



TECHNISCHE
UNIVERSITÄT
WIEN

DOCTORAL THESIS

Development of an Interferometry-Based Drift-Compensated Scanning Probe Microscopy Technique to Measure Surface Forces (Molecular Forces Apparatus, MFA)

zur Erlangung des akademischen Grades

Doktor der technischen Naturwissenschaften

an der Fakultät für

Technische Physik

eingereicht von

Kai A. Schwenzfeier BSc. MSc.

Matrikelnummer 11743127

ausgeführt am Institut für Angewandte Physik
der Fakultät für Physik der Technischen Universität Wien

Betreuer: Univ.Prof. Dipl.-Ing. Dr.techn. Valtiner Markus

Ort, Datum

(Unterschrift Verfasser)

(Unterschrift Betreuer)

Ich erkläre an Eides statt, dass ich die vorliegende Dissertation selbständig und ohne fremde Hilfe unter der Betreuung von Univ. Prof. Dr. Techn. DI Markus Valtiner verfasst habe. Es wurden keine anderen als die angegebenen Quellen und Hilfsmittel benutzt beziehungsweise die wörtlich oder sinngemäß entnommenen Stellen als solche kenntlich gemacht.

Wien, am 18. März 2022

Acknowledgements

Es heißt, jeder sei seines Glückes Schmied. Diese Beschreibung ist mindestens ebenso libertär und romantisch wie sie falsch ist. Zwar lohnt es sich für jeden, ein paar Techniken der Schmiede zu meistern, wie „sein Feuer nicht erlöschen zu lassen“ oder „stets mehrere Eisen im Feuer zu haben“, aber um sich erfolgreich Glück zu erschaffen, braucht es viel mehr als das.

Sowohl Soziologie als auch Psychologie schreiben Buch um Buch darüber, welche Art Eisen man sein muss, wie viel Wärme und Hitze es braucht und wie hart einen der Hammer in Form bringen muss, bevor man glücklich wird. Doch Einigkeit herrscht vor allem darin, dass es für Glück immer große Mengen an Zufall braucht. Ich denke, neben eigener Fertigkeit und einer Menge Glück, bedarf es vor allem auch an vielen helfenden Händen!

Wenn man ein seltsames Stück Metall ist, dem nachgesagt wird, ein Alien zu sein, nicht so recht formbar zu sein, an Stellen zu spröde, an anderen zu hart, ist man doch dankbar um jede helfende Hand, die, wenn es nie Mangel an Menschen gibt, einem neue Steine in den Weg zu rollen, zeigen, eigene neue Wege zu finden, zu klettern, Widerstände zu sprengen. Menschen, die einem Mut zusprechen, die einen auf die eigenen Schultern klettern lassen, die einem mit Wissen und Fähigkeiten unterstützen, an einen glauben, auch wenn es stellenweise nicht nach Fortschritt aussieht.

In diesem Sinne danke ich allen, die mir geholfen haben, meinen Weg bis hier hin zu gehen, meine Kämpfe gegen mich selbst und die Welt zu überstehen.

I would like to thank Markus Valtiner for many good discussions, especially the harsh ones and for bearing and trusting in me in times of “low energy”. Also for giving me the opportunity to work on this challenging project with a lot of interdisciplinary things to learn. I also thank Andreas Erbe for introducing me to MPIE, for trusting me with the code to his program (reflcalc) which finally inspired my first actual project big enough to actually learn coding.

Ralf Selbach and his workshop team at MPIE for helping me through the process of bringing MFA to something actually machinable. Iván González for the fast-paced crash-course in LabView that enabled me to go writing a controlling software for XSFA from “Where do I write the actual code? And then I click those icons? And what do these pipes do?” within less than a day. (With a few modifications this software still controls our SFAs) Rainer Gärtner and Herbert Schmidt for their constant struggle of precision and to help me tackle the last machining steps until MFA was actually operable. Marie for her many hours of work in trying to solder those thousands of flimsy and tiny cable leads and their shielding of the MFA real-time cables to more tiny cables in make-shift adapters without proper documentation from the companies. Michael Schmid for giving me a fast paced introduction to electronic debugging and repair while saving the MFA piezo amplifier.

Tabrisur Khan for his continuous reminder to regularly keep taking my “vitamin Z” (tea). Waldemar Krieger and Igor Barsukov for lots and lots of good discussions

about basically everything. Qingyun Hu for giving me my first introduction to SFA technique even if this ended with complete disassembly and misalignment of SFA1 in Düsseldorf. For her patience in showing me the basics of mica cleaving and the importance of cleaning *everything* around SFA setups. Multiple times if needs be. Claudia Merola for many years of being the bubbly, cheerful, inclusive good spirit of the group. Laura Mears for always having an open ear and always lending a helping hand.

Danken möchte ich auch meinen Eltern, für all die Unterstützung, Hilfen, Gespräche und Gedanken, die mich mein Leben durch begleitet haben. Ich danke Tina, dafür dass sie mich gestützt und unterstützt hat in meiner Zeit vor Wien, Manu für die gemütlichen Teerunden in Zeiten, in denen die Welt still stand, Melli dafür, dass sie mich immer wieder „erden“ konnte und für all die Jahre der Freundschaft. Und schließlich danke ich meiner geliebten Sophie für ihre Geduld, wenn ich mich zum Arbeiten zurückziehe und dafür, dass sie mich immer aufheitert, wenn es nicht so gut läuft.

Finally I would like to thank the European Research Council for funding through the grant CSI.interface, ERC-StG 677663.

Abstract

Measurement of forces between molecules and surfaces at solid-liquid and solid-gaseous interfaces have been studied for decades, but the precision was often hampered by artefacts stemming from drift within the measurement devices themselves.

This work describes the development of an apparatus that compensates for drift in all three spatial axes in a rigorous, method independent way and a white light interferometric method to detect absolute distance and bending of an AFM cantilever in reflection geometry.

Based on experience with multiple beam white light interferometry in transmission geometry, as has often been used in the Surface Forces Apparatus (SFA), the method of analysis has been improved to allow determination of absolute distances by employing a new way of analysis using a 4×4 multiple matrix method. This analysis method has further been extended to allow analysis of white light interferometry spectra in reflection geometry and arbitrary layered sample stacks. This allowed the development of SFA in reflection mode, analysis of isotropic and birefringent additional layers, as well as completely new layouts such as the 3-layer-surface-forces-sensor.

The apparatus was designed and built to measure drift and thermal expansion along five axes (three spatial, two rotational) using IR-laser interferometric sensors and compensate drifts and environmental influences to an unprecedented stability, in the sub-nanometers, for experiments spanning several hours. As example techniques an SFA-type and AFM-type scanning probe microscope has been implemented.

The software developed during this work (*SFA Explorer*) is commercially available, the apparatus design (*Molecular Forces Apparatus, MFA*) has been filed as a patent.

Kurzfassung

Die Vermessung von Kräften zwischen Molekülen und Oberflächen an fest-flüssig, sowie fest-gasförmigen Grenzflächen ist bereits Objekt wissenschaftlicher Untersuchungen. Jedoch behindern oftmals Messartefakte wie geräteinhärenter Drift die Aussagekraft und Präzision solcher Messungen.

Die vorliegende Arbeit beschreibt die Entwicklung einer Apparatur, die agnostisch einer speziellen Messtechnologie Drift innerhalb der Maschine entlang aller drei Raumrichtungen kompensiert, sowie eine Methode, weißlichtinterferometrische Absolutdistanzen und Deformationen eines AFM Kantilevers in Reflektionsgeometrie zu bestimmen.

Ausgehend von Erfahrungen mit Weißlichtinterferometrie in Transmissionsgeometrie, wie sie oft beim Surface Forces Apparatus eingesetzt wird, konnte eine Analysenmethode entwickelt werden, die die Bestimmung absoluter Distanzen mit Hilfe eines 4×4 -Multimatrixansatzes möglich macht. Diese Analysemethode wurde erweitert auf Messungen in Reflexionsgeometrie, sowie auf Proben aus beliebig vielen Schichten unterschiedlicher Parameter, sowohl optisch isotrop als auch doppelbrechend. Auch wurden so komplett neue Probensysteme, wie sie für die 3-layer-surface-forces-sensor Technik benötigt werden, analysierbar.

Das Design des Apparats basiert darauf, Drift und thermische Expansion entlang von bis zu fünf Achsen (drei räumliche und zwei Rotationsachsen) mittels infrarot-laserinterferometrischen Sensoren zu bestimmen und zu kompensieren. Hierdurch konnte eine bisher unerreichte Unabhängigkeit von Drift und Umwelteinflüssen über viele Stunden erreicht werden. Als Beispielsimplementationen wurden SFA-artige und AFM-artige Sondenmikroskopie implementiert.

Die hier entwickelte Software (*SFA Explorer*) wird bereits vermarktet. Das Gerätedesign (*Molecular Forces Apparatus, MFA*) wurde zum Patent angemeldet.

Contents

1	Motivation	1
1.1	Introduction	1
1.2	Direct Measurement of Reaction Kinetics	3
1.3	Current State of the Art of Drift Correction in AFM	4
1.4	Aims and Questions	5
2	Implementation of 4×4 Matrix Method for Multiple Beam White Light Interferometry	7
2.1	Multiple Beam White Light Interferometry	8
2.2	Ellipsometry and Multiple Matrix Methods	10
2.3	Matrix Methods for MBI	12
2.4	Schubert's 4×4 Matrix Approach Adapted to MBI	14
2.5	Comparison of Matrix Method and Analytical Analysis	15
2.6	Simulation of Typical FECO Spectra	17
2.7	MBI in Reflection Geometry	18
2.8	Effects of White Light Spectra	19
2.9	Effects of Layers Outside the Interferometric Cavity	20
2.9.1	Effects of mirror properties	20
2.9.2	Effects of Supporting Glue	23
2.10	Further Improvements to the SFA Technique	26
2.10.1	Improved Optical Path	26
2.10.2	Determination of Mica Optical Properties	30
2.10.3	Rotation of the Mica Lattice for Symmetric 3–5 Layer Interferometers	31
2.11	Validation of Matrix Method MBI Analysis	32
2.11.1	Thickness of Confined Molecular Layers, Radius Calibration and Force Distance Characteristics	32
2.11.2	Refractive Index of Fluids Confined Into a Crevice	34
2.12	Discussions and Conclusions	36
2.12.1	Practical Implications for SFA Experiments	36
2.12.2	Accuracy and Potential for Automation and Real-Time Analysis	37
2.12.3	Conclusions	38
2.13	Further Dissemination	39
2.13.1	Impact on Further Projects	39

Contents

2.13.2 Showcase	40
2.14 Outlook and Roadmap for the Software	43
3 Molecular Forces Apparatus - Proof of Principle	45
3.1 Introduction	45
3.2 Concept	46
3.2.1 Design Principle	47
3.3 Results and Discussion	50
3.3.1 SFA Measurements and Characterization of Device Behavior	50
3.3.2 MBI AFM Theory and Measurements	53
3.3.3 Complementary Discussion of Force Probe Techniques and the SFC Principle	57
3.4 Conclusion	58
4 Summary and Impact	61
4.1 Aims	61
4.2 Impact on Other Work	61
4.3 Outlook	62
Appendix	63
Methods and Materials	65
Implementation of 4×4 Matrix Method for Multiple Beam White Light Interferometry	65
Molecular Forces Apparatus - Proof of Principle	67
List of Publications	69
Excerpt from Patent	73
Copyright Clearances	77
Bibliography	79

List of Figures

1.1	Description of a typical experiment in Single Molecule Spectroscopy with resulting force/distance curve	2
2.1	Layout and Map of Layers of a Typical SFA Experiment	9
2.2	Definition of Optical Quantities for use in Matrix Formulation	11
2.3	Examples of Simulated SFA Spectra	16
2.4	FECO in Transmission and Reflection Geometry	18
2.5	Typical White Light Spectral Deconvolution	20
2.6	FECO Position Shift Depending on Mirror Thickness	21
2.7	Influence of Supporting Glue Layer Thickness on FECO Spectra	23
2.8	Simulation of Interferometric Superposition due to Asymmetric Glue Layer Thicknesses	25
2.9	Improved Optical Path for SFA	27
2.10	FECO Spectrum as Measured With Improved Optical Path	28
2.11	SFA Experiment Flowchart	29
2.12	Determination of Mica Refractive Index	30
2.13	Force vs. Distance Graph of Typical Forcerun With Lipid Bilayers	33
2.14	Simulation to Determine Detection Limit of Birefringent Splitting	35
2.15	Analysis of Density Fluctuations in Close Confinement	36
2.16	Screenshot of SFA Explorer Main Screen	41
2.17	Screenshot of Major SFA Explorer Options Screens	42
3.1	MFA Schematic for SFA and AFM Mode	48
3.2	MFA Optical Path	49
3.3	MFA: Dependence of Measured Distances	51
3.4	MFA: Force/Distance Characteristic and Performance in SFA Mode	52
3.5	MFA: Influence of Cantilever Mount Angle in AFM Mode	54
3.6	MFA: AFM Mode Experiment Analysis	56

Acronyms

- A Helmholtz free energy. 2, 3
- D layer thickness. 8
- D FECO distance. 9, 47, 48, 50, 51, 53, 55–57
- F Force. 9
- G Gibbs free enthalpy. 3
- H enthalpy. 3
- K equilibrium constant. 3
- PID_z PID output position. 47, 50, 51, 56
- R gas constant. 3
- R SFA disk curvature radius. 9
- Sp_z distance setpoint. 47, 50, 51
- S entropy. 3
- T temperature. 3
- U internal energy. 3
- V volume. 3
- W_{diss} dissipated work. 3
- Z laser interferometric distance. 47, 48, 50, 51
- $\Delta_R G^0$ standard reaction Gibbs free enthalpy. 3
- Ω optical thickness. 8
- α cantilever mounting angle. 54
- \bar{W} average work. 2
- k_{forward} reaction rate constant for the forward reaction. 3, 4
- k_{reverse} reaction rate constant for the reverse reaction. 3, 4

Acronyms

n real part of a refractive index. 8

p pressure. 3

AFM Atomic Force Microscopy. 1, 2, 4, 5, 7, 45–47, 50

BLAS Basic Linear Algebra Subprograms. 15

CSC Complete Spectral Correlation. 17, 34

DPPC Dipalmitoylphosphatidylcholine. 32

FCS Fast Correlation Spectroscopy. 15

FECO Fringes of Equal Chromatographic Order. 8, 36, 39, 48, 55

GUI Graphical User Interface. 40

MBI Multiple Beam White Light Interferometry. 5, 7, 10, 45–47, 53–55, 57, 61, 67

MFA Molecular Forces Apparatus. 45

MOKE Magneto-optical Kerr Effect. 61

OT Optical Tweezers. 7

QE Quantum Efficiency. 19

SAM Self Assembled Monolayer. 1, 2, 32

SFA Surface Forces Apparatus. 5, 7–9, 39, 46, 47, 50, 61, 65

SFC Surface Forces Clamp. 46, 47, 67

SMS Single Molecule Spectroscopy. 1, 5

SPM Scanning Probe Microscopy. 4, 5, 7, 45, 47

SPR Surface Plasmon Resonance. 61

STM Scanning Tunnel Microscopy. 7

WLI White Light Interferometry. 8

X-SFA hybrid of Surface Forces Apparatus to simultaneously measure X-Ray Reflection. 17

XRR X-Ray Reflection. 39

1 Motivation

A good tool improves the way you work.

A great tool improves the way you think.

(Jeff Duntemann)

Since the earliest days mankind has strived to its use curiosity, to learn from its world around, to make tools, and to forge a better living. This work is a part of just another of those stories.

Methods of “making things” can be one of two: giving form and function by removing surplus stuff, and giving form and function by adding stuff, or a combination of both.

When adding materials it inevitably comes down to the question of how to make parts stay in the position they are supposed to be. Besides many mechanical, physiological, and chemical ways, using glues have become one of the major methods of our time, as the flexibility in what can be glued and what physical properties of the joint arise from this has proven to be huge.

Most classes of glues consist of some kind of organic polymer with special properties or chemical groups to anchor it on different materials. The characterization of how good a given glue performs on a macroscopic scale has been well measured and characterized.

However the actual glue making still remains a process of empirical recipes using a number of different components in the ten to fifty ingredients range, without detailed knowledge of why and how the single components work, if at all.

A way of learning about the mechanisms of how glue actually adheres to a substrate and which components are necessary for this is to measure bond strength of functional groups anchoring the polymer to a substrate. This can proceed by isolated, single molecules and successively scaling up the model to allow interaction between polymers and with other ingredients.

1.1 Introduction

A main tool for characterizing bond strengths of single functional groups is Single Molecule Spectroscopy (SMS). This method is in principle a pulling experiment within an Atomic Force Microscope using a tip functionalized with a Self Assembled Monolayer (SAM) using a mixture of a reactive polymer diluted in a non-reactive

1 Motivation

polymer, and a sample functionalized in the same way, but with a different reactive polymer. If the reactive end-group of the polymer is able to attach on either a metallic coating of tip or sample, the respective SAM can be omitted. In this experiment (see figure 1.1) the tip approaches the sample, giving the reactive end-groups a chance to react with their counter part, then pulling until the bond rips apart.

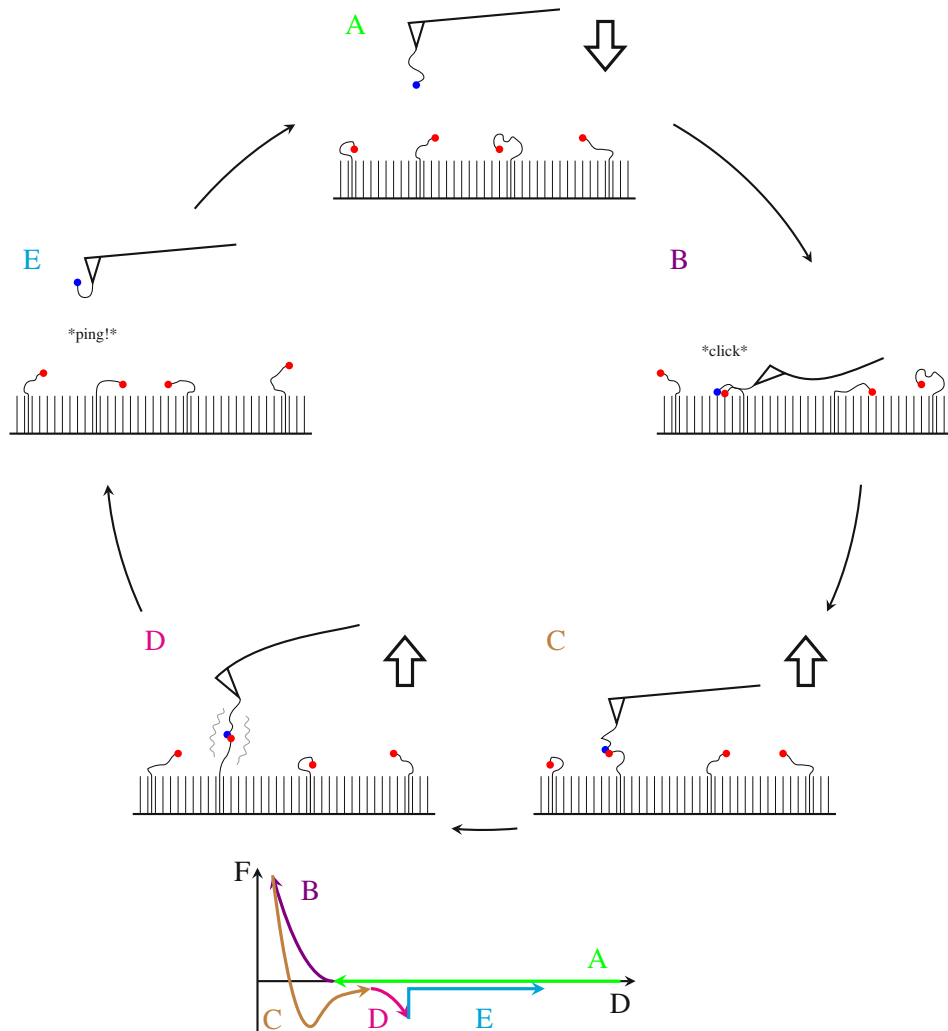


Figure 1.1: A typical Single Molecule Spectroscopy experiment: Both, the tip of an AFM probe and a sample surface are incubated with a SAM with reactive end-groups (sample side is diluted). The probe approaches the sample (A). On contact with the sample the endgroups have a chance to react (B). The tip is being retracted from the surface (C) to the extent the polymers holding the end groups and the probe are strained (D) until the bond between the functional endgroups breaks (E). Below is the resulting force (F) versus distance (D) curve. The integral over D is used for analysis.

Under the assumption the pulling is infinitely slow to approach quasi-equilibrium conditions, the average work (\bar{W}) approaches the Helmholtz free energy (A) (Jarzynski's Equality [1, 2]):

$$\bar{W} = \Delta A + W_{\text{diss}} \quad (1.1)$$

where the dissipated work (W_{diss}) vanishes. This model however does not yet include the additional pulling force the polymer backbone applies to the bond due to its Brownian motion. Taking all of this into account the average work becomes a weighted integral with the most contributing events being the rarest (polymer chain “coincidentally” completely straight while the bond rupture occurs).

It is obvious, doing a statistically relevant amount of experiments (so rare cases happen often enough), where each individual experiment takes infinitely long (infinitely slow pulling), is practically not feasible, which leads to compromise and uncertain, derived values are to be expected.

To circumvent those challenges, the present work aims to develop a new technique capable of finding an easier and more direct way of measuring bond strengths and dynamics in a truly quasi-static fashion.

1.2 Direct Measurement of Reaction Kinetics

Jarzynski’s idea was to derive equilibrium quantities from a non-equilibrium process, as a direct measurement of kinetics at this time was not feasible. But how could such a direct measurement work?

Using A is a good choice to compare results of those measurements to simulations as the internal energy (U) within the definition of Helmholtz free energy:

$$A = U - TS \quad (1.2)$$

(using temperature (T) and entropy (S)) can be easily obtained from *ab-initio* calculations.

A more experimentalist-friendly quantity is the Gibbs free enthalpy (G), which is defined as:

$$G = H - TS \quad (1.3)$$

(using enthalpy (H)).

The standard reaction Gibbs free enthalpy ($\Delta_R G^0$) can be directly related to the equilibrium constant (K) which relates to reaction rate constants of the forward (k_{forward}) and backward (k_{reverse}) reactions forming the equilibrium:

$$\Delta_R G^0 = -RT \ln K = -RT \ln \frac{k_{\text{forward}}}{k_{\text{reverse}}} \quad (1.4)$$

(using gas constant (R)).

The difference between the Gibbs free enthalpy G and the Helmholtz free energy A is the difference between enthalpy H and internal energy U :

$$G - A = H - U = p \cdot V \quad (1.5)$$

Assuming neither pressure p nor volume V change during the bond formation, the

difference can be neglected.

The relation of the reaction rate constants k_{forward} and k_{reverse} can be derived by measuring the time a single bond spends in the “product”, aka bound state with respect to the time this bond is in the “educt”, aka unbound state.

If it can be made possible to keep the tip of the probe steady at a defined position and distance over the sample, the difference between the bound and unbound state should be evident from the above mentioned Brownian motion of the continuous polymer chain pulling on the bond from being in a bound state on the tip. This means the tip in the unbound state should be in a forceless “up”-state while the bound state should exhibit some force pulling the tip down (“down”-state).

Design Goals for a Quasi-Static Single Molecule Atomic Force Microscope

A device to directly measure kinetics by the aforementioned mechanism needs certain properties and qualities to enable such a measurement.

The most crucial property is the ability to keep a steady and defined position of the probe with respect to the sample. Modern Atomic Force Microscopes, or Scanning Probe Microscopes in general, lack both. In AFM the distance between tip and sample is strictly only known when the tip presses onto the surface with high force which might already change the tip geometry. Distances higher than that are derived from the piezo extension which is prone to creep and thermal fluctuations. The lateral position is known to exhibit drift in the order of a few micrometers per minute. Those shortcomings are known to be detrimental to the scientific insight of investigations and a lot of effort has been made to reduce those uncertainties.

1.3 Current State of the Art of Drift Correction in AFM

Measurement artefacts caused by thermal drift are well known to the AFM community. [3] Aside from concepts of stabilizing temperature, pressure, and humidity in the laboratory, isolating vibrations acting on the machine, and using materials less prone to those influences, the main concepts to counter those problems range from measuring in elliptical intersecting paths [4], known “landmarks” within the sample [5, 6], post-processing of data [7], optical tracking of the blurring of fiducial markers [8], or estimation of drift [9] (only a few representative studies mentioned for each).

However, those methods inherently work for position dynamic measurements, overestimate potential correctable resolution of optical imaging methods (blurring), and or underestimate the non-linear properties of drift itself (estimating, post-correction). (For a more thorough description, also see chapter 3.1.) A device to acutally keep a controlled static absolute position was not available prior to this work.

1.4 Aims and Questions

This present work consists of two major parts, each describing building blocks enabling a new technique for direct kinetic measurements of single bond breaking events.

The first part (chapter 2) focuses on the introduction and development of an analysis method for Multiple Beam White Light Interferometry (MBI) that allows tracking of the absolute distance of a probe with respect to the sample, with sub-nanometer precision, using a matrix-based formalism adapted to MBI. This chapter also includes a discussion of and improvements to the Surface Forces Apparatus (SFA) technique in general.

The second part (chapter 3) describes the development of an apparatus that works as a positional cage in five dimensions to compensate for thermal drift, vibrations, as well as piezo creep in an AFM. This part also characterizes the performance of the designed device in both, an SFA mode as a benchmark, and a novel AFM mode. The actual static single molecule bond breaking experiments are beyond the scope of this work and will be dealt with in follow up work.

Both parts have, at the time of submission of this work, been subject of a peer-review process (second part is still in review process) and were published or patented where applicable.

In summary the aims of this thesis are:

- To establish an analysis method for use with MBI in reflection geometry,
- introducing beam path optimizations to ensure more mechanical stability and optical reproducibility,
- designing a device to stabilize Scanning Probe Microscopy (SPM)-based measurements against drift on timescales between several minutes to hours,
- implement an MBI-based SPM method to enable static SMS experiments with probing areas in the range of AFM cantilevers.

2 Implementation of 4×4 Matrix Method for Multiple Beam White Light Interferometry

Measuring distances in principle is a long-solved problem. There are many techniques available for different lengthscales and resolutions, as long as both endpoints are accessible to some kind of sensors.

When tasked with measuring displacements in a gap between two interfaces over atomic lengthscales SPM based techniques are considered state-of-the-art. SPM based techniques usually drive either sample or probe using a piezo-electric crystal and measure distance related properties (AFM: deflection of a laser, Scanning Tunnel Microscopy (STM): current, Optical Tweezers (OT): displacement of the optical image of the sample) as a result of movement. While blurring of an optical image is *a-priori* prone to imprecision, the other methods are still far from being able to reliably measuring an absolute distance without the attempt to correct-guess fundamentally random influences (notably: thermal drift) using crude approximations (linearity, known hysteresis). The only case a distance measurement using those methods surpasses those uncertainties is when probe and sample are in firm contact with each other, without any deformation of the probe or indentation of the sample happening. In this case the distance problem becomes trivial.

Other, not-so-common techniques for non-damaging measuring distances on atomic lengthscales that aim for a higher degree of precision, are interferometry or at least optical property based. Ellipsometry and the SFA are notable variants. While well suited to measure distances, both lack the lateral resolution to investigate properties of single molecules.

A combination of interferometry based distance measurements with lateral resolution of AFM would be an ideal match for those kind of experiments.

The Aim of This Chapter is to develop an analysis method for analysis of MBI spectra. Focus points of this part of the present work were to:

- improve the analysis method with respect to methods available for the SFA technique,
- introduce new analysis capabilities to widen applicable range of the SFA technique, especially with respect to birefringent materials and a geometry change to analyze spectra taken in reflection.

In addition to those aims this chapter depicts a collection of directly obvious improvements to the SFA technique itself and name a few selected studies that have been directly enabled by the proposed analysis method.

Substantial parts of this chapter have been published as [10] including supplemental information. Variable names may differ from the rest of this work as the scientific community around the SFA technique has not yet settled for a common naming scheme. Thus, variable names have to change depending on which other work is used as context.

2.1 Multiple Beam White Light Interferometry

A prominent implementation of White Light Interferometry (WLI) is the SFA as pioneered by Jacob Israelachvili. The principle uses samples glued to quartz disks with cylindrical curvature, facing each other with the apexes of the curvature being perpendicularly aligned (cross-cylinder alignment) (see figure 2.1 (a)). One of those disks is mounted at a fixed position while the other resides on a levered system of leaf springs to enable very fine dosages of distance and force change. The optical path resembles a transmission microscope geometry with the beam path ending in a spectrometer.

A sample in these terms is usually a molecularly smooth cleaved sheet of muscovite mica with a thickness ranging between 3 and 10 μm with thinner sheets being used more commonly. On the backsides (facing the glue) of those sheets is a thin film of deposited metal (in the following: mirror, as short form of semi-transparent mirror), thin enough to let light through, but thick enough to form interference patterns between two of those metal films (typically ranging between 20 and 55 nm).

Samples like this can be functionalized on the mica side facing towards the opposing sample and used to measure surface and interaction forces with different solutions between the samples during compression and decompression of the formed gap.

The constructive interferences of those patterns, called Fringes of Equal Chromatographic Order (FECO) generated this way are a unique description of the optical thickness (Ω) between those metal films. The optical thickness is defined as:

$$\Omega = \sum_i \mu_i \cdot D_i \quad (2.1)$$

with i indexing all layers *between* the mirrors, the real part of refractive indices (n), and the layer thickness (D) for each layer.

For a classical system like this (both samples using mica of the same thickness), Israelachvili developed an analytical equation to derive the thickness of the fluidic layer:

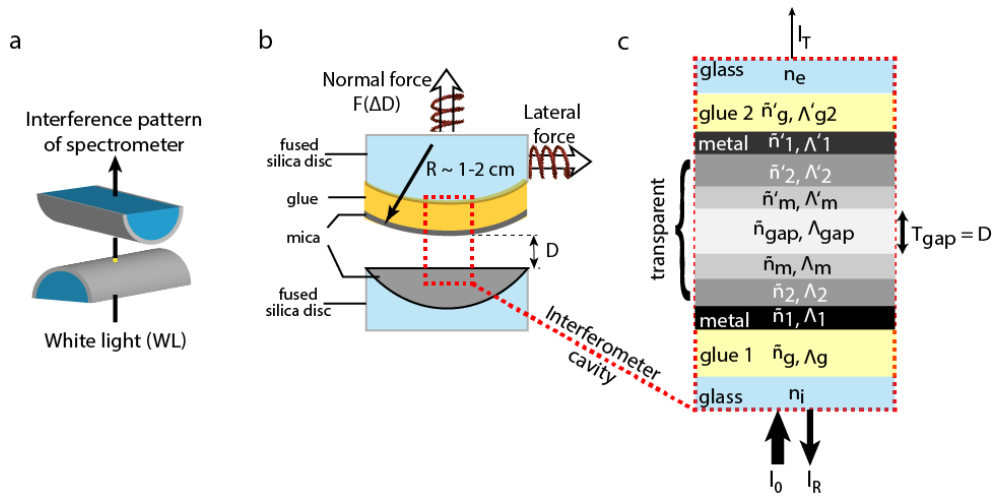


Figure 2.1: **(a)** The typical sample geometry in SFA experiments is a crossed cylinder geometry. **(b)** Absolute distance, D , the contact radius, R , and lateral as well as normal force are measured in an SFA experiment. **(c)** Typical options for interferometer stacks in transmission and reflection mode consist of up to 2–7 layers in transmission mode and 2–5 layers in reflection mode, depending on whether specific surface modifications are applied or not. Reflective metal mirrors (Λ_1/Λ'_1) are essential for establishing an interferometer cavity. They are semitransparent with $\Lambda_1 = \Lambda'_1 \approx 30$ to 55 nm. While in reflection mode one bulk metal layer with $\Lambda'_1 \rightarrow \infty$ is used. Any number of transparent layers that can be stacked between the metals necessarily have a combined thickness ≥ 2 – 3 times the wavelength of the light used, in order to establish resonance in the wavelength range used. In a typical SFA experiment forces F are measured as a function of a fluid gap layer thickness Λ_{gap} that defines the absolute surface separation $D = \Lambda_{\text{gap}}$. The layers between the metal mirrors can be setup in many different ways, and the glue layer indicated in **(b)** is usually chosen in such a way that it matches the refractive index of glass. (see text for details).

$$\tan(2\pi n_{fl} D / \lambda_j^D) = \frac{2n_{rel} \sin \left[\frac{1 - \lambda_j^0 / \lambda_j^D}{1 - \lambda_j^0 / \lambda_{j-1}^0} \pi \right]}{(1 + n_{rel}^2) \cos \left[\frac{1 - \lambda_j^0 / \lambda_j^D}{1 - \lambda_j^0 / \lambda_{j-1}^0} \pi \right]} \pm (n_{rel}^2 - 1) \quad (2.2)$$

using the spectral position of a fringe in contact λ^0 and during the experiment λ^D for two adjacent fringes (indexed as j and $j - 1$), the assumed uniform and constant refractive index of the fluid (n_{fl}) and a ratio between the refractive indices of the fluid and mica (n_{rel}). The varying sign refers to $+$ for odd and $-$ for even fringes.

Similar equations have been published for systems with mica on only one side, as well as more complex layouts, and simplified versions. [11, 12]

While this analysis framework carried the method over many years, it was never able to fulfill the claim of MBI being a method of absolute distances.

2.2 Ellipsometry and Multiple Matrix Methods

Ellipsometry on the other hand uses a variable incident angle reflection type of geometry. Light is linearly polarized (not strictly a requirement, but the most common implementation) and the change of polarization of this light, after being reflected from a sample, is measured (can be either monochromatic or spectral distribution).

The complex ellipsometric ratio ρ can be described as a ratio of reflection amplitude coefficients in p- and s-polarization (parallel (p) to the plane of reflection and perpendicular (s)) or as a function of an amplitude describing the real quantity Ψ and a phase shift describing the imaginary quantity Δ :

$$\rho = \frac{r_p}{r_s} = \tan \Psi \times e^{i\Delta} \quad (2.3)$$

[13]

A common approach to analysis of ellipsometric properties is to start with a model consisting of layers with given thicknesses and more or less known refractive indices, then simulate spectra of Ψ and Δ , and try to match those spectra to the measured spectra using some kind of fitting algorithm. A direct interpretation is usually not the favorable approach due to the sheer complexity of different possible intricate optical effects acting on the incident light typically defying any intuitive understanding.

This led to a strong focus on mathematical methods and formalisms suited to describe the generation of spectra given a limited set of parameters using Maxwell's field equations in a matrix multiplication based formalism. A literature selection on the history can be found in: [14–20]

Given the fundamental character of Maxwell's field equations, any approach to find a solution to a specific problem within limited time is challenging. Therefore the art of devising a formalism first of all consists in picking suitable boundary conditions.

One of the main areas of application of ellipsometry is evaluation of the semicon-

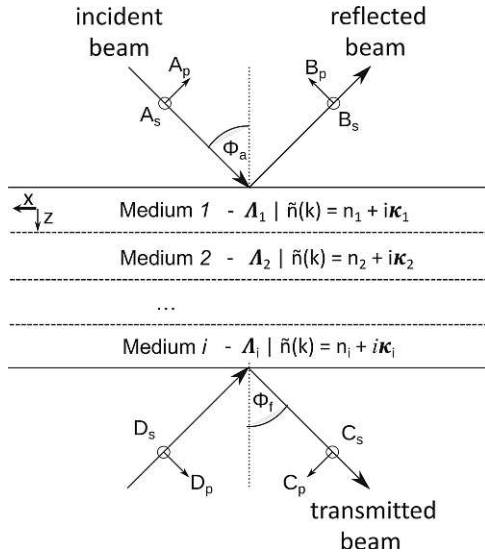


Figure 2.2: Definition of simultaneously measurable and theoretically accessible components of electromagnetic waves propagating through a slab of i parallel layers with thicknesses Λ_i and complex refractive indices \tilde{n} , established in the Schubert method. [21]

ductor manufacturing process. The process can be summarized by a series of steps: a layer-by-layer masking, selective and patterned dissolution of the masking layers, etching where the mask has been removed, rinse and repeat. The resulting structures are stacks of parallel layers of patterns within a substrate that can be discerned by optical properties. Thus, the boundary condition is a stack of optically homogeneous materials with parallel interfaces and finite but varying thicknesses. Since potentially the number of such layers can vary greatly and even the way those layers interact with light can be different, a versatile method would require a formalism that allows for a layer-by-layer description of optical interactions and an easy way of combining layers to form a stack of layers to yield a resulting description.

The matrix based approach used in this work is such a formalism that uses matrices to describe the effect of each single layer (partial transfer matrix \mathbf{T}_p) on light amplitudes of incoming and exiting light. It is possible to stack layers by matrix multiplication of multiple layers to form a total description (transfer matrix \mathbf{T}) if also combined with matrices crafted to describe the semi-infinite layers the light traverses before approaching the stack (\mathbf{L}_a^{-1}) and after leaving it (\mathbf{L}_f) (see figure 2.2).

$$\mathbf{T} = \mathbf{L}_a^{-1} \prod_{i=1}^N [\mathbf{T}_{ip}(\Lambda_i)]^{-1} \mathbf{L}_f = \mathbf{L}_a^{-1} \prod_{i=1}^N \mathbf{T}_{ip}(-\Lambda_i) \mathbf{L}_f \quad (2.4)$$

Another important question arises about the effects the matrix method is supposed to describe. While simple isotropic layers with negligible effect on the magnetic amplitudes of light are sufficiently described by 2×2 matrices, including layers featuring optical uni-axial anisotropy, birefringence, or helical anisotropic effects (such as caused by liquid chiral molecules), 4×4 matrices are required to discern effects on s- and p-polarization amplitudes:

$$\begin{pmatrix} A_s \\ B_s \\ A_p \\ B_p \end{pmatrix} = \mathbf{T} \begin{pmatrix} C_s \\ D_s \\ C_p \\ D_p \end{pmatrix} = \begin{pmatrix} T_{11} & T_{12} & T_{13} & T_{14} \\ T_{21} & T_{22} & T_{23} & T_{24} \\ T_{31} & T_{32} & T_{33} & T_{34} \\ T_{41} & T_{42} & T_{43} & T_{44} \end{pmatrix} \begin{pmatrix} C_s \\ 0 \\ C_p \\ 0 \end{pmatrix} \quad (2.5)$$

(for a definition of matrix elements A through D , see figure 2.2)

Further assumptions subsequently used in this work include: the absence of additional illumination from the backside of the stack ($D = 0$), negligible influence on the magnetic amplitudes of light caused by each layer, quasi-monochromatic behavior (no effect on light amplitudes of one wavelength caused by light of another wavelength) which includes light emission of layers, no scattering, no depolarization, no stray light.

Given a working stack description using a transfer matrix, actual observable optical effects, such as ellipsometric spectra, transmission spectra, or reflectance spectra, can be derived via computation of Fresnel Coefficients from elements of the transfer matrix and subsequently transmittance and reflectance from those. [22]

2.3 Matrix Methods for MBI

Thin film studies using multiple-beam interferometry (MBI) evolved as a powerful tool for measuring absolute thicknesses and complex refractive indices, \tilde{n} , of nanometer confined thin films between apposing surfaces.

Since the first analysis of MBI patterns by Tolansky [23] the technique was further evolved to study surface and interfacial forces in biological and engineering environments. Implemented in the Surface Forces Apparatus (SFA), which was pioneered by Tabor, Winterton and Israelachvili. [24–26] MBI provided direct quantification of fundamental interaction forces across surfaces and thin-film properties down to separation distances D below 1 nm, including the first measurement of van der Waals forces, [27] hydration layering, [28] or hydrophobic interactions. [29] Other applications included polymers in solution, [30] the experimental verification of the Kelvin equation, [31] and DLVO forces [32].

As shown in figure 2.1 (a)/(b), in a typical SFA experiment two 90° -crossed silica cylinders, covered with back-silvered transparent mica surfaces are brought into contact. The central aspect of the SFA experiment is that the apposing surfaces are set up in such a way that they form an interferometer for MBI. White light is then transmitted perpendicular through the apposing surfaces, resulting in standing waves forming fringes of equal chromatic order (FECO) that can be recorded with an ordinary imaging spectrometer. Variation of absolute separation distances D of apposing surfaces can subsequently be measured by tracking wavelength shifts of FECO. [26]

Figure 2.1 (c) shows an overview of possible options for combining optical slabs for establishing interferometers for transmission and reflection mode operation in SFA (see figure for details).

In transmission mode fluids with thickness Λ_{gap} , and complex refractive index \tilde{n}_{gap} are frequently confined between transparent layers of uniformly thick muscovite mica ($\Lambda_2 = \Lambda'_2$ with a complex refractive index of $\tilde{n}_2 = \tilde{n}'_2$). Semi-transparent silver mirrors, henceforth referred to as “mirrors”, with thicknesses $\Lambda_1 = \Lambda'_1 = 30\text{--}55$ nm, are applied to the backside of the mica layers. Using MBI then allows measurement of the thickness of the mica layers (at $\Lambda_{\text{gap}} = 0$), and subsequently the distance between surfaces defined as $D = \Lambda_{\text{gap}}$.

Simultaneously normal forces $F(D)$, as well contact radii, R , between the surfaces can be measured using MBI. [12, 26] Strain gauges are often implemented for detecting friction forces. [12]

Muscovite mica has been used as a transparent material because it is relatively simple to prepare uniformly thick and atomically smooth layers. [24] Mica layers are typically cleaved to thicknesses ranging from 3–6 μm . Mica can be further, chemically modified introducing additional thin layers on both or one of the apposing surfaces, establishing either symmetric or asymmetric interferometers, respectively. The resulting thin-film modifications have defined thicknesses (Λ_m and/or Λ'_m) and refractive indices (\tilde{n}_m and \tilde{n}'_m), and can be applied using a number of approaches including formation of supported lipid bilayers [33] as well as self-assembled silane monolayers. [34, 35]

Another frequently used interferometer layout is formed by facing one back-silvered mica surface against smooth metal surface (usually for example gold, platinum, palladium) templated from mica [36, 37] or evaporated by magnetron sputtering or physical vapor deposition. The latter also have a surface roughness of $\sigma_{\text{rms}} = 1\text{--}2$ nm, while templated surfaces are smooth with $\sigma_{\text{rms}} < 0.5$ nm. [36] In such a setup it is again possible to introduce chemical surface modifications, such as self assembled monolayers on gold, [35] or modifications used for mica, resulting again in asymmetric/symmetric interferometers.

A reflection mode interferometer can be formed for example by using a bulk metal that faces a back-silvered mica surface. This setup has so far been tested in only one set of experiments by Roger Horn *et al.* [38] where shape-changes of Mercury-drops were induced electrochemically. With the increasing interest in electrochemical interfaces and corrosion studies, [39, 40] oxide covered bulk metal samples became increasingly important in SFA experiments. However, no rigorous treatment existed for such interferometers.

Hence, a rich variety of sample and interferometer preparations is by now available for SFA experiments. The various interferometers consist of layered stacks of materials with different optical properties and calculating thin film thicknesses needs to take into account all of the layers and their wavelength dependent change of optical properties.

For SFA experiments analysis typically utilized simplified equations for interferometers with 2–7 layers, with wavelength independent optical properties. [26] A number of researchers independently developed more rigorous analysis approaches

[41, 42] based on an algorithm using a 2×2 multiple matrix method by Born and Wolf. [43] M. Heuberger extended the use of 2×2 matrix based analysis and developed a fast correlation spectroscopy (FCS) to provide fast and online analysis of interference patterns recorded in SFA. [44, 45] In this technique the maximum intensity patterns are read out and fitted to simulated spectra, and also secondary and tertiary interference patterns can be fitted. The 2×2 multiple matrix method is, however, not suited for fitting especially birefringent materials, such as mica or anisotropic fluid layers, which is often essential to SFA measurements and could open a number of new possibilities.

Recently, Zappone *et al.* [46] re-derived matrices designed for more complex fluids with continuously twisting optical parameters, and discussed a qualitative resemblance with measured spectra analyzed by peak tracking. However a somewhat different approach to evaluate transmission coefficients compared to Schubert [21] was applied in this work. Also, Kuhl *et al.* developed methods for describing layers with varying refractive indices. [47, 48]

Already in 1996 Schubert [21] derived a 4×4 transfer matrix that provides a unified theoretical approach to electromagnetic plane waves reflected or transmitted at arbitrarily anisotropic and homogeneous layered systems. This work explicitly already includes partial transfer matrices for a slab of a continuously twisted biaxial material at normal incidence, and arbitrary isotropic and randomly distributed anisotropic slabs, as well as incident and exit matrices. This approach has been applied to model only a few monolayer-thin, oxide layers formed electrochemically on various noble metals [37] using *reflcalc* [49], a direct predecessor of *SFA Explorer*.

2.4 Schubert's 4×4 Matrix Approach Adapted to MBI

In [21] Schubert presents a completed algebraic derivation using a 4×4 matrix formulation to solve Maxwell's Equations in \mathbf{k} space for use with anisotropic layered systems. While using Berreman's 4×4 differential matrices [50] as a starting point he incorporates Wöhler's optimization of using the Caley-Hamilton theorem to avoid computationally expensive row summation of Berreman's algorithm. In addition to that he also develops an algorithm to obtain 4×4 partial transfer matrices that can be mixed with matrices describing isotropic materials (in contrast to [22]).

Starting from the differential equations for in-plane components of the electric and magnetic fields derived by Berreman

$$\partial_z \Psi(z) = ik_0 \Delta(z) \Psi(z) \quad (2.6)$$

using the wave vector k_0 , the partial transfer matrix \mathbf{T}_p can be constructed by a finite

series expansion up to the power of $n - 1$, where n is the rank of the matrix:

$$\mathbf{T}_{p,\text{aniso}} \equiv \exp\left(i\frac{\omega}{c}\Delta d\right) = \beta_0\mathbf{E} + \beta_1\Delta + \beta_2\Delta^2 + \beta_3\Delta^3 \quad (2.7)$$

with the identity matrix \mathbf{E} . The scalars β_i have to obey the following set of equations:

$$\exp(ik_0q_k\Lambda) = \sum_{j=0}^3 \beta_j q_k^j \quad \text{for } k = 1, 2, 3, 4 \quad (2.8)$$

with q_i being the eigenvalues of the matrix Δ .

In preliminary tests of analytical solutions to those equations by Schubert, Wöhler [51], or using adaptations by Erbe [49] could be shown to result in non-intuitive and non-consistent values for cross-polarization terms in some corner cases. Instead of re-deriving just another analytic solution, a numerical procedure could be found to compute q_i and β_j quantities using common Basic Linear Algebra Subprograms (BLAS) routines, such as made accessible via the python module *numpy*. [52] The inherent speed gain from an analytical solution as compared to a numerical one was found to be negligible on modern computers. However, this comes at the cost of introducing a corner case for cases where the wavelength dependent dielectric tensor becomes scalar after rotation. In this case the described algorithm becomes singular (a direct result of using the Caley-Hamilton theorem) and a different solution has to be found.

2.5 Comparison of Matrix Method and Analytical Analysis

The change in analysis methodology comes with a change in analysis paradigm. Where the original analytical method by Israelachvili focused on tracking the relative positional changes of features in a spectrum, matrix method based approaches focus on simulating a complete spectrum. This comes at a huge cost of being more complex and thus inherently slower. On the other hand, when simulating full spectra the actual position of singular features loses importance, which enables analysis of cases where optically challenging interferometer layouts obstruct the formation of clear features. Hybrid approaches like Heuberger's Fast Correlation Spectroscopy (FCS) [45] precompute full spectra, then extract a distance dependent correlation map of feature positions within the spectra. [45] The effect here is to shift computationally expensive calculations, to periods during measurements where time is abundant, to allow the speed advantage of real-time tracking of features "the old way" at the cost of all benefits of a matrix based method but an enhanced precision.

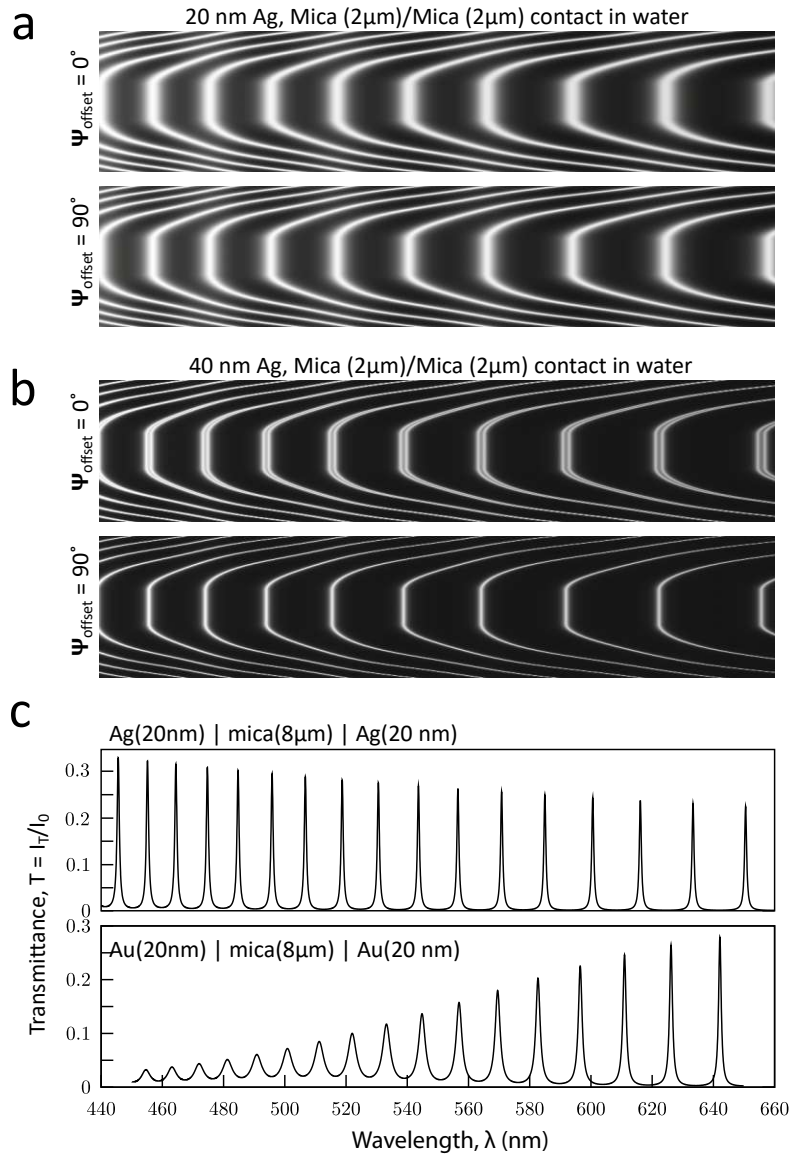


Figure 2.3: Simulated FECO for a mica/mica non-adhesive, Hertzian contact in water where the surface has a radius of curvature $R = 1$ cm using (a) 20 nm and (b) 40 nm silver mirrors, with two $2 \mu\text{m}$ thick mica lattices aligned with 0° and 90° respectively. The contact diameter is $15 \mu\text{m}$ and the dispersion in y is 450 nm/px . (c) shows the calculated transmittance of silver and gold interferometers at contact for the 20 nm mirror thickness with 90° lattice alignment.

2.6 Simulation of Typical FECO Spectra

One of the most obvious features of using full spectral fitting (coined as Complete Spectral Correlation (CSC), [10]) is the fact that the full spectra (see figure 2.3), used as fitting intermediates, can be used to predict what the experiment ahead will show if it runs as planned. Not only can this be used to time-optimize the process of measurement (especially to spot when things start to go wrong), but also immediately highlight effects that have not been anticipated during design of the experiment. This also predicts the feasibility of new measurement designs in terms of sufficient resolution, requirements and optimizations for “side parameters” such as tailoring mirror thicknesses or selecting mica thicknesses before experiment preparation. The predictive power of this has been used during experiments using a hybrid of Surface Forces Apparatus to simultaneously measure X-Ray Reflection (X-SFA) on spontaneous ordering of liquid crystals, for the design of in-situ crevice corrosion experiments, and during design of a special optical stack for better investigation of electrochemistry in SFA controlled confinements (for more details see section 2.13.1).

Another straight forward approach implemented in *SFA Explorer* is to store pre-computed spectra in a correlation table (“lookup table”). In contrast to Heuberger’s method this omits the step of isolating FECO positions while still gaining speed. This retains the versatility of a full spectrum simulation at the cost of resolution¹ and working memory.

As a demonstration of this aforementioned predictive power, figure 2.3 (a) and (b) show a simulation of a FECO pattern for a mica/mica contact in water. For generating a FECO pattern a set of spectra with increasing water thickness was calculated, and intensities were plotted to simulate a contact of two mica sheets with radii $R = 1$ cm. Figure 2.3 demonstrates that the developed code allows the simulation of the observed FECO pattern very well, including the birefringence of mica. The two apposing mica surfaces are rotated with their optical axis either aligned, or rotated by 90° in panels (a)/(b). 90° rotation results in a singlet, without any splitting due to birefringence. Alignment of the optical axis results in maximized birefringence with clearly visible doublets indicating the β and γ -fringes. It is also clearly visible, that a decreased mirror thickness results in a significant broadening of the resonant modes.

In addition, figure 2.3 (c) shows the transmittance across a silver-coated mica slab, and a gold-coated slab. First, the maximum transmittance for metal 20 nm layers is in the range of 30% (see (c)), increasing the metal thickness ((a) compared to (b)) results in the observed sharpening of FECO at the expense of transmitted intensity. Second, it can be seen, that transmittance of a silver-based interferometer decreased towards longer wavelengths, while transmittance of a gold interferometer increases (see (c)). Hence, SFA optics need to be equipped for measuring and normalizing intensity variations, if a full fitting is to be performed.

¹The resolution has to be predefined and determines the size of the table.

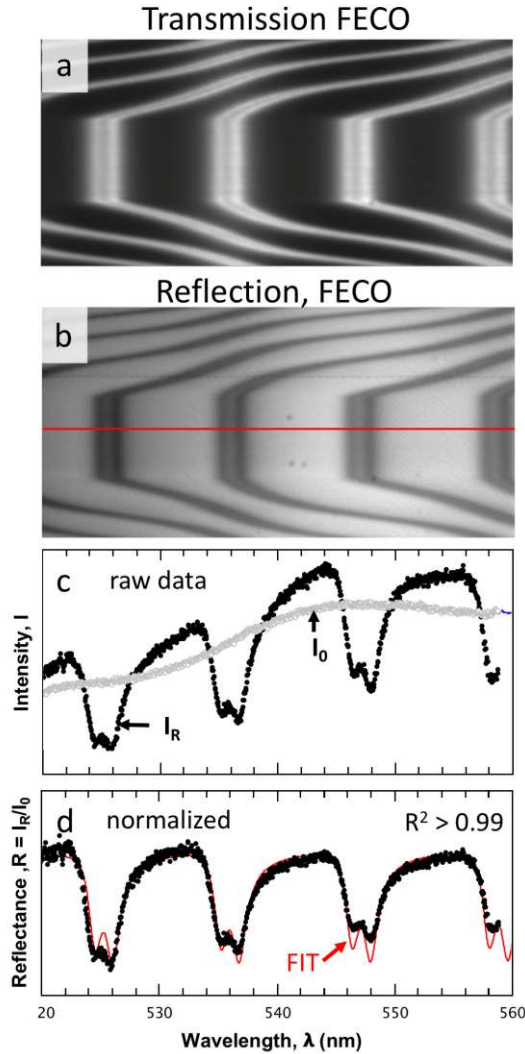


Figure 2.4: Comparison of (a) FECO recorded in transmission mode, (b) and reflection mode, respectively, for the same contact between two mica sheets with a 32 nm silver mirror at their backsides. (Recorded by Hsiu-Wei Cheng, Thanks!) The data (c), raw data) extracted from the line indicated in (b) shows the recorded intensity of the white light, I_0 , and the FECO, I_R . (d, normalized) shows the calculated reflectance, $R = I_R/I_0$, and a fit (solid red line) with a fit quality of $R^2 > 0.99$.

2.7 MBI in Reflection Geometry

Figure 2.4 shows a typical FECO pattern recorded for two equally thick mica layers in contact, coated with a 32 nm silver mirror (as fitted using the iterative process described below, section 2.10.2). This data is recorded in the newly designed optics shown in figure 2.9. It shows the first ever recorded transmission (a) and reflection (b) mode data for exactly the same contact of a standard 3 layer interferometer used in SFA. So far, only reflection mode spectra of a bulk metallic liquid facing a back-silvered mica have been demonstrated. [38] Analysis of the thickness of the mica using either the reflection mode or the transmission mode signal results in deviations of less than 0.01% of the total mica thickness.

With an optimized optics it is hence possible to work in either reflection, or transmission mode without any compromise in resolution of the spectra. This opens up a number of new possibilities for setting up SFA experiments (such as in-situ crevice corrosion or AFM absolute distance sensing (chapter 3)). It is now possible to record FECO and Newton ring in reflection mode, while leaving the room for the transmis-

sion path to perform simultaneous complementary analysis, including for instance fluorescence microscopy.

Figure 2.4 (d) also shows that the implemented 4×4 matrix approach, together with a white light correction, can effectively model spectra with high accuracy. Interestingly, recorded reflection mode FEKO show a distinctly non-Lorentz-like peak shape with considerable tailing towards longer wavelengths. This experimentally observed spectral feature strongly depends on the wavelength dependent refractive index of the silver layers, and in particular on the imaginary part. This spectral behavior cannot be simulated well with wavelength independent refractive indices, or with any other data sets for silver available in the databases and literature. This suggests that the data set that we use for silver is particularly well suited for modeling thin films of silver used in SFA experiments.

2.8 Effects of White Light Spectra

Figure 2.5 compares recorded source spectra, and spectra of the LED source recorded after transmission through the SFA optics without (I_0) and with (I_T) a 2 mm thick mica window at the position of the interferometer. The transmittance $T = I_T/I_0$ is calculated and plotted as well. Figure 2.5 shows a number of interesting aspects. An SFA spectrum recorded with the typically used tungsten halogen source increases in intensity towards longer wavelengths, due to the strongly increasing emission of the tungsten halogen source towards the red end of the spectrum. However, a simulated spectrum using a silver mirror indicates increased transmission at smaller wavelengths (see again figure 2.3).

Cold white LED sources are used, because they do not emit significant heat into the lab environment, minimizing thermal drift of the experiment. However, LED sources also impose their characteristic spectrum, also shown in figure 2.5, on the data.

First, after passing through the optics, the white light spectrum (I_0) reflects an increased intensity variation over the recorded spectral range compared to the source spectrum. Significant deviations (marked as ΔI_0) appear in the range from 500–650 nm, which is typically used for recording SFA spectra. After passing through the SFA optics the white light spectrum is a result of the convolution of the source emission spectrum, the spectrometer and the grating used, as well as the Quantum Efficiency (QE) of the sensor over the recorded wavelength range, which results in such strong deviations. The QE of the sensor used is almost constant over the recorded wavelength and only decreases gradually towards shorter wavelengths. The strong deviations are likely due to the spectrometer grating and optical elements (beam splitters etc...). Similar strong deviations are also observed in spectra of tungsten halogen sources (see figure 2.5 again).

Second, the calculated transmittance increases from about 55% at 500 nm to 70% at 650 nm. Above 650 nm the light is filtered using a low pass filter. The transmittance increases almost linearly towards the red end of the spectrum. In a first

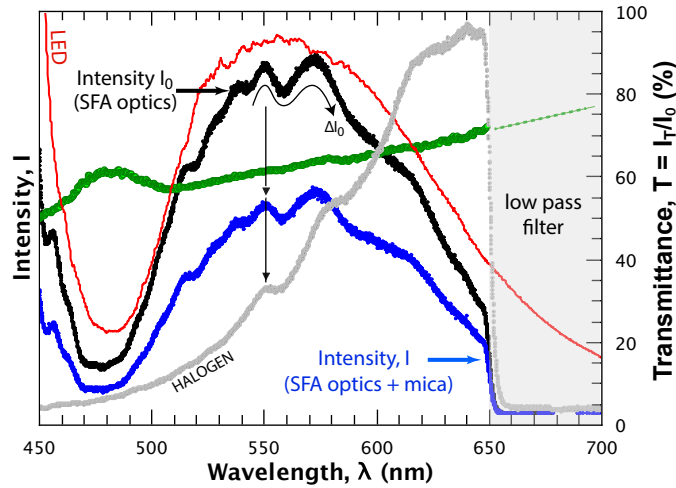


Figure 2.5: Recorded spectra after guiding a cold white LED light beam through the optical setup with (blue) and without (black) a 2 mm mica window placed at the position of the interferometer. (Recorded by Hsiu-Wei Cheng, Thanks!) Transmittance (green) and the lamp spectrum of the LED light source (red) and as reference a halogen lamp (gray) are shown and indicated (see text for details).

approximation, this suggests a weak linear wavelength dependence of the imaginary refractive index of mica with an increasing absorption of light at smaller wavelengths. For thinner mica layers in the range of the typically used $3\text{--}6\ \mu\text{m}$ the transmittance is almost constant, and mica can be safely modeled neglecting the imaginary part of the refractive index.

2.9 Effects of Layers Outside the Interferometric Cavity

2.9.1 Effects of mirror properties

Changing metal mirror thicknesses frequently occur in electrochemical and corrosion studies with the SFA, [37, 39] and a detailed analysis of an MBI pattern can provide a very detailed understanding of chemical changes at electrified interfaces. This includes the evaluation of refractive indices of *in-situ* forming metal oxides, as well as the determination of corrosion rates by direct analysis of the degrading metal mirror thickness.

However, in analytic equations [12, 26] the thickness of the metal mirror is not taken into account, and metal mirrors are treated as fully reflective with zero amplitude of propagating waves at the metal surface. This neglects phase shifts at metal interfaces, which result in shifts of standing waves if the metal mirror thicknesses change. In existing transfer-matrix based simulation approaches for MBI spectra only peak positions are analyzed [44] or qualitatively compared, [46] peak widths and intensities are irrelevant to the analysis.

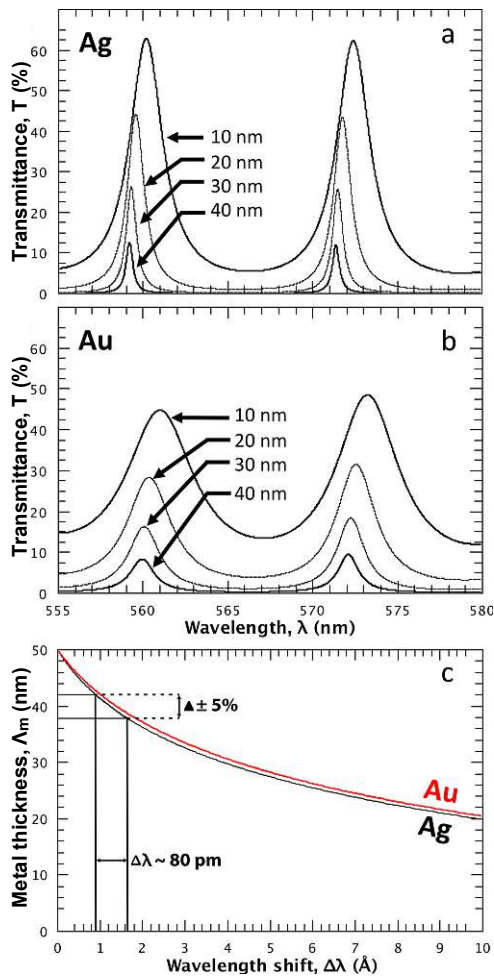


Figure 2.6: Effect of metal mirror thickness on peak shape and position for (a) silver and (b) gold interferometers. The extracted wavelength shifts are shown in (c). The spectra are calculated for a symmetric stack of two contacting mica surfaces with thickness of $4 \mu\text{m}$.

In contrast, a full fitting approach allows to directly analyze mirror thicknesses and resulting effects in MBI spectra. Figure 2.6 shows simulated spectra of a mica/mica contact ($4 \mu\text{m}$) for an increasing thicknesses of (a) silver and (b) gold mirrors, respectively. First, comparing silver and gold spectra this data shows that gold mirrors result in a significantly broader FECO pattern. This is due to the significantly higher imaginary part of the refractive index (especially light absorption) of gold in the visible range. Second, upon decrease of the mirror thickness both silver and gold show the expected increase in transmittance in combination with a significant wavelength shift of up to 1 nm for very thin mirrors. In a previous work, it could already be shown how transmittance can be used to estimate the corrosion rate of a mirror used in an MBI experiment. [39]

More interestingly, in the context of this work, figure 2.6 (c) also shows the mirror thickness plotted versus the wavelength shift. The characteristic shape of this plot suggests a larger influence of mirror thickness changes for thinner mirrors. It could also be estimated that a 5% variation in the thickness range typically used in a SFA experiment can result in up to 80 pm wavelength shift. This is an interesting result as 5% over 1 cm of sample is a typical homogeneity obtained by an ideal PVD process (rotating sample, ideal impact angles, ...). This suggests that changing the contact position, which is a typical practical procedure in SFA, can result in considerable absolute distance errors. Using the analytic equations or peak correlation approaches. According to analytical equations [26] for even and odd fringes, a wavelength shift maximum of 80 pm (estimated as 3σ of a Gaussian distribution) results in an average shift of $\pm 7 \text{ \AA}$ / $\pm 5 \text{ \AA}$ for odd/even fringes, respectively.

This does not seem significant, and may be safely ignored for measurements where molecular dimensions (sub 1–2 nm distances, or layer thicknesses) are not approached or studied. However, for hydration force measurements, self-assembled monolayer thicknesses, or for measuring oscillatory behavior of molecular fluids it is, therefore, essential to carefully analyze, and if necessary, fit the mirror thickness. Otherwise data has to be reported with an average absolute error in the range of molecular dimensions.

In typical experiments a number of interesting aspects could be found. First, silver mirrors are typically about 20% thinner compared to deposited thicknesses of 35 nm measured using a quartz balance in a well calibrated PVD. This is very likely due to significant oxidation of the silver after exposure to ambient environment, and during heat or UV curing of glues used to attach mica sheets to the cylindrical glass discs. Typical oxide thicknesses on silver are in the range of 2–10 nm depending on the exposure conditions to oxidizing environments. [53, 54] Second, upon changing a contact position we usually find only about 2% mirror thickness variation, suggesting that PVD processes may be slightly better than quoted by PVD manufacturers (see materials and methods), or degradation during gluing may, to some extent, level out initial roughness.

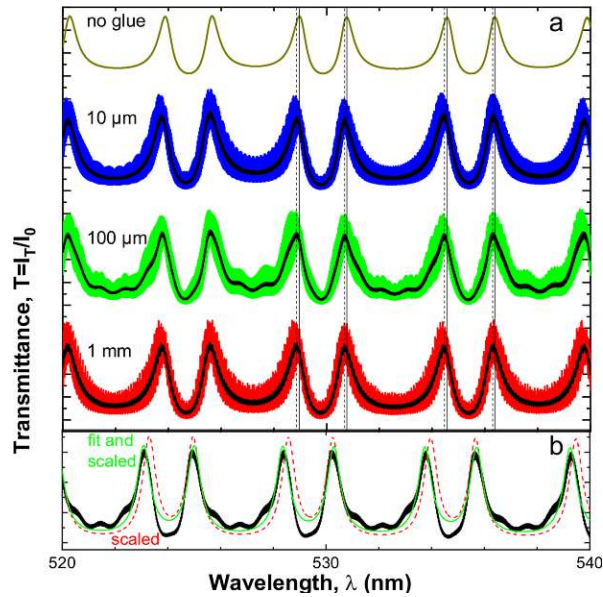


Figure 2.7: Simulated spectra for an interferometer formed from layers as seen in figure 2.1, in (a) a spectrum has been simulated without any supporting layers (no glue) and others with a 3 mm glass layer and varying thicknesses of glue layer (NOA81[55]), topped with mica and with a water layer as the gap medium of 20 nm. Colored lines are data simulated with a resolution of 200 points/nm and the black line is a 10 point moving average to replicate the spectrometer resolution. Vertical lines have been added at the FECO maxima of the no glue case (solid lines) and the 100 μm (dashed lines) to illustrate the small shift in position of the FECO and the change in splitting between β - and γ -fringes. The largest shift occurs upon introduction of a glue layer, minor variations as a function of the glue layer thickness are within the typical SFA noise level (see text). (b) is the same interferometer with a 100 μm glue layer without a gap layer ($\Lambda_{\text{gap}} = 0$). Displayed data (black) is with the same resolution after smoothing the high order oscillations in (a). The data has been fit with the model without supporting layers, first with the same interferometer layer parameters as used for the simulations (scaled, red dashed line), and second with allowing the mica thickness and birefringent splitting parameters to fit freely (fit and scaled, green line).

2.9.2 Effects of Supporting Glue

So far, all simulation and analysis approaches in SFA ignored the effect of supporting layers outside the actual interferometric cavity, namely glue layers and fused silica discs, which encase the cavity. Only recently, glue layer effects were inspected in terms of relative peak ratios for a special 3-mirror interferometer.[56] An important question for judging the absolute accuracy of an SFA measurement is however, how much varying support layer thicknesses may shift the measured resonances. Experimentally, specifically the glue thickness is virtually impossible to control within a sub-micrometer uniformity. Glue layers may not have similar thicknesses for both supporting layers, and they may change significantly during change of contact positions, which is a standard procedure in SFA, specifically if additional layers are

introduced. In such a case, it is essential to unmount/remount a sample and with high certainty a slightly different contact point will be established. Resulting, artificial shifts will result in a significant absolute error. Here we quantify the extent of this systematic error.

Figure 2.7 investigates the effect of the glass and a varying glue layer (see again figure 2.1 (c)), to evaluate principle effects on the patterns in the data. The support layers impose a difference in the refractive index transitions between the interferometer and its environment.

For comparison a typical 3-layer (mica/mica) interferometer has been modeled with and without the supporting layers. Figure 2.7 (a) shows simulated spectra without any supporting layers (no glue), as used above, and for different symmetric glue thicknesses with a refractive index of 1.56 typical for UV-curing hard epoxy glues after curing.

Figure 2.7 (a) compares the interferometer with and without out support layers and how resulting spectral positions of the FECO shift and how the $\beta - \gamma$ splitting varies.

First, due to introduction of a glue layer all peaks show a relative shift to lower wavelengths, which is due to the change of the phase shift compared to modeling with a semi-infinite layer of air.

Second, the $\beta - \gamma$ splitting introduced by the birefringence of the mica appears to increase with the presence of the supporting layers as well. This can also be attributed to the differences in refractive indices at the additional interfaces, resulting in different phase shifts.

Third, additional weak interference patterns of two different orders are superimposed compared to the spectrum with no glue and glass layer: A high order interference arises from internal reflections within the glass support, and a lower order modulation from the reflections between the mirror and glass across the glue layer. As can be seen in all spectra simulated with glue, the high order signal superimposes a pattern oscillating with a 0.001 nm periodicity (not visible with the plotted magnification), which is independent of the glue thickness. This signal arises from the 3 mm thickness of the glass disks. The generated pattern is however not detectable in recorded spectra due to the resolution limitations of the spectrometers, which are in the range of 0.02 to 0.04 nm (depending on exact settings). To replicate this limitation a moving average of the simulated high resolution data (solid lines in the figure) was used. As shown, the data indicates that the 3 mm thick glass surfaces have a very limited influence on spectra, below the typical noise level of SFA.

Asymmetric glue thicknesses superimpose an additional pattern onto the variability of the intensity of the supporting layer interference patterns. There is a shift in the patterns across the spectrum with increasing difference between the two glue layer thicknesses (see figure 2.8).

Hence it can be concluded that simplifying the interferometer to a free floating unit in air, especially without supporting layers, introduces an inaccuracy in the fitted parameters. In figure 2.7 (b) this inaccuracy is quantified and the fitting of the simulated

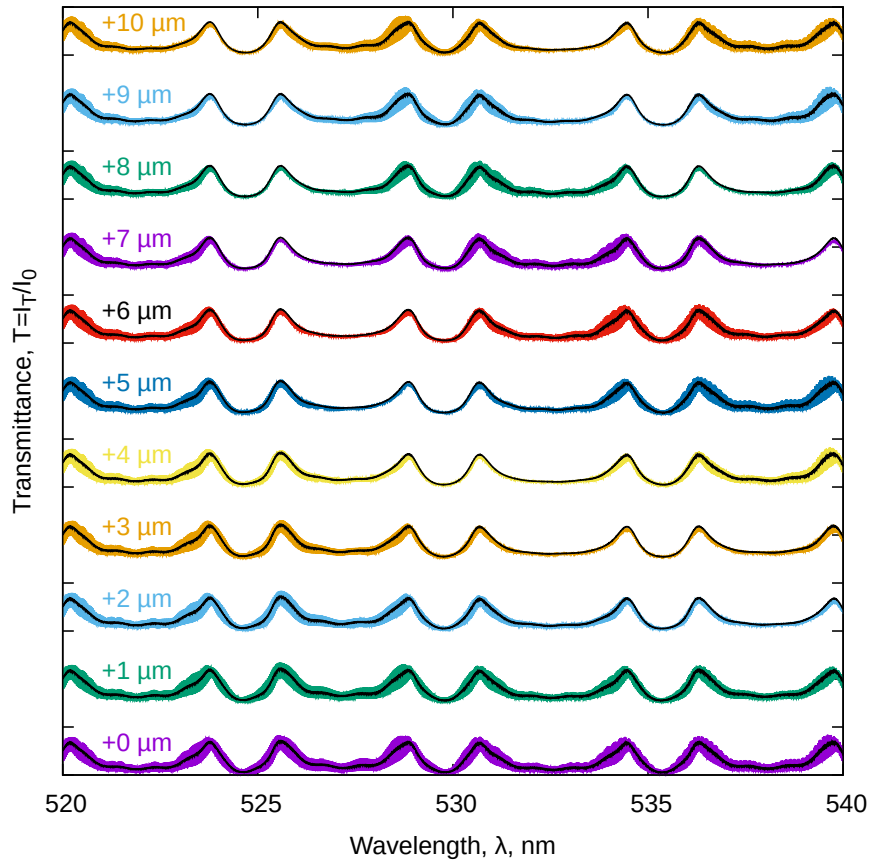


Figure 2.8: Simulated transmission spectra for a { air | glass (3 mm) | glue (100 μm) | Ag (30 nm) | mica (8000 nm) | H₂O (20 nm) | mica (8000 nm) | Ag (30 nm) | glue (100+x μm) | glass (3 mm) | air } interferometer (colored), including 10 point moving average (black). Additional intensity changes can be seen in the patterns that are superimposed onto the spectra by the inclusion of the supporting layers. The changes move through the spectrum as the glue thickness asymmetry increases.

data from an interferometer including the supporting layers using the free floating interferometer model considered as fitting model. Keeping the fitting parameters of the free floating interferometer identical to the layers set in the simulated data (scaled, red dashed line) the fit quality is clearly decreased.

If mica thickness and birefringent splitting parameters are allowed to fit freely (fit and scaled, green line), a good fit can be achieved. The resulting mica thickness is fitted as 7998.64 nm instead of the expected 8000 nm which corresponds to an error of 0.02%. At the same time the birefringent splitting increases from 0.0052 to 0.0060 which corresponds to an error of approx. 15%.

The difference in mica thickness is therefore rather small and negligible (for non-complicated interferometer layouts) and the influence on the birefringence can be compensated for by adjusting the effective birefringence. The effective birefringence will be smaller by a factor of approximately 15%, if glue layers are not included in the simulation explicitly.

The simplification of using a free floating interferometer provides the benefit of a reduced computational cost, compared to including the supporting layers, for minimal systematic error introduction. Also, in experiments the glue thickness is not controllable after all. As such, choosing a glue that has a refractive index closer to, or is matching, the fused silica disc n will be ideal, however such glues are unfortunately often too soft for SFA purposes.

The central quantity for estimating a resulting systematic error of such a simplification is the absolute shift of peaks for a case with asymmetric glue layers. Asymmetric glue layers are the most likely experimental situation. A shift of a peak position due to contact position changes may be interpreted as a thickness change of a confined layer, although it may simply be the result of a move of the contact position and hence change of the *local* glue layer thickness. We evaluated peak positions at three different wavelengths in the green, yellow and red wavelength ranges of the spectrum. The data suggests that the variation of the absolute peak positions of an explicit glue model are in the range of ± 0.01 nm in the green, and up to ± 0.04 nm in the red wavelength range above 600 nm upon change of the glue thickness. Hence, in the green region the error is clearly below the detection range of a typical spectrometer with a 0.02 to 0.04 nm resolution (depending on camera pixel size, grating and spectrometer focus length), while it may become detectable at higher wavelengths. According to simplified equations for even and odd fringes,[26] a wavelength shift of 40 pm translates into a maximum detectable relative distance shift of 2 to 3 Å.

2.10 Further Improvements to the SFA Technique

2.10.1 Improved Optical Path

Figure 2.9 describes the implementation of both standard transmission mode operation and reflection mode operation, means to provide *operando* normalization of data

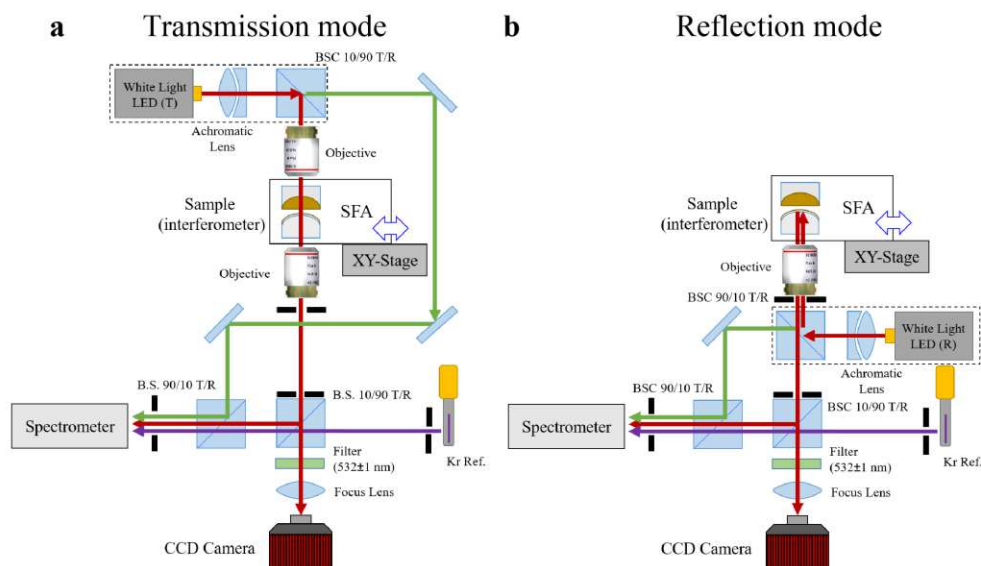


Figure 2.9: Newly designed modular optics for recording **(a)** transmission mode and **(b)** reflection mode spectra, simplified *all-perpendicular* beam alignment and simultaneous FECO and microscopy recording. Red lines indicate the white light path through the interferometer into the camera/spectrometer. The green line reflects the white light reference path and the mercury reference is colored in purple. Important optical elements such as beam splitter cubes (BSC), as well as irises for beam alignment are indicated (see text for details).

by white light reference spectra, and simplification of alignment of optics. Specifically, figure 2.9 compares the optical path designed for SFA experiments in **(a)** transmission, and in **(b)** reflection mode, as detailed in the figure. This setup introduces two essential and novel aspects.

First, in classic SFA experiments, [24–26] the optical system is composed of a white light source, heat filter, the SFA chamber, a free standing microscope and one or two prisms to guide the light path emerging from the microscope into to a spectrometer. Perpendicular beam alignment is in fact very tedious and error-prone in such a setup. Small deviations from a perpendicular light path can however result in often significant distance shifts. Specifically, if a contact position is changed within an experiment, which is a frequent procedure, realignment of the path results in artificial shifts of the recorded wavelength and hence distance in the 0.5 to 1 nm range. Furthermore, finding a contact position and re-alignment of the optics requires significant training. The upgraded optical system presented here, figure 2.9, fixes all optical paths using a standard cage system, which can be aligned perfectly perpendicular using a set of irises and beam guides. As a result, only the established contacts (as in interferometric cavities) are moved into the center of the optimized optical path, as indicated by the red line in figure 2.9. For this, the SFA itself is mounted on a x/y translation stage. This simplifies the optical alignment of the SFA considerably. As soon as any established contact position is moved into the center position, both FECO and Newton’s rings recorded with the spectrometer and camera, respectively,

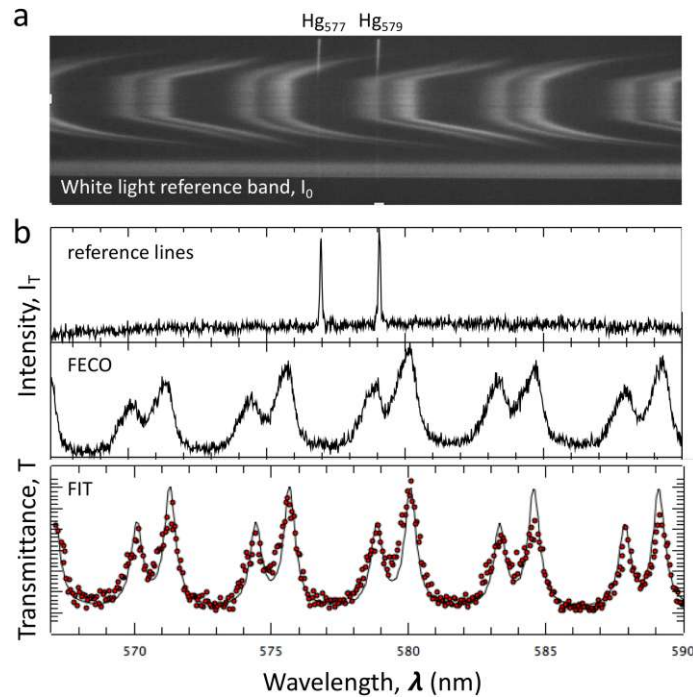


Figure 2.10: **(a)** FECO recorded for a mica | mica contact in water. The spectrum also shows the simultaneously recorded white light reference band and the reference lines. Paths for these beams are translated and shaped so that they do not interfere with the FECO recorded in the center of the sensor. **(b)** Intensity profile of FECO in contact, as well as calculated transmittance $T = I_T/I_0$, along with a fit (solid line) using the 4×4 transfer matrix approach.

are immediately observed. This simplifies searching for contact positions and even provides a pathway for automating the approach and alignment procedures. The optical system also provides a flexible platform for easily adding new capabilities such as fluorescence microscopy [57] or laser interferometry. [58–60]

A second important addition to existing SFA optics is the simultaneous, yet fully decoupled, measurement of reference lines and the white light source spectra. For this beam paths are included, guiding 10% of the white light, and a reference light, directly into the spectrometer. Both beams are laterally translated and shaped using translating pinholes and slits. Lateral translation of the reference and white light beam allows us to project these beams at the upper and lower halves of the sensor, while the MBI signal is projected into the center of the sensor. As a result, and as shown in figure 2.10, those reference lines, white light spectra and FECO can be simultaneously recorded. This procedure eliminates any fluctuations of the source during data normalization. Specifically, if the source fluctuates, both FECO and white light spectra similarly fluctuate, maintaining the transmittance constant.

All data shown below is normalized by an appropriate reference white light beam, to allow for a full fitting of the entire spectra.

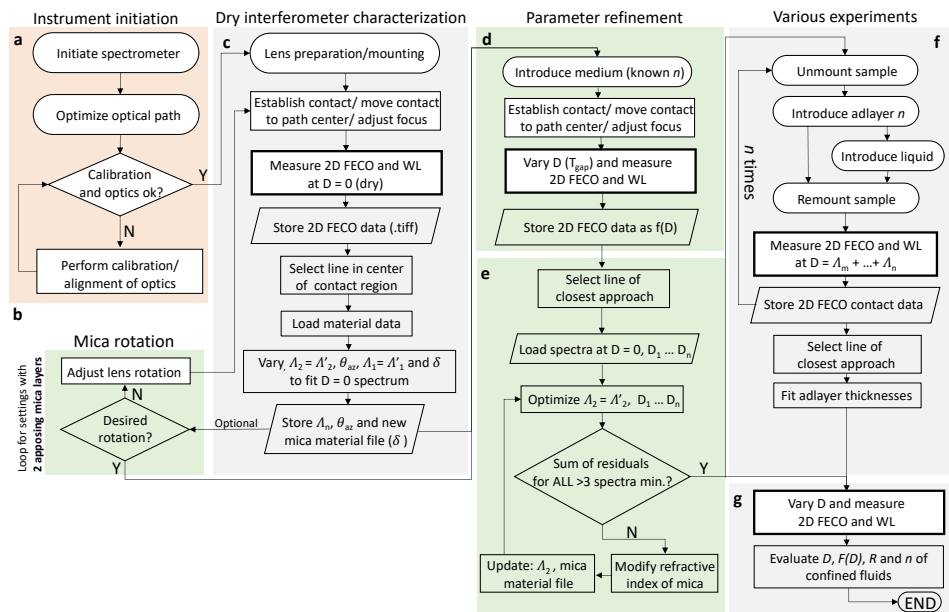


Figure 2.11: Suggested flow chart of an SFA experiment. **(a)** Instrument initiation. **(b)** Rotation of lenses to adjust for relative azimuthal angle of apposing micas in a mica vs. mica experiment. **(c)** Characterization and analysis of dry interferometer ($D = T_{gap} = 0$) and initial optimization of mica parameters. **(d)** Recording of and **(e)** optimization of mica thickness and refractive index based on measurement and analysis of spectra with defined gap thicknesses of a medium (for example water or air) with known and isotropic refractive index. **(f)** Consecutive experimental introduction and analysis of any number of n add layers and their thicknesses and refractive indices. **(g)** $F(D)$ measurements and other experiments.

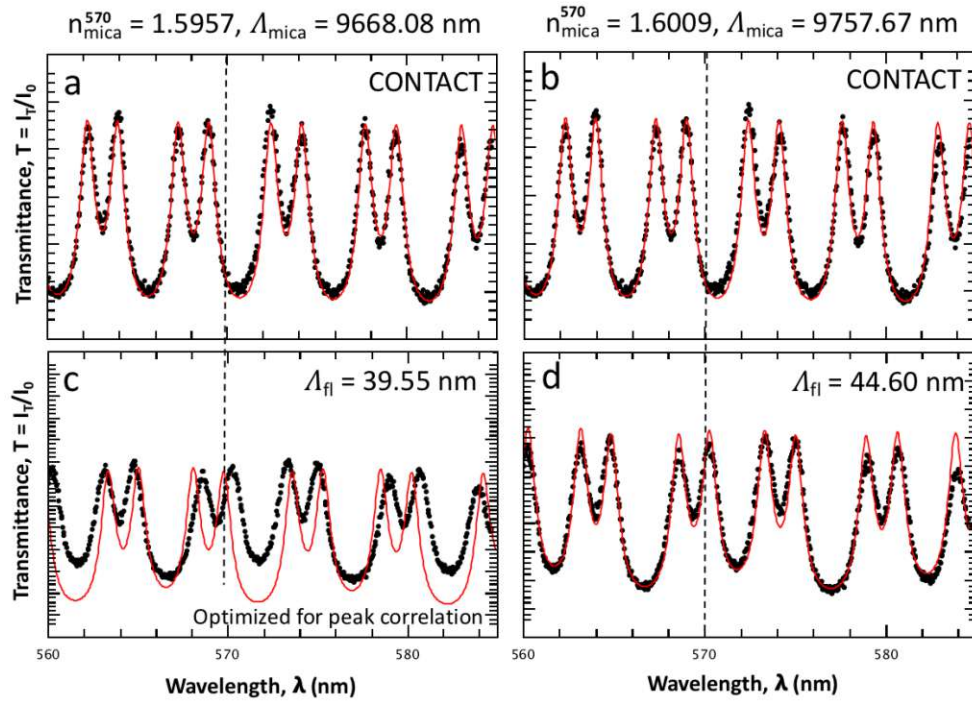


Figure 2.12: Typical experimental data and fitted spectra for the same experimental data (a)/(b) at contact of two similarly thick mica sheets, and (c)/(d) with a fluid (water) gap separating the two mica sheets. The fit is shown as a solid red line, data is plotted as points. The mica refractive indices of the γ -fringe at an example wavelength of 570 nm, the mica thickness (Λ_{mica}) and fluid gap thickness (Λ_{fl}) are fitted quantities. The dotted line is a guide line for the eye (see text for details).

2.10.2 Determination of Mica Optical Properties

The absolute refractive index of the specific mica sheet used in experiments is a concern, regarding absolute measurements of distances and layer thicknesses in SFA experiments. Muscovite mica is a birefringent natural material, which has a reported birefringence of $\delta = 0.0035$ to 0.0052 with refractive indices in the range of $n_{\beta} = 1.52$ to 1.62 and $n_{\gamma} = n_{\beta} + \delta$ at 570 nm. [61] It is common practice to use fixed values for the mica refractive index in the range of $n = 1.56$ to 1.60 with a fixed β and γ splitting as measured in experiment. [12, 25, 26, 44, 46] Using tabulated fixed values will result in errors in the determination of the absolute thickness of mica. This error will translate into errors in the determination of distances, specifically if an additional gap layer such as water is present. An independent measurement of the refractive index for the actual mica sheet used in an experiment seems useful, and is possible by a simple iterative fitting approach, as shown in the flow chart in figure 2.11 (d-e).

In particular, figure 2.11 (e) shows how the refractive index of mica can be fitted iteratively for a symmetric three layer experiment using a set of spectra with isotropic finite gap layer thicknesses.

Figure 2.12 (a) and (b) show a mica spectrum, and the corresponding fitting of the spectrum using two refractive indices within the reported window at 570 nm. Clearly, and as shown in figure 2.12 (a) and (b), both refractive indices fit the data equally well if no gap layer is present. In contrast, and as seen in (c) and (d), as soon as a water gap of about 45 nm is introduced experimentally, only one refractive index fits the data well, even if the difference is only $\Delta n = 5 \times 10^{-3}$. As such, an iterative fitting of mica refractive indexes at $D = 0$ and at one or more larger distances, with a material in the gap with a precisely known isotropic refractive index, provides a direct *in-operando* possibility to accurately measure the mica refractive index of the sheet used in a particular experiment with an accuracy of $\Delta n = 0.0002$.

Interestingly, the fitted mica thickness is off by less than 1%, while the fluid layer thickness in a three layer interferometer displays a considerably larger error of up to 10%. Also, a close inspection of the fits indicates that specifically the even order maxima are highly sensitive to the mica refractive index, due to the finite and larger amplitude during propagation across the mica | water | mica interface. At the same time, this also suggests that a simple tracking or correlation of maxima is prone to 10% error for layer thicknesses above approximately 20 to 30 nm since only maxima are tracked or fitted, irrespective of the analysis method used. The mica refractive index must be fitted, in order to achieve the possible sub-nm absolute accuracy resolution of SFA also at larger distances.

2.10.3 Rotation of the Mica Lattice for Symmetric 3–5 Layer Interferometers

Further, the birefringence of mica was tested in terms of evaluating relative rotations of two equally thick apposing mica slabs. The code was implemented in such a way, that the rotation of two birefringent materials can be fitted to the expected spectrum. At each iteration of the fitting routine a new rotated transfer matrix is computed for one of the two layers, using the numerical approach described above.

For qualitatively testing the performance, two opposing mica layers were rotated by about $10^\circ \pm 2^\circ$ around the azimuthal axis. Afterwards we recorded a contact in solution. Figure 2.10 indicates observed characteristics of the FECO pattern and transmittance. First, rotation of the lattices is directly reflected into the intensity of the β - and γ -fringes. Here, the β -fringes show a significantly decreased intensity, and a slight shift of the wavelength of both β - and γ -fringes towards the average wavelength of both. Using the implemented 4×4 transfer matrix method we can fit the rotation of the apposing mica lattices, and find an effective rotation of 12° . This matches the value targeted by the alignment of the apposing sheets. Hence, evaluating the mica birefringence in terms of intensity *and* peak position allows us to directly extract the relative rotation of mica lattices facing each other. This is an aspect that cannot be fitted using a peak-correlation algorithm, simply because the information is obtained from the relative intensities. Commonly used peak correlation algorithms

will interpret this result as a small change of the mica birefringence, which is equivalent to the wavelength shift of β - and γ -fringes. Hence, relative rotations of mica layers can not be ignored in an analysis without introduction of significant absolute and relative errors.

2.11 Validation of Matrix Method MBI Analysis

2.11.1 Thickness of Confined Molecular Layers, Radius Calibration and Force Distance Characteristics

Figure 2.13 summarizes the performance of the new optics and the 4×4 matrix analysis for the essential standard SFA experiment. Here, a force versus distance measurement and analysis of a supported lipid monolayer facing a mica surface is performed. For this purpose, the lipid layer is supported with an inner hydrophobic SAM on gold, followed by Langmuir-Blodgett-deposition of an outer layer of the neutral Dipalmitoylphosphatidylcholine (DPPC) lipid, which together can be described as a bilayer-type structure, referred to as a bilayer for simplicity. This is a benchmark experiment in many respects, as it involves a number of critical steps in the analysis and experiment, which are summarized in the flow chart of an SFA experiment figure 2.11 (f).

First, an initial contact referencing for a clean mica gold contact is performed.

This is followed by removal of the gold disc from the SFA chamber for a >12 h thiol deposition. After successful thiol deposition the gold, now coated with a self assembled monolayer, is transferred back into the SFA chamber for measuring the thickness of the SAM. Here, a consistent thickness of 1.2 ± 0.2 nm could be found taking into account all aspects mentioned above. This agrees very well with reported thicknesses and tilt angles of this particular SAM and ellipsometry data of such thin films. [62–65]

It should be noted that transfer out of the system is critical as a realignment of the contact with the optical path is necessary again. Using the newly designed optics (figure 2.9), only a newly established contact has to be moved back into the optimized beam path, and no errors can occur.

After establishing the SAM thickness, the SAM-covered gold is transferred to the LB-trough for the DPPC deposition. The deposited DPPC layer is transferred back into the SFA chamber under fully wet conditions, and the thickness of the constructed bilayer in solution and the force versus distance characteristics are measured. The force versus distance characteristics in figure 2.13 indicate a long range electric double layer repulsion that can be fitted well using a DLVO model. As expected, the data indicates a jump into a very adhesive contact, with a stable hard wall at the distance D that equals the thickness of the hydrated bilayer slab.

The measured and analyzed thickness of the SAM/DPPC layer is 3.2 ± 0.3 nm, indicating a hydrated DPPC thickness of 2 ± 0.2 nm, which agrees very well with

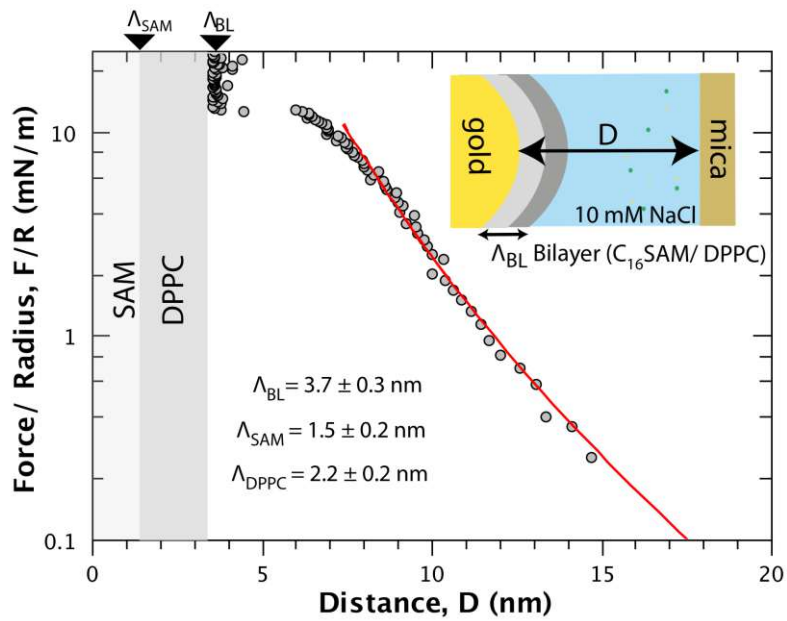


Figure 2.13: Force versus distance characteristics of a lipid bilayer-type model facing a bare mica surface in 10 mM NaCl solution. (Measured by Pierluigi Bilotto. Thanks!) The schematic details the optical layer (interferometer) setup in this experiment. A molecularly smooth gold surface is modified with a hydrophobic hexadecane-1-thiol SAM, followed by coating with an outer DPPC layer in the gel phase. The distance $D = 0$ is defined as contact between gold and mica in dry nitrogen. The SAM thickness T_{SAM} and bilayer thickness T_{BL} are indicated (see text for details).

previously observed and measured single layer thicknesses in a hydrated neutral bilayer. [48] An aspect worth mentioning is, that we also optimized both refractive index and thickness of the established molecular layers using the iterative fitting approach described above, and find that refractive indices of $n = 1.478$ for the molecular ordered thin films describe the observed spectra best. [66]

In a standard SFA setup, the interferometer is not sensitive to detect differences of in-plane/out of plane refractive indices of confined lipid like films.

Simulations (see figure 2.14) indicate peak shifts below the detection limit, if the refractive index is considered as non-isotropic with refractive index differences of 0.04 for lipids. Hence, the data is described equally well using an isotropic refractive index for the organic thin films. For materials such as liquid crystals, with refractive index differences of up to 0.2 for in-plane and out-of-plane, it is possible to distinguish anisotropy in confined thin films down to sub 10 nm gap thicknesses D .

2.11.2 Refractive Index of Fluids Confined Into a Crevice

While the SFA is not sensitive to small changes of in-plane and out-of-plane refractive indices, it is very sensitive to isotropic refractive index changes of confined fluids down to molecular dimensions. Therefore, refractive index changes of fluids confined into a crevice generated using the SFA have been fitted.

This is a very interesting question in many fields, including crack propagation in stress corrosion cracking, where fluid properties at the crack tip are unknown, or for crevice corrosion, where fluid compositions within a crevice are often composed of salt solutions with concentrations close to saturation levels.

Figure 2.15 (a) shows a cross-section across an established contact between two mica sheets. Figure 2.15 (b) shows a typical FECO pattern recorded, and rotated by 90° to resemble the cross-sectional view.

After establishing a contact, cyclohexane was introduced and >1000 FECO patterns recorded with 10 frames/second. Figure 2.15 (c) shows the result of simultaneously fitting both the real part of the refractive index, and the fluid thickness (that is the gap thickness) using the implemented CSC, when going from the fully confined zone towards the gap opening as indicated in figure 2.15 (a).

As previously described by Heuberger *et al.* [68] a considerably lower refractive index was found at small fluid thicknesses, with an average (over 1000 frames, which corresponds to 100 seconds measurement time) that decreases to a value close to $n = 1$ at $\Lambda_{\text{gap}} = 2$ nm. This has previously been explained as a decreasing density, for example gas-like behavior, which is similarly confirmed by this data.

Interestingly, and also similar to observations by Heuberger *et al.* [44] an increasingly broad refractive index distribution was found when going to small gap openings. This is consistent with the interpretation of considerable density fluctuations of the highly volatile cyclohexane when confined between two opposing hard walls. However, at gap thicknesses below 2 nm unexpected large variations resulting in refractive

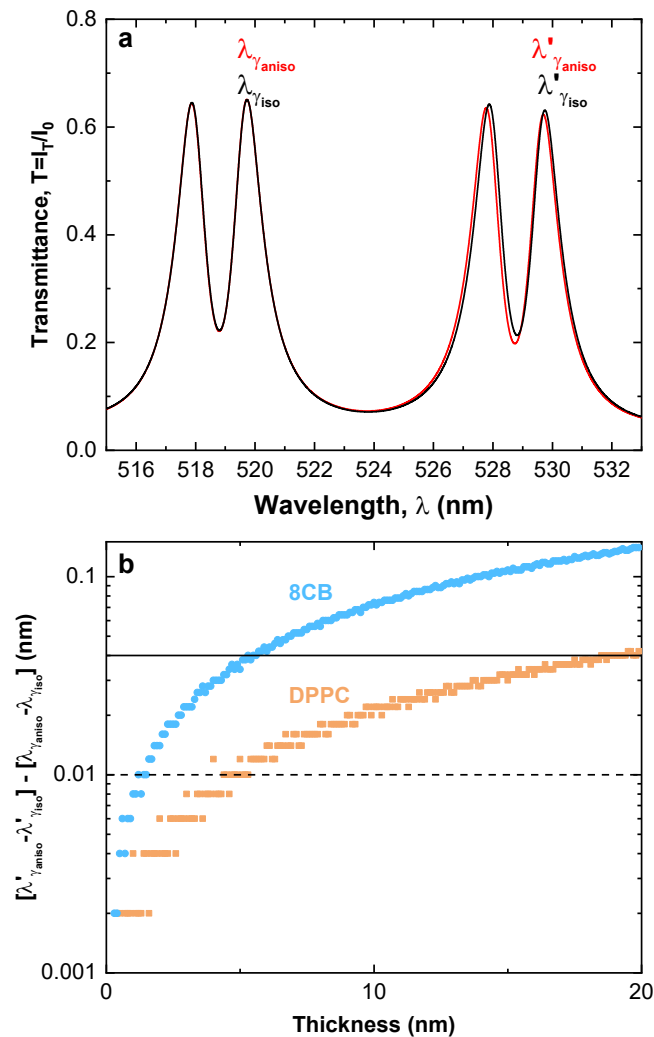


Figure 2.14: Simulations to determine the detection limit of the apparatus for anisotropic thin layers under confinement. **(a)** Simulated spectra of a 50 nm of material with the properties of DPPC (lipid) confined between two mica sheets. For the black spectrum a mean refractive index of 1.4982 was used simulating isotropic behavior, whereas for the red spectrum the birefringence of DPPC was applied with 1.4704 for the in plane component and 1.526 along the optical axis with a typical tilt angle of 30° . [67] The peaks shift in position between the isotropic and anisotropic spectra by different amounts for the odd and even fringes. The difference between the spectral positions of anisotropic and isotropic γ fringes of the same order has been calculated and then compared with the equivalent difference of an adjacent γ fringe in **(b)**, orange points). The same process has been applied to the liquid crystal 8CB **(b)**, blue points) which has a larger birefringence than the lipid, the isotropic average refractive index used was 1.595 and for the anisotropic case $n_e = 1.68$ and $n_o = 1.51$. The solid horizontal line represents the conservative estimate of our spectral resolution of 0.04 nm (see section Implementation of 4×4 Matrix Method for Multiple Beam White Light Interferometry in the appendix, page 65). The dashed line represents a more optimistic spectral resolution of 0.01 nm which could be achieved with appropriate optical component choices. The thicknesses at which the anisotropy of thin films can be resolved are therefore where the simulated difference in shifts are above the spectral resolution lines.

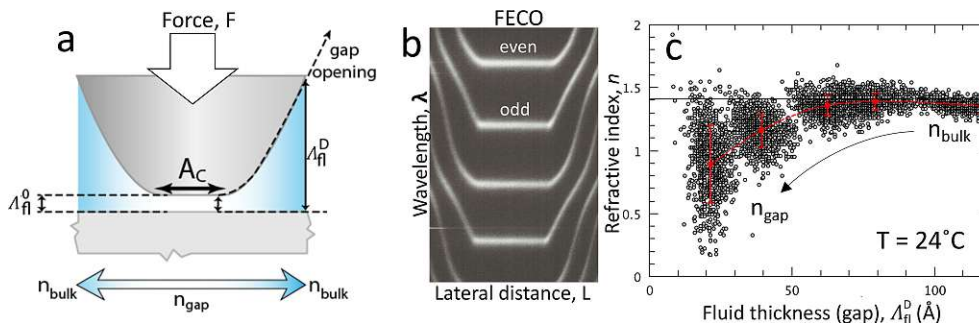


Figure 2.15: **(a)** Schematic of a contact established in cyclohexane, indicating the contact area A_C , the fluid thickness T_n in the gap, and in the gap opening where the surface-to-surface distance increases to T_n^D . **(b)** shows the FECO pattern recorded and rotated to resemble the schematic in **(a)**. **(c)** shows the simultaneous fit of the real part of the refractive index \tilde{n} and the distance D as a function of the fluid thickness in the gap opening. The data was recorded at 24 °C and the bulk cyclohexane refractive index is indicated. A clear decrease in n and increasing fluctuations at smaller gap sizes are observed.

indices and standard deviations were found that extend well below 1.0. This may be due to a break down of continuum theory at such small gap thicknesses, or due to reaching resolution limitations for relative peak shifts in the range of 0.02–0.04 nm spectral resolution in our systems.

In summary, MBI provides a very detailed view into fluids confined into a gap or crack. The 4×4 matrix approach, together with a full fitting of FECO data, can provide refractive indices of nanometer confined fluids, with the possibility to include anisotropic layering that may arise in particular during confinement. Figure 2.14 simulates expected spectral differences due to a change from an isotropic to an anisotropic thin film, with typical anisotropic refractive indices for a liquid crystal and a lipid layer. Relative peak shifts of even and odd ordered fringes with respect to each other approach the conservative estimate of spectral resolution of 0.04 nm at film thicknesses of 20 nm for lipids, and about 6 nm for liquid crystals. However, SFA may be sensitive to anisotropic refractive indices of monolayers of liquid crystals of 2 nm thickness and lipid layer thicknesses of 4 nm only if a resolution limit of 0.01 nm is achieved. This is possible with appropriate choices of optical components.

2.12 Discussions and Conclusions

2.12.1 Practical Implications for SFA Experiments

Based on the above data and analysis, a number of practical guidelines for performing SFA experiments can be extracted. These can be summarized as follows.

1. An optimized SFA experimental and data flow/analysis flow chart is shown in figure 2.11. The general procedure for obtaining best fitting results of experimental data is to first optimize azimuth angle, birefringence, mirror thickness

as well as initial mica thicknesses from a contact measurement using an initial guess of the mica refractive index.

2. Azimuthal angles of apposing micas and birefringence can be directly interpreted from a visual inspection of the peak splitting which enables a close approximation to be input in the initial fitting parameters. Relative intensities of β - and γ -fringes indicate the relative rotation of the mica layers, and birefringence is a direct measure of the β - γ splitting.
3. The mica refractive index and the resulting mica thickness can be refined to an accuracy in the 4th digit for the individual mica sheets, using a set of spectra with an added isotropic gap layer. Since mica is a natural material with considerable variations of the refractive index, it is recommended to fit the refractive index. Only this provides an absolute evaluation of layer thicknesses, specifically at larger separation distances. Variations from 1.52 up to 1.61 depending on the batch of mica could be found, with most micas being in a smaller range around 1.58 ± 0.02 .
4. Upon change of contact positions, an accurate fitting of the metal mirror thickness can eliminate systematic errors due to small variations in the metal mirror thicknesses. In addition, using a fixed and aligned optical path, and a translation mechanism for moving established contacts into the beam path (described in figure 2.9) minimizes systematic errors due to small deviations of optical alignments after for example contact position changes.
5. It is useful and often essential (especially in reflection mode operation or with metal mirrors that can corrode) to simultaneously record a white light reference spectrum for providing normalized data analysis of full spectra. This can be easily achieved using an optical path described in figure 2.9.
6. Glue layers can be safely neglected in a simulation approach in the green and yellow wavelength region as long as a spectral resolution below 0.02 nm is not achieved.

2.12.2 Accuracy and Potential for Automation and Real-Time Analysis

The typical fitting error of a full spectral fitting is in the range of 0.09%, for a mica thickness of 10 μm . The determination of a bilayer thickness from a single experiment results in a standard deviation of 50 pm. Fitting a full spectrum for an ideal layer thickness and isotropic refractive index within a small window typically requires that about 10 to 20 spectra are calculated and fitted. As a result a full fitting approach is inherently slow, with possible frame rates in the range of seconds. This is clearly too slow for a typical video acquisition rate of 10–30 Hz for SFA spectra. Here, the fast correlation spectroscopy and analytical equations analyzing only wavelength maxima

provide a fast and straight forward solution, with the discussed caveats of not fitting intensities and peak shapes. However, this may be combined in a post-experimental analysis.

In order to speed up online analysis, we implemented a fast full spectral fitting approach based on a *look-up table* approach. Such an approach provides a simulation of all possible spectra within a given grid of refractive indices (Δn) and layer thicknesses ($\Delta \Lambda$). This takes about 20–30 mins to compute on a standard desktop PC and much less on a supercomputer, using a window of interest for a typical SFA experiment with $\Delta n = \pm 0.50$ and $\Delta \Lambda = 0.00$ to 100.00 nm. The resulting 2–5 MB look-up table that can be easily stored in memory for a fast direct comparison with measured spectra. Based on calculating and comparing the sum of residual squares for spectra within a reasonable range of the previous spectrum, the best fit is chosen within a few ms, providing online capabilities much faster compared to typical 10–30 fps video frame rates of SFA data recording. Look-up tables can be saved, stored and recalled into other real-time software, which offers the possibility to implement this into an SFA feedback regulation.

2.12.3 Conclusions

In summary, new optics and the 4×4 transfer matrix approach by Schubert [21] for acquisition and simulation were implemented and tested, respectively, of full transmission and reflection mode MBI patterns were obtained in a variety of different SFA experiments. A numerical fitting approach for calculation of partial transfer matrices for anisotropic layers was developed and implemented, and an optimized experiment and analysis data flow was developed for SFA experiments in order to reduce systematic errors (see again figure 2.11). The performance of the Schubert method could be demonstrated using a number of benchmark experiments including, the full description of birefringent layers, the consecutive fitting of thicknesses of deposited chemical modification layers, and the measurement of refractive indices of cyclohexane confined within a nanometer gap. Further, the simulation of the rotation angle of two apposing birefringent mica layers were discussed, the fitting of reflection mode spectra, as well as simulation and fitting of metal mirror thicknesses for the minimization of systematic experimental errors in SFA. The analysis procedure introduced here makes SFA an absolute technique, not only with respect to an optical reference thickness, but with respect to the dimensions of the full stacks of material in the interferometer cavity, and enables a more detailed insight into SFA data.

The newly developed optical layout for SFA, which simplifies operation, introduces reference beams, allows recording of reflection and transmission mode spectra, and minimizes potential systematic errors in experiment and analysis. This approach greatly simplifies SFA experimentation and analysis and opens SFA for new and exiting opportunities, including meta-materials, multilayered anisotropic layers, layers of rotating anisotropic layer, as well as chiral layers, for which partial transfer matrices

are readily available from Schubert's original work.

2.13 Further Dissemination

2.13.1 Impact on Further Projects

During the development of *SFA Explorer* up to its present state it has grown in features and enabled several other projects. Some of those are presented here:

X-SFA: A variant of the SFA that enabled simultaneous measurement of X-Ray Reflection (XRR) was used to examine spontaneous structure formation in confined ionic liquids and liquid crystals, and their behavior under mechanical stress. The birefringent nature of those used liquid crystals distorted the FECO patterns to a point where analysis using the classical analysis would introduce a significant amount of artifacts. The use of *SFA Explorer* revealed those distortions and after the introduction of an interferometer model using an anisotropic liquid layer also successfully analyzed the measurements. [69]

In-situ Crevice Corrosion: Corrosion of metal films thin enough to be still examinable in a transmission experiment evidently behaves different than corrosion of a bulk metal. Although the idea of an SFA in reflection geometry was already proposed by Roger Horn, this approach did not reach the necessary degree of maturity to actually perform meaningful experiments. In [70] Merola, *et al.* perfected this method to a point of being able to measure crevice corrosion in-situ and in real time. This was the first project to facilitate the reflection geometry analysis capabilities of *SFA Explorer*.

Lipid Stability: Biological studies on a (sub-) cell length scale tend to be complex, as the space within cells is highly crowded and often localized by enzymes anchored within a membrane. Structures, such as cell membranes, are only a few nanometers thick which makes it hard to account for their individual contribution on the resulting FECO images. While the classical method of analysis lacked both precision and reproducibility, an adapted version of *SFA Explorer* that included additional, individually fittable layers within the interferometer model, was able to successfully analyze those patterns. [71]

Electrochemical Investigations: Electrochemistry in the SFA has a long history. However, those studies suffered from the difficulty of only having one surface available for use as an electrode. Solutions including, for example, rings of wire hovering around the SFA disks always raised the question of how much the sub-optimal geometry of the electric field impacts the results. Adding another metallic layer within the interferometer in order to have two opposing electrodes produced highly irregular FECO patterns. [56] An optimization of

this interferometer design was possible due to simulation of spectra for different design options using the matrix library of *SFA Explorer* and finally measurements could successfully be analyzed. [72]

2.13.2 Showcase

SFA Explorer comes as a Graphical User Interface (GUI) based python program. Main program functions as well as most important parameters are accessible from the main screen (see figure 2.16). Less common options and settings for setting up the interferometric cavity layout can be found in an extra dialog “Options” (see figure 2.17, left). This includes run time optimizations such as only simulating spectra for a fraction of data points in the spectrum (“spectral divider”), or support for cutting the red and blue edges of spectral data in case of pixel data misalignment due to sensor binning or optical distortion due to sensor width. *SFA Explorer* knows two major operation modes: (a) Fitting of selected parameters using a Levenberg-Marquardt (least-squares) algorithm with quasi-infinite resolution, and (b) a lookup table based mode for finding a global best fit within a set of precomputed parameterized spectra. While (a) results in a higher quality of analyzed data and allows more degrees of freedom for fitting, it recomputes spectra for every step which is more expensive in computation time. The time-intensive computation of spectra for (b) can be externalized (see figure 2.17, right) and parallelized. It also allows more flexibility in the design of spectra requiring special treatment such as the spectral convolution over a sloped distribution of distances as explained in figure 3.5 (page 54) and used for figure 3.6 (page 56) at the cost of having to pre-define a grid of possible fit values. A special variant of a lookup table incorporated into the main program allows for also applying an offset to the real part of the refractive index of the liquid medium (see figure 2.15, section 2.11.2). This feature is specially designed to analyze density fluctuations in close confinement.

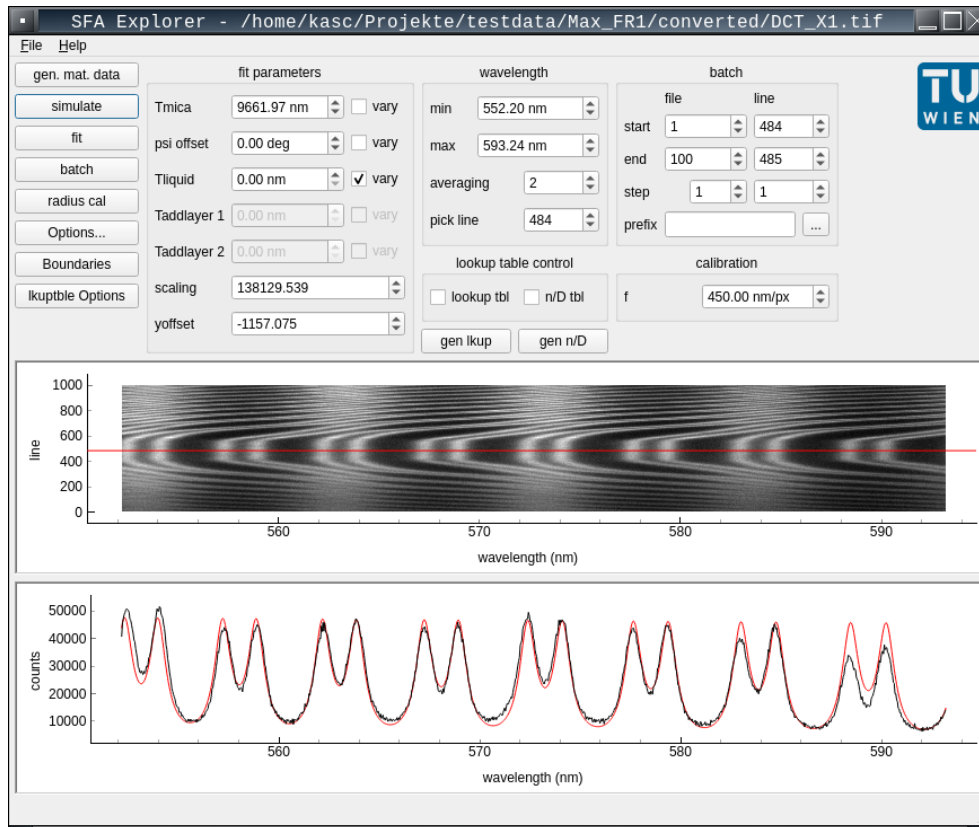


Figure 2.16: Screenshot of the main screen of *SFA Explorer* using a Qt based GUI run on a linux computer. Approximately the top about third allows for setting the most common parameters for analysis operation and allows the user to invoke the main functions or further dialogs for specific parameters. The middle third shows the currently loaded spectrum overlaid with a marker (red line) highlighting the line within the recorded frame selected for analysis. The bottom third shows the intensity graph of the line in the spectrum selected above (black) and the most recent simulated spectrum (red). Note: *scaling* and *yoffset* represent parameters for linear scaling of the simulated spectrum. Since intensities stored in the measured frame depend on many effects and measurement parameters, they cannot be considered representing an absolute scale, so negative *yoffsets* and huge scalings are common.

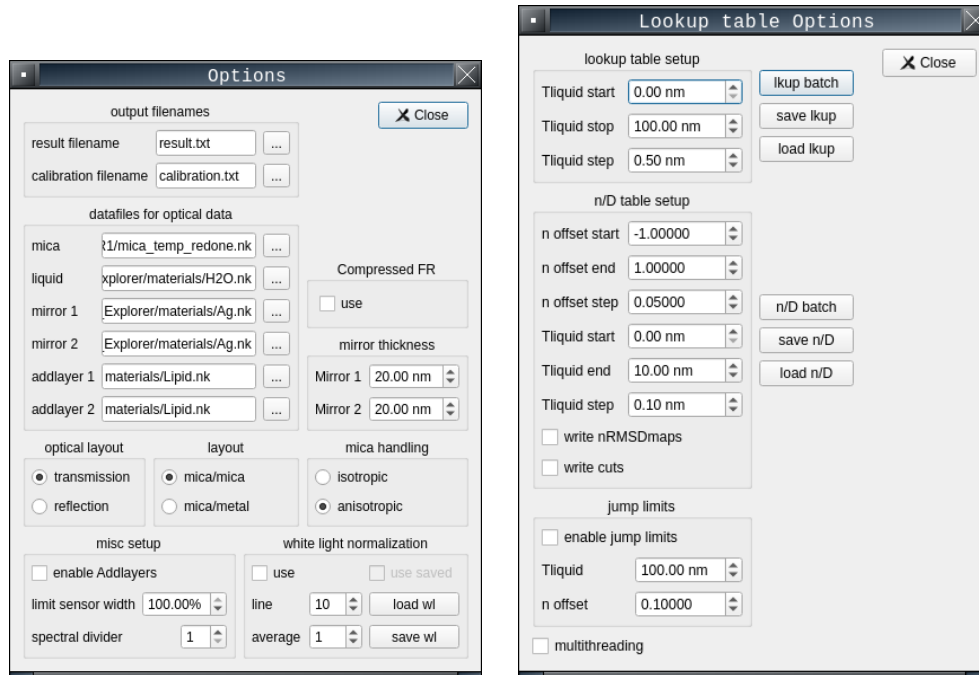


Figure 2.17: Left: Screenshot of the *Options* dialog of *SFA Explorer*. Besides selection of filenames for generated reports and files describing optical properties of materials. The interferometer layout can be parameterized and the white light normalization can be set up. Right: Screenshot of the *Options for lookup table operation* dialog of *SFA Explorer*. This dialog controls generation parameters for one or two dimensional lookup tables (distance or distance and offset to the real part of the refractive index of the fluid layer). Lookup tables can be saved and restored or generated by external programs and imported here.

2.14 Outlook and Roadmap for the Software

Development on the *SFA Explorer* project will continue. Among others, the next milestones include:

- Re-implementation using model/view framework
- Allow and implement more layer types (e.g. helical anisotropic layers, effective media layers, potentially chaining of layers)
- Decoupling the engine for calculation of spectra from the main code and release as open source
- Allow arbitrary stacks of layers
- Easier workflow
- Automatic documentation of the analysis process including representing the stack of layers in machine readable form and potentially enriching the analysis data with machine readable metadata
- Implement a plug-in mechanism for user-supplied analysis.

3 Molecular Forces Apparatus - Proof of Principle

This chapter focuses on the design, construction, and benchmarking of the apparatus implementing an MBI-based technique to enable single molecule direct kinetic experiments, the Molecular Forces Apparatus (MFA).

While the actual target of this device is to stabilize a probe with respect to a sample in five dimensions (three spacial and two rotational), the corresponding journal publication shows only a stabilization in vertical (z) axis. For this purpose the device has been dubbed *Surface Forces Clamp (SFC)*, as the main depicted feature is a “clamping” of the absolute distance of probe and sample. The full 5 axis (3 lateral, 2 rotational) version has been filed as a patent application and for the time being is to be treated confidential.

At the time of printing this present work large parts of this chapter are still in submission with *Review of Scientific Instruments* as “*Design and testing of a drift free scanning probe microscope with absolute distance control*”, manuscript RS121-AR-02700. The materials and methods section can be found in appendix Molecular Forces Apparatus - Proof of Principle starting on page 67.

3.1 Introduction

After almost 35 years of truly successful and transformative advancements the AFM, and SPM in general, still have a fundamental limitation: A constant drift and uncontrolled motion of probe and tested surface structures with respect to each other. This is inherently linked to the currently accepted design principle – only forces are measured, distances are inferred from force measurements and piezo motions.

Current SPM technology does not provide an ultra-stable 3D-reference frame to position an SPM probe with sub-Å resolution. In particular Atomic Force Microscopy (AFM) does not provide a direct, simultaneous yet decoupled measure of forces and absolute position between the probe and a given point of interest (for example, a single molecule) at a surface/interface. In current technology, the relative distance is inferred from the measured (or calibrated) displacement of the piezoelectric translation of the AFM probe or sample stage and the response of the cantilever spring. [73] Hence, an apparent distance is obtained by *a posteriori* interpretation of the ensuing force-vs-displacement characteristics and not through an independent method. Ensuing forces are measured as a function of the displacement of a piezoelectric translator,

which is then converted into an apparent distance. The displacement of the piezo-electric translator is, however not absolute with respect to a sample and is corrupted by uncontrolled mechanical and thermal drift of the whole microscope. This limits the time-scale for controlled measurements at a given distance, during contactless hovering above a surface, to a few seconds (where drift is still insignificant). System drifts cannot be compensated *operando* by direct measurement. This limits AFM to processes that appear on short timescales (seconds). AFM force studies and therewith a large number of applications of AFM in biological and nano-sciences will benefit from a truly distance controlled AFM technology.

In the last few years these fundamental design flaws of AFM have been increasingly realized across interdisciplinary fields. Current concepts resolve this issues at the expense of sensitivity and range. For instance optical-trapping in a back-scattering geometry was used to provide accurate positioning of an AFM probe above a surface in 3D, yet is limited to static measurements of transparent substrates. [74] Likewise, absolute sample separation was measured between an AFM-probe and a solid substrate in (and limited to) the presence of an irreversibly adsorbed film by analyzing a scattered evanescent wave that is generated at the surface of the sample. [75] Simultaneous colloidal-probe AFM and Reflection Interference Contrast Microscopy were successfully used to study the compression mechanics of polymer brushes with a force sensitivity of a typical AFM sensor, yet only with an absolute distance resolution of 2–3 nanometers, at best. [76] Also this technique is limited to macroscopic (optically resolvable) colloidal probe tips.

Complementarily, the SFA has been used for more than 40 years now for the simultaneous, yet decoupled, measurement of surface forces and absolute positioning in z-direction (with Å-accuracy) using MBI. [12, 26, 27, 37, 77] In addition, MBI also provides a direct and dynamic visualization of evolving contact geometries. In contrast to AFM, SFA offers absolute vertical separation measurement and dynamic control with an accuracy of 50 picometers between two opposing interfaces. [77, 78] Yet, with its macroscopic probe dimensions (centimeters) it lacks the lateral resolution of AFM. Also, forces are measured with double cantilever springs with spring constants of typically 500–1000 N/m. Consequently, the force sensitivity is limited to several tens of nN and single molecule interactions and single bond breaking cannot be observed with SFA. Instead, SFA has been widely used to explore multiple hydrogen and hydrophobic binding formations in parallel [28, 29, 35] and various interfacial forces between apposing surfaces, including steric forces and structural forces due to confined fluid interfaces [35, 36, 79] in very close proximity (below 1 nm) and with Å-resolution.

3.2 Concept

In this work the working principle is described of a novel design for an absolute distance based force measuring apparatus, for the name Surface Forces Clamp was

coined. As discussed above, SPM suffers from thermal drift, which can be minimized but not eliminated by hardware design and post-processing software solutions. What is not achieved in state-of-the-art AFM is an absolute distance control between the sample surface and scanning probe. This would in principle allow a real time drift correction, that is, constant positioning of sample and surface in space and time. Here, a method-independent approach to enable constant distance operation of in principle all different SPM methods was chosen, while the focus has been put on showing exemplary applications for AFM and SFA. As shown in figure 3.1, an approach based on laser-based interferometric sensing of the relative position of the probe and the sample surface with respect to each other was chosen. In previous work a different laser-based approach was also developed by the Kurihara group, [80] where an interferometric bouncing from the back of a single surface is utilized to measure the relative placement of an intransparent sample surface. In comparison to this so-called twin-path SFA, an interferometric clamping between upper and lower sample mount was designed and its intrinsic stability and applicability demonstrated for both AFM and SFA measurements.

3.2.1 Design Principle

In detail, the central idea is to measure the position of sample and probe with respect to each other - in terms of an absolute distance - using laser based interferometers as a “distance clamp”. This fixes an external absolute distance Z , which can directly relate to the surface separation D . Figure 3.1 shows a sketch of the essential design features and working modes of the designed devices while figure 3.2 depicts the complete optical path used for this setup.

From the conceptual point of view, the Surface Forces Clamp (SFC) (see figure 3.1) features a generic home-built inverse reflection microscope-like setup with interchangeable sample holder concepts to implement different SPM techniques. A piezo driven xyz-stage with an aperture provides relative motion for a sample with respect to a static probe.

The novel and unique aspect of this apparatus consists of a synergistic combination of MBI measurement of the absolute distance (D) between sample and probe and a fast distance clamping and drift correction using an IR-laser Fabry-Pérot interferometry-based approach. The clamping is accomplished by comparing the laser distance Z (see figure 3.1) to a user-defined setpoint Sp_z , while simultaneously a PID controlled approach corrects the relative position of sample and probe by moving the xyz-stage. Thereby the regulated output position reflects the intended absolute position as well as any necessary compensations due to sample and/or surface drift in the z-direction. These can then be fully compensated in real time with up to kHz reaction time given the currently utilized laser hardware.

Hence, the PID output position (PID_z) position corrects for the intended absolute position of the sample and the probe holder with respect to each other, which includes

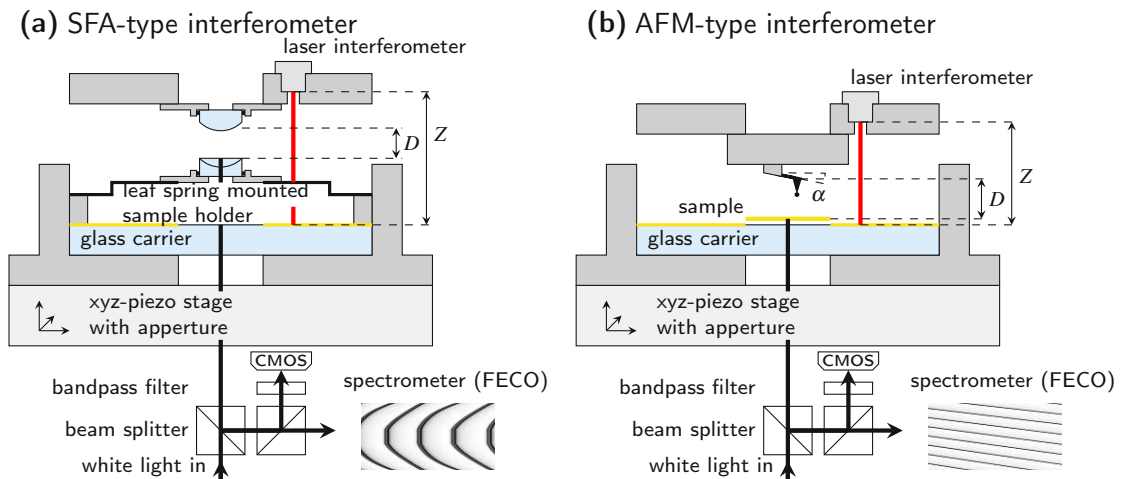


Figure 3.1: Schematic drawing of the apparatus in SFA-mode (a) and in AFM-mode (b). Drift is measured using a Fabry-Pérot interferometer (laser interferometer) against the gold coated glass carrier (Distance Z) and corrected using a PID-controlled xyz-piezo stage. The aperture in the piezo stage allows for measuring white light interferometry distances (Distance D). In case white light interferometry is used, the emerging interference patterns can be analysed as Fringes of Equal Chromatographic Order (FECO) after spectroscopic splitting (simulated patterns expected for both measurement modes depicted as insets) or as Newton rings (for an example see fig. 3.6 (a)) by using a bandpass filter and a CMOS camera. In SFA-mode (a) the interferometer is composed like a classical SFA-type crossed cylindrical quartz disks in mica-mica reflection geometry. For the AFM-mode (b) the interferometer is built using a bottom-side gold coated colloidal probe AFM cantilever against a gold coated microscopy coverslip.

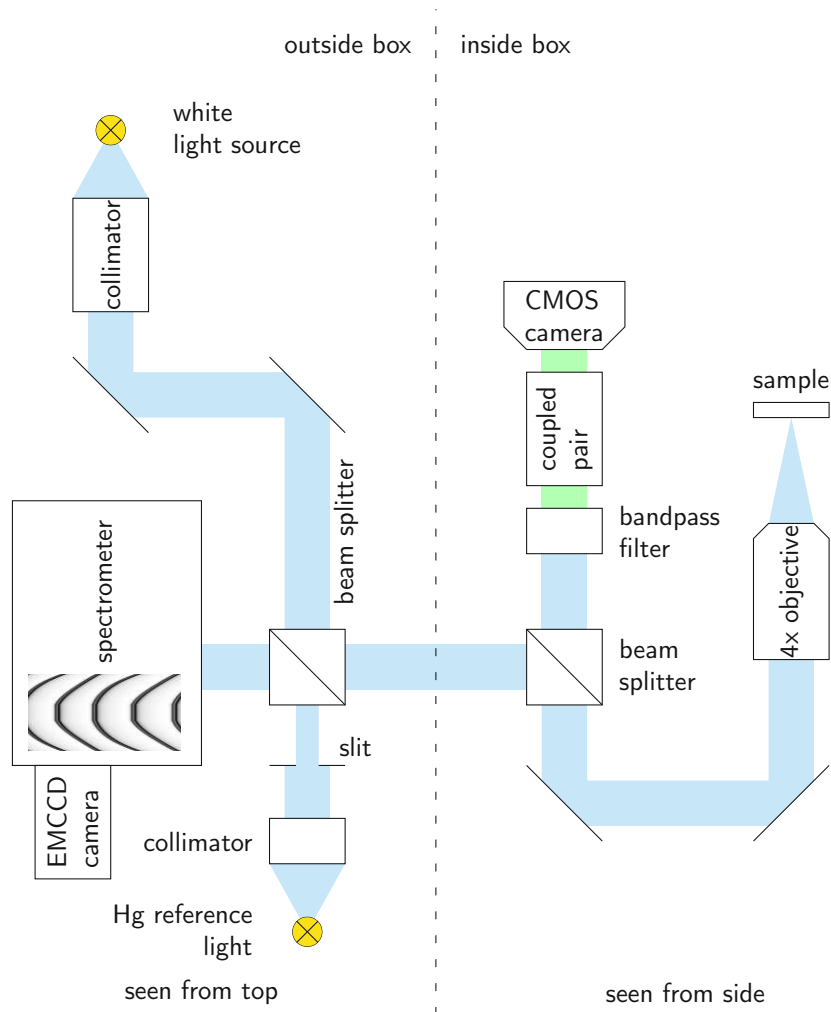


Figure 3.2: Optical white light path (not to scale). The left half depicts the beam path outside the noise cancellation box as seen from a top view. The right half shows the optical path within the box as seen from the side. This setup ensures heat sources (light sources) are outside the box which also dampens climate (temperature and humidity) fluctuations in addition to air-transmitted vibrations.

drift correction as well as machine characteristics. In turn Z characterizes the absolute sample to probe holder distance, which is the process variable of the PID loop. The FECO distance (D) reflects an absolute distance of sample and probe measured by classical SFA in reflection mode geometry, which can also be used for benchmarking the absolute Z positioning quality. Further, the difference between D and PID_z contains information about forces inherent to the used samples (for example surface forces).

Similar to the SFA approach, by a definition of the contact position, that is, when sample and probe touch in a dry atmosphere, it is hence possible to set an absolute sample-to-probe distance using the IR-laser Fabry–Pérot interferometry approach, for both the AFM- and the SFA-like setup.

3.3 Results and Discussion

In this section the newly constructed device will be discussed in terms of benchmark experiments, in both AFM and SFA mode operation.

3.3.1 SFA Measurements and Characterization of Device Behavior

First, figure 3.3 (a) shows a comparison between distance setpoint (Sp_z) and PID_z positions, recorded during continuous open-loop (piezo not linearized by the closed-loop strain-gauge extension sensors) approach/separation. The recorded data shows the expected sigmoidal deviation from an idealized linear response of the piezo for $Sp_z = PID_z$. Approach curves (\bullet) exhibit a slightly different dependence as compared to separations (\blacktriangle) indicating a typical hysteresis. This is the inherent piezo characteristic, as expected for an open loop operation.

In our approach the PID sensor directly corrects the piezo characteristic by utilizing the absolute distance derived from the Fabry-Pérot interferometer. In this sense, the interferometric distance acts as a sensor for linearizing the piezo characteristics during operation; that is, effectively setting up a closed-loop control with the laser based distance sensor.

This closed-loop operation principle can now be directly benchmarked using an SFA-based force versus distance experiment. Therefore, a force measurement was performed between two mica surfaces (in crossed-cylinder geometry) in HNO_3 at a pH of 3.0.

Figure 3.3 (b) shows the linearized (corrected) PID_z position versus the distance D measured by the SFA approach. The data indicated a clear linear relation between D and PID_z . The white light interferometry measured distance D reflects the PID set position PID_z linearly with three exceptions which are: When 1) sample and probe touch in hard contact ($D = 0$, \ddagger), 2) at a distance of about 30–40 nm before close contact (long-distance forces), and 3) during separation where an adhesive jump out

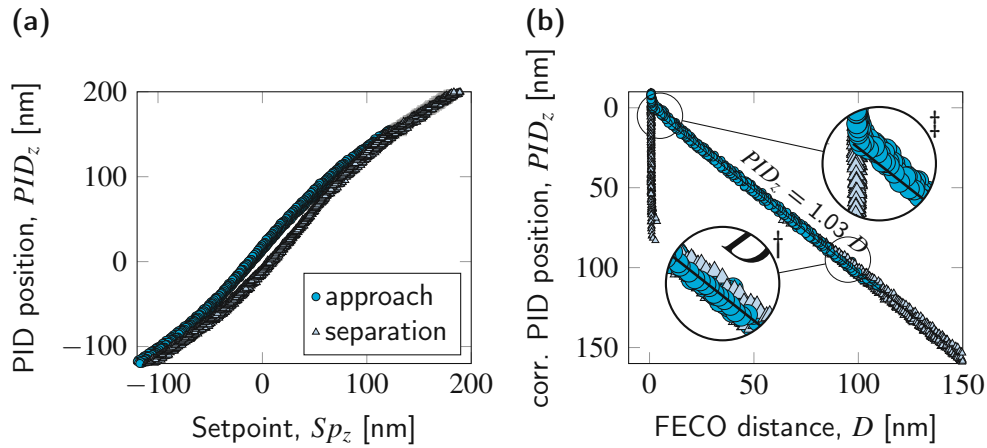


Figure 3.3: In order to match the laser interferometric distance (Z) to a given distance setpoint (Sp_z), the stage is moved to a position determined by the PID controller (PID_z). **(a)**: PID_z plotted against Sp_z shows a sigmoidal dependency and hysteresis (only one occurrence shown) originating from characteristics of a stack of piezo crystals used to drive the xyz-stage. **(b)**: After correction for drift over time (offset shifted to match the other forceruns) PID_z in comparison with the FECO distance (D) shows further relaxations of the system at high distances (\dagger) in addition to the expected deviations near contact (\ddagger) caused by surface interaction forces. As a result the overall slope is 1.03.

of contact (jump out) occurs due to the adhesive hysteresis (\dagger).

This data can be further directly transformed into a force versus distance characteristic by subtracting the linear approach rate from the data shown in figure 3.3 (b). As customary in SFA, forces have been calculated assuming this linear approach rate between PID_z and D values, using the spring constant of the sample holder (8860 N/m in this case).

Figure 3.4 shows the resulting force versus distance characteristic. The force characteristics during approach and separation indicate a stable zero-force line for large separation distances up to 120 nm, as well as the expected hard wall at very close separation distances of about 0.73 \AA . The data indicate a typical approach curve expected for two mica surfaces immersed in water at mildly acidic pH levels of 3.0, with an ionic strength of 1 mM.

The data can be fitted well using the DLVO theory (----) with literature and theoretical values [81] for the Hamaker constant ($2.2 \times 10^{-20} \text{ J}$) and the Debye length ($9.61 \times 10^{-9} \text{ m}$). The fitted interaction constant of $16.71 \times 10^{-12} \text{ J/m}$, which corresponds to a surface potential of 47 mV, in perfect agreement with expectations for mica versus mica, where the surface is already partially protonated, close to the point of zero charge between $\text{pH} = 2\text{--}2.5$.

For further characterizing drift compensation characteristics a "set-and-hold" experiment, at given distances D , was performed. Therefore, a constant distance ramp with decreasing separation was programmed, and at each step the distance was stabilized by the Fabry-Pérot interferometry (constant distance clamping), and D were

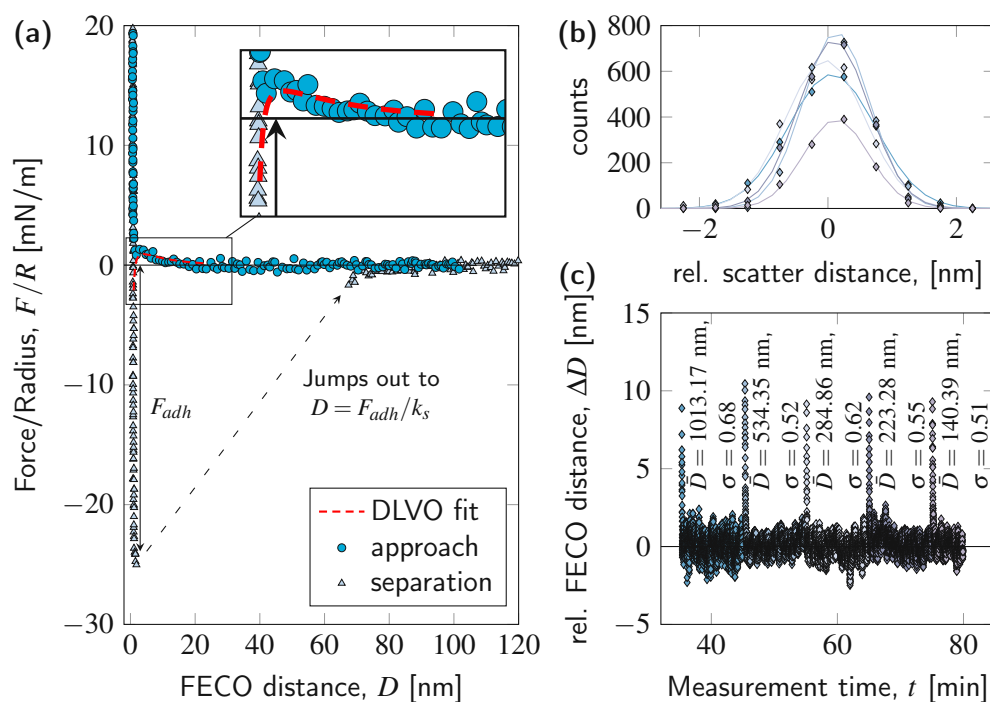


Figure 3.4: (a): Force versus distance characteristic recorded during approach and separation of two mica surfaces in HNO₃ at pH = 3. (b): Histogram of stabilised distance over 10 minutes (last distance over 5 minutes) (points) and corresponding Gaussian fits (lines). (c): Recorded relative distance changes (ΔD) during stabilisation of given distances over 10 minutes each (last distance over 5 minutes), respectively (see also: text for details). For better visibility of the noise level, the average set distance of each step (denoted as \bar{D}) has been subtracted from the position data of that step. The apparent spikes indicate the motion during a jump between two set distances. The equilibration times depend on the jump distance and feedback settings and are in the range of a few seconds. Color codes of each step corresponds to those in (b).

recorded for ten minutes. This allows us to track and benchmark the absolute distance clamping capacity of the constructed device.

Figure 3.4 (c) shows the deviation (ΔD) of the measured D from their distance average (\bar{D}) as a function of time for each approach step. It can be seen that the system stabilizes the absolute distance between the two surfaces well within 1 nm over an extended time of up to 10 minutes. In principle this can be extended to any desired extended time period (in practice as long as an experimental system will be stable).

Since the focus of this benchmark experiment is the long-time stability the first 100 data points (20 seconds) of each step, during stabilization of D after the jump to the next set distance, were not taken into account for calculating averages as well as histograms (b)).

This yields a Gaussian distributed absolute distance over this extended time period. Gaussian fits of the distance histograms are depicted in figure 3.4 (b) with the standard deviation of each step shown in subfigure (c) (σ). This data demonstrates that the D can be successfully stabilized to within 0.5–0.6 Å over 10 minutes. Virtually no significant drift occurred in this closed-loop system, which is stabilized by the implemented Fabry-Pérot distance clamping mechanism.

These results confirm and support that the laser-based interferometric-distance clamping can be directly utilized as an absolute distance clamp. Precisely, the absolute position distance clamping was confirmed by MBI. Application of this setup can include, for instance, measurements between non-transparent samples, complex multilayered samples or samples with gradients of refractive indices, where the absolute character of the MBI approach becomes limited by the modeling of the sample, or any other type of SPM methods. Here, the focus should be put on demonstrating that this mechanism can be utilized to also record *absolute* force versus distance characteristics in an AFM geometry.

3.3.2 MBI AFM Theory and Measurements

As shown in figure 3.1 (b), a second sample holder for mounting a standard commercial AFM cantilever chip was constructed with a colloidal probe of a given radius of 5.5–9 μm, effectively forming an interferometric cavity of (gold | solution | gold).

It is our aim to probe the piezo feedback regulation with the Fabry-Pérot laser interferometer also for AFM, while simultaneously evaluating the quality of the distance read out with MBI directly from an interferometer constructed between cantilever and surface. This requires a reflection mode operation of the MBI, here with a gold cantilever (with a reflective 50 nm gold coating on the sample side) and a surface with a semi-transparent gold coating (15 nm).

For this first set of experiments a colloidal probe system was chosen due to geometric restriction of commercial cantilevers with fine needle tips. Specifically, commercially available AFM cantilevers are optimized for a mounting angle of 10° in order

to allow for easy mounting as well as detection using the beam bouncing method. In addition the tip height is usually about 15 μm , which sets a too large distance for highly resolved MBI. Due to its spherical geometry, and selectable size, a colloidal probe tip *per se* does not require any special angle mounting and provides a selected separation distance based on the colloidal radius. In principle, it is possible to perform the following experiments with needle tips as well.

Considering these cantilever limitations, MBI is further preferably performed with interacting surfaces normal to the propagation direction of the light used in detection. In practice, it is possible to go to a shallow angle of about 2–3 degrees, without the risk of touching the sample with the cantilever chip instead of the tip. This angle will however also influence the distance resolution with MBI as follows.

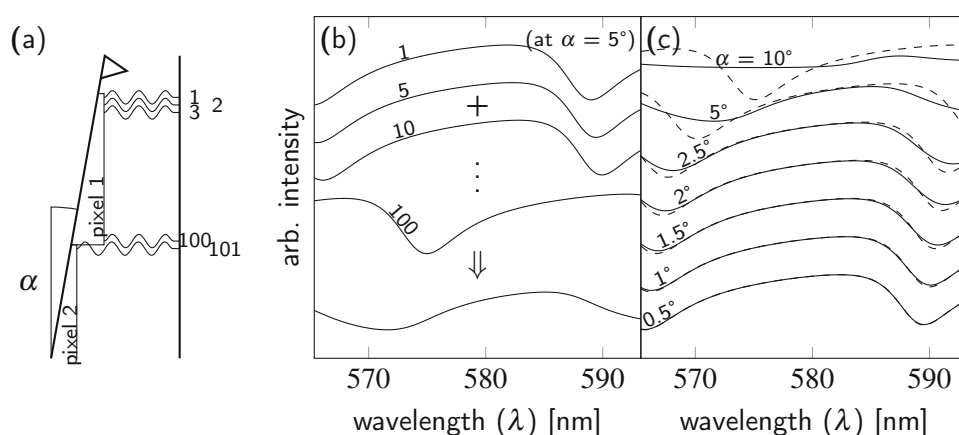


Figure 3.5: Theoretical evaluation of the influence of the cantilever mounting angle (α) on white light interferometric spectra. **(a)**: Interference patterns of different distances (denoted by a number eg. 1–101) between cantilever and surface will occur on the same pixel on the detector camera. **(b)**: The resulting superposition of those patterns (1–100) can cause peak broadening and loss of contrast, to an extent line-based analysis is no longer usable. **(c)**: Comparison of resolution-limited spectra at certain mounting angles α (solid lines) compared to the midpoint distance of the same distance interval (dashed lines). (Simulations have been done for 100 distance steps per line in a spectrum at a lateral dispersion of 1107.595 nm/px).

Figure 3.5 **(a)** depicts the influence of the angle of the cantilever (α) on the expected spectral patterns of the signal in MBI, based on a simulation for a 5 degree tilt of the cantilever.

First, and as expected the propagating light waves of the incident light form a continuous distribution of interference patterns for each distance, as indicated in the figure 3.5 **(b)**. However, the resolution on the detector is limited by the optical path, dispersion of the spectrometer, and the pixel size of the camera chip. Hence, with increasing tilt angle an increasingly larger range of distances is smeared out onto one single pixel of the detector. As indicated in the figure panel **(b)** this results in an integral spectrum on each pixel.

These smeared interference patterns strongly depend on the distance distribution

seen by each single camera pixel, and a lower angle will considerably increase the resolution.

In detail, figure 3.5 (b) shows the simulation of a selection of those overlapping interference patterns emerging from 100 even-spaced distances convoluting on a single pixel given a mounting angle of 5° and the set total dispersion of our device, as well as the resulting overlap spectrum at the bottom of the graph.

Figure 3.5 (c) shows the comparison of overlap spectra (solid lines) to the respective single spectrum at median distance (dashed lines) for different mounting angles. The simulation shows not only a broadening of the destructive interference patterns (minima), but also a significant shift of the spectral position of the minima for higher angles. In any case, it is possible to simulate such pattern for any given tilt angle, providing a possibility to track FECO directly from an AFM cantilever.

Consequently, from an experimental point of view it is ideal to lower the mounting angle as much as possible, given the currently available commercial cantilever chip design. Hence, actual experiments have subsequently been performed using a mounting angle of about 2.5° .

Figure 3.6 shows results of a force versus distance experiment also recorded in HNO_3 at a pH of 3. Several interesting aspects of this experiment can be summarized as follows.

First, panel (a) shows a series of patterns recorded during approach, and increased compression in hard contact at $D = 0$. Indeed, reflection mode detection provides an expected Newton pattern for a cantilever beam in the top view camera (green notch filter with ± 2 nm around 532 nm). At large separation (left) the pattern indicates lines of alternating increased and decreased intensity, with shorter separations at higher distances. In hard contact the pattern offers a direct view into the deformation of the cantilever beam. As can be seen, the top of the tip (contact point) remains at a stable distance, while the center of the beam starts to bend considerably, as expected for a spring. Hence, Newton ring analysis provides a direct view of cantilever deformations *in-situ*, to an extent that cannot be derived from the classical beam bouncing methods. This will be particularly useful for applications in tribology, where real-time deformation profiles of the tip are crucial for understanding sample/probe interactions.

Second, panel (b) shows a time series of FECO patterns, the simulated patterns for deriving the distance, as well as the PID signal (linear piezo approach) recorded/analyzed for an approach run at a typical AFM approach rate of 100 nm/s. Importantly, it is possible to capture FECO, directly from an approaching AFM cantilever. It has to be emphasized that the approach is controlled in feedback with the Fabry-Pérot distance clamping. As such the comparison of the FECO pattern, the simulated pattern and the PID pattern indicate a well regulated system also in this case. This data uniquely confirms that it is possible to utilize MBI even for an AFM geometry, which immediately makes AFM an absolute distance controllable technology, similar to SFA. Excitingly, it is now possible to translate the measured FECO distances into

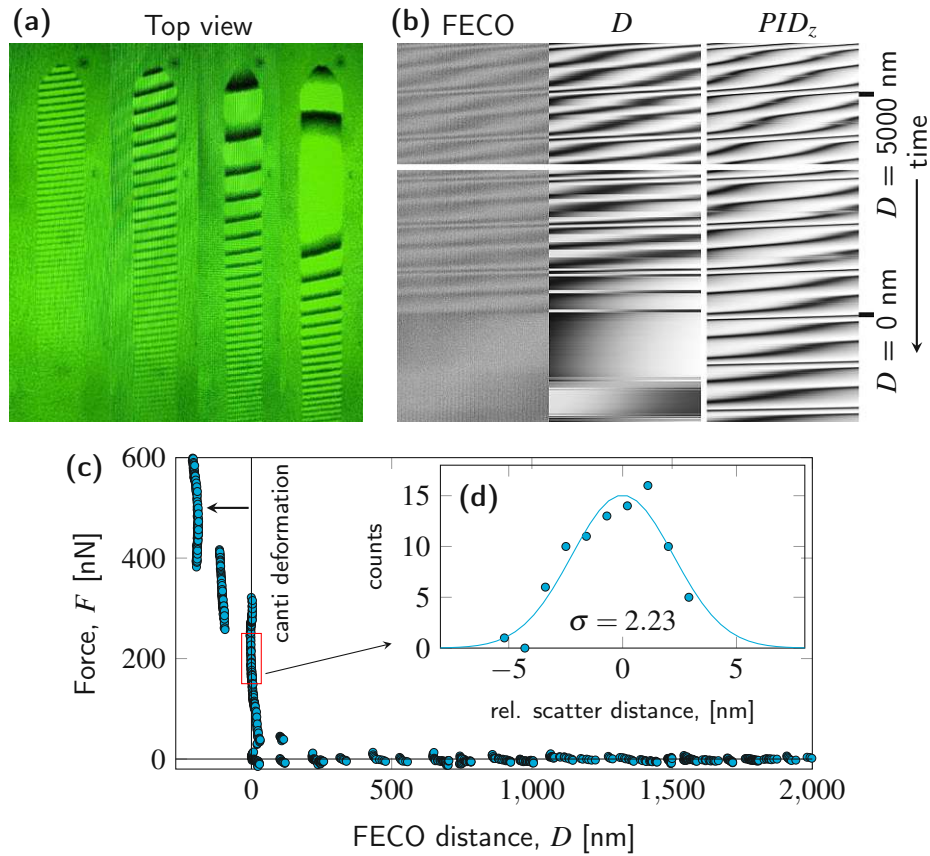


Figure 3.6: **(a)**: Newton ring pattern on the AFM cantilever as seen through the top view path, using a band pass filter, at different distances between cantilever and sample during compression. The third image is near contact, the fourth compressing hard enough to bend the cantilever and force a “belly”. **(b)**: Spectra as seen in a time series during approach (from top to bottom, each line is one frame). Left (FECO) the measured spectra after background subtraction, middle and right a simulation of spectra from the fitted distances (D) and the stage positions (PID_z). **(c)**: Force/Distance curve for this approach. Inset **(d)**: Histogram of the fitted distances during contact before deformation starts (red box) and Gaussian fit over the histogram.

a force versus distance characteristic similar to SFA.

Panel (c) shows the derived force versus distance characteristic. While rather noisy, the data demonstrates a clear and absolute distance regulated approach from 2000 μm distance. As expected, the sample touches the surface and runs into a hard wall at $D = 0$. No standard correction for the cantilever bending [73] had to be applied to derive a true distance versus force pattern for an AFM force probe experiment. The zero distance can be defined similar to an SFA approach based on a (dry) reference measurement. Once a proper zero distance is defined any distance can be referred to this reference in terms of an absolute distance. As such, this provides an absolute force versus distance, and the possibility to set any distance in future experiments using FECO and/or the Fabry-Pérot distance clamp. In hard contact, when the sample/tip separation does not change significantly, the resolution of the MBI can be read out from a Gaussian distribution of the measured distance. As can be seen in the inset (d), an absolute distance resolution of about $\pm 2\text{--}3$ nm could currently be achieved. This is about a factor of 2–3 better compared to an absolute distance sensing using reflection interference microscopy on a colloidal probe. [76, 82, 83] Further, from the zero force line it is possible to read out a force resolution, which is about $\pm 5\text{--}10$ nN with the applied system settings. As a side note, and as can also be seen, during highest compressions, apparent distance jumps could be seen in hard contact. We attribute these to sliding and resulting deformation changes of the cantilever, or possibly even indentation events. A further analysis of such events is out of the scope of this work, but will be considered in future work with the system.

3.3.3 Complementary Discussion of Force Probe Techniques and the SFC Principle

In summary, two important aspects were demonstrated, with implication for force probe experiments.

First, a Fabry-Pérot absolute distance clamping is capable to stabilize an SPM and SFA device. Further the absolute Fabry-Pérot distance can be utilized as a feedback regulation parameter for SFA as well as AFM experiments. This provides an indirect distance clamping, which perfectly correlates with the absolute distance measurement by MBI demonstrated in by direct comparison to the SFA approach. As such, the distance clamp is an ideal and fast method for stabilizing the probe to sample relation, irrespective of the application. Here, AFM and SFA applications were demonstrated, but in principle any relation of a probe to a sample can be fixed by this approach. In the field of SPM this will allow now to conduct distance stabilized force probe experiments. This will allow to collect information on, for example, molecular fluctuations occurring at the single molecular level.

Therefore, and this is the second point, a further increase of the accuracy of the AFM approach is necessary in future work. While it is possible to use the Fabry-Pérot clamping alone, it will be ideal to also enable simultaneous MBI at sub-nm

resolution as an internal reference. In this work the principle could be proven and the possibility show that one can generate and analyze FECO data from direct cantilever bouncing. However, the force read out is limited to 5–10 nN, and the distance to $\pm 2\text{--}3$ nm. These two values are directly correlated. An increased distance resolution will provide better force resolution. If it is possible to reach SFA accuracy of ± 0.1 nm the best expected force resolution will be around 10–30 pN. This will reach the necessary limits of single molecule detection, and will be demonstrated in a future work. However, it will be better to combine the distance clamping with a traditional beam bouncing read out. In particular, FECO read out (at up to 100 fps) is also considerably slower compared to beam bouncing in the kHz sampling range.

3.4 Conclusion

In this work a novel absolute position control for scanning probe devices has been developed. The device utilizes a feedback regulated laser interferometer for stabilizing the absolute distance between probe and sample surface. We demonstrated the capabilities of this interferometrically stabilized scanning probe device using benchmark experiments and comparison to AFM and SFA operation modes. In detail, it could be demonstrated that

- the absolute positioning is accurate to within 0.6 ± 0.2 nm RMS deviation of the distance between sample and probe, irrespective of the operation mode (AFM/SFA).
- absolute position can be held with the same accuracy over extended time scales (tested up to 10 minutes).
- data output from the SFA operation mode is directly comparable to traditional SFA. However, in comparison to fastest acquisition rates of traditional SFA (max. 50–100 Hz) this setup now allows a feedback-regulated absolute distance control with up to several kHz (comparable to AFM).
- in principle the device allows for SFA-like experiments with non-transparent surfaces and complex surfaces.
- direct white light interferometry in reflection mode is possible with AFM cantilevers. Signals are weak, yet well detectable and analyzable. The absolute distance accuracy with FECO analysis, is currently limited to about ± 3 nm, with potential for further improvement based on increased signal to noise ratios.
- Newton patterns provide a direct visualization of the AFM cantilever bending, providing a 3D real-time view of torsion during the experiment.

In summary, with this new setup it is possible to perform distance controlled experiments for both AFM and SFA setups and over extended time scales (>10 min). This will enable for example equilibrium force probing with AFM, probing of fluctuating two-state systems, as well as constant distance and force probing of electrochemical modulations in confinement with the SFA. In addition, it is possible to extend the concept to 3D to enable constant distance positioning with single molecular accuracy in all three spatial dimensions. In AFM mode, imaging the cantilever bending in-situ may provide important insight into nano-friction experiments, local compressibility of thin films and solid electrolyte interfaces, and with new cantilever designs higher accuracy may become possible. Hence, the developed new technology will prove useful for scanning probe microscopies in general, and it will allow new measurement modes, which are to date not possible. The described advances can possibly be retrofit to some existing system designs.

4 Summary and Impact

4.1 Aims

In this work I established a novel analysis methodology (chapter 2) for MBI in reflection geometry that allows for analysis of absolute distances between a semi-transparent sample and an AFM cantilever (chapter 3).

Several improvements to the SFA technique were established (section 2.10), ranging from improved mechanical stability to adapting features considered mature from other optical techniques such as proper reference light intensity spectra.

With the analysis method for MBI in reflection geometry established, I developed a device (chapter 3) to further stabilize absolute positioning of probe and sample. Due to this, static single molecule bond breaking experiments are now possible. The developed approach is a method agnostic way that allows not only for single molecule direct kinetic measurements but is also retrofittable to all kinds of scanning probe techniques and optical techniques including, for example, Surface Plasmon Resonance (SPR), Magneto-optical Kerr Effect (MOKE), or distance stabilized ellipsometry. The design in AFM mode is even capable of enhancing the AFM method to include sensing and tracking of changes in the cantilever, such as torsions or deformations, using MBI without the introduction of an energy rich radiation source that could alter the temperature of the sample or induce corrosion of cantilever coatings. The principle of such a device to stabilize the lateral and absolute vertical positions, as well as two rotational positions in real-time has been submitted as a patent application.

4.2 Impact on Other Work

The analytical method presented in this work is the work horse for SFA analysis in our group. The software itself and the simulation library have been used in many projects for both testing of the feasibility of experimental design by simulation and prediction of parameters necessary to achieve within the measurement, as well as the SFA spectra analysis itself.

The capabilities of this method has enabled SFA based methods to expand to a variety of topics and fields ranging from life sciences [84, 85] via rheology, corrosion, and catalysis to geology with a few of them highlighted in section 2.13.1, such as in-detail analysis of optical properties of liquids such as fluctuations in refractive index [10], or orientation of birefringent substances including membrane creating lipids

4 Summary and Impact

[71], liquid crystals [69], and ionic liquids [86]. Novel layouts of interferometric cavities became analyzable such as SFA in reflection geometry to investigate corrosion processes on bulk metal samples (in-situ crevice corrosion) [39, 70] or the addition of further metallic layers within the cavity to enable electrochemical investigations of liquids between two electrodes [72, 87].

4.3 Outlook

With the foundational work of the development of the MFA done and the proof of principle successfully finished, the next steps include performing the actual single molecule direct kinetic measurements and evaluating the results against reference methods. At the same time a redesign of the device itself and the controlling software in order to reach a ready-to-market state, followed by introduction to market using the foundation of a spin-off company, is projected.

The analysis software *SFA Explorer*, developed in chapter 2, is already being commercially marketed and is currently used by six international laboratories in the USA, Asia, and Europe. Another redesign to enable arbitrary stratified media is planned for the near future. This redesign will be accompanied by a modularization of the library performing spectral calculations alongside a re-licensing of the library as open source.

Appendix

Methods and Materials

Implementation of 4×4 Matrix Method for Multiple Beam White Light Interferometry

Chemicals and Materials

Highest available purity chemicals (NaCl, cyclo-hexane, ethanol, hexane, hexadecane-1-thiol) were used as received from Sigma Aldrich, unless otherwise specified. Milli-Q water (Millipore, resistivity of $\geq 18 \text{ M}\Omega\text{cm}^{-1}$, TOC below 2 ppb) was used for preparing NaCl solutions (pH = 5.5–5.7 and concentration 10 mM). 1,2-dipalmitoyl-sn-glycero-3-phosphocholine (DPPC), was obtained from Avanti Lipids and was stored at -20°C . Mica was obtained from SJ Trading Company (NJ, USA) as approximately $20 \times 10 \text{ cm}$ reddish colored sheets with 2–3 mm thickness.

Surface Forces Apparatus

SFA normal force measurements were performed at 24°C using the SFA 2000 (SurForce LLC, Santa Barbara, CA). The optical setup consists of several beam splitters, optical rail systems, irises, $4\times$ and $10\times$ microscope objectives (Nikon), an LED cold white light source, a low-pass filter to filter any wavelength above 650 nm, and an Andor EM-CCD sensor (338 iXon) and spectrometer (300 mm focal distance, 900 lines/mm grating with blaze angle of 550 nm).

Mica sheets were hand-cleaved to provide sheets with an area of several (typically 5–10) cm^2 and uniform thicknesses ranging from 4 to 6 μm . The edges of these sheets were melt-cut with a hot platinum wire. Particular care was taken to avoid contamination of the mica sheets with platinum particles. With the use of PVD (model see below), the mica sheets were back-silvered with a $40 \pm 2 \text{ nm}$ silver layer and then glued to cylindrical silica disks with a nominal radius of curvature $R = 1\text{--}2 \text{ cm}$, using an UV curable glue (Norland Adhesives, NOA81).

Self Assembled Monolayer and Langmuir-Blodgett Deposition

Atomically smooth gold films were prepared by template stripping as previously described. [35] Freshly stripped gold surfaces were placed immediately into a 1 mM solution of hexadecane-1-thiol, resulting in a hydrophobic surface termination. Exposure of the solution to light was avoided during the reaction time. After 12–24 h,

the surfaces were taken out of the solution, washed with hexane and ethanol, and mounted into the SFA.

Langmuir-Blodgett layers of DPPC were transferred in their gel-phase at 40 mN/m using a R&K LB-trough (Riegler & Kirstein, Potsdam, Germany).

Other Techniques and Instrumentation

An Abbe5 Refractometer (VWR International) was used to measure the refractive index of fluids with 0.5×10^{-4} accuracy.

An in-house designed PVD, manufactured by BestTec (Berlin, Germany) was used for depositing metal layers. The base pressure of the chamber is 1×10^{-8} mbar, and during deposition samples are rotated at 30 rpm, with a distance of 50 cm from a 10 kW electron beam source. This results in a film uniformity of $\Delta\Lambda_1 \leq 5\%$ over 1 cm.

Simulation and Fitting Approach

For the transfer matrix approach described below a home-made graphical user interface (*SFA Explorer*) was used.

Simulated spectra are fit against measured spectra by minimizing the root mean squared deviation using a Levenberg-Marquardt algorithm implemented in the Python lmfit-library. [88] Since measured spectra are usually in counts, instead of transmittance as simulated, the intensity is scaled to pseudo-transmittance using a linear model and thus add a scaling and an offset parameter.

Python Packages and Hardware

The analyses were made using a home-written software (*SFA Explorer*) that was used within a WinPython-3.4.4.6 [89] python distribution with added PySide-1.2.4 [90] (via pypi.org). The modules numpy-1.11.3+mkl [52], scipy-0.18.1 [91], pillow-4.0.0 [92], pyqtgraph-0.10.0 [93], and lmfit-0.9.5 [88] were already supplied by the WinPython distribution. Analysis and benchmarks were performed on a standard office PC with Microsoft Windows 10™, an Intel i7™ processor and 16 GB RAM, with a 7000 rpm HDD.

Optical Data

The optical data used for the simulations for silver [94], gold [94], cyclohexane [95], water [96], DPPC [66], and air [97] were taken from refractiveindex.info, [98] converted to wavenumbers, and reformatted. Refractive indices for mica were fitted using the empirical equation from [61] as a reference for the wavelength dependence, and varying the absolute value and the splitting between the crystallographic distinct refractive indices β and γ , which are perpendicular to the crystallographic c-direction.

Molecular Forces Apparatus - Proof of Principle

Chemicals and Materials

HNO₃ p.A. was purchased from VWR, and was diluted to the experimental pH values using Milli-Q water. Gold surfaces were prepared by thermal evaporation in a home-built physical vapor deposition system at a base pressure of 2×10^{-6} mbar. Samples for SFA experiments consisted of freshly cleaved ruby muscovite mica obtained from S&J Trading (NY, USA). The protocol for SFA surface preparations has been described in detail in previous work. [99] Briefly, sheets of uniformly thick single terraces were cleaved by hand. Afterwards they were PVD back-side coated with 25 nm of silver (sample sheet) and 40 nm of silver (probe sheet) for effective reflection mode operation. [10] The thus way prepared back-silvered mica sheets were epoxy glued onto fused quartz disks with cylindrical curvature in a way the crystal lattice orientation of sample and probe side were retained in a crossed cylinder orientation of the disks.

Force Probing Equipment and Consumables

The Surface Forces Clamp - SFC We built the SFC inside a home-built noise cancellation box on a passively isolated optical table (B9090ACH, ThorLabs) to reduce the effect of environment vibrations as well as temperature fluctuations. The bulk of the device has been constructed from Invar™ and stainless steel. Motions are provided by a MadCityLabs Inc. T-115 piezo driven microscopy stage with aperture. For external distance sensing an FPS3010 displacement laser interferometer was used using D4/F14 sensor heads (attocube, Germany).

Atomic Force Microscopy A Cypher AFM (Asylum Research, Santa Barbara, CA) was used for calibrating the spring constant of cantilevers using the implemented thermal noise methods. Colloidal probe cantilevers were used (CP-CONT-Au-C, obtained from NanoAndMore, Germany) with spherical gold colloids of 5.5–9 μm diameter. The colloids act as a spacer between the reflecting mirrors for Multiple Beam White Light Interferometry. For enhancing interferometry intensities the cantilevers were Ti/Au coated (5 nm/50 nm) at the colloidal side.

Optical Path

The internal distance sensing white light path for reflection geometry has been constructed from ThorLabs parts similar to a previous setup. [10] An Oxford Instruments Kymera KY193i spectrometer (grating: 1200 lines/mm) with an Andor iXon EMCCD camera was used for white light interferometry. The topview path features a green bandpass filter (532 nm ±2 nm, FL532-10, Thorlabs) and a CMOS camera (DCC1645C, Thorlabs).

Software

For alignment, experiment control and logging home-made programs written in LabView using supplied libraries from MadCityLabs and attocube were used. The PID functionality uses “PID Advanced Autotuning” function from the National Instruments LabView 2017 Autopid library. Analysis of white light interferometry spectra has been conducted using SFA Explorer 3.5.2. [10] Scripts for simulation of spectra used the SFA Explorer internal multiple matrix method library.

Experimental procedures

Experiments for keeping constant positions at different distances (used for figure 3.4 **(b)** and **(c)**) were conducted in air. Dynamic SFA experiments (used for figure 3.3 and 3.4 **(a)**) were performed in 1 mM solution of nitric acid.

As surfaces round microscopy cover slips coated with 5 nm Ti and 15 nm of gold were used (serving as interferometer surface as well). “AFM-like” experiments (used for figure 3.6) were performed in 1 mM solution of nitric acid.

All measurements have been conducted over night under remote control of the machine to reduce vibrations and temperature fluctuations.

The entrance slit of the spectrometer had an opening of 20 micrometers. The camera sensor was set to a 2×2 binning. For the static SFA experiment the EM-CCD camera was set to an exposure time of 0.2 seconds resulting in a cycle time of 0.21301 seconds. All other measurements have been set to an exposure time of 0.19806 seconds to maintain a cycle time of 0.2 seconds. Spectra were recorded as 16 bit grayscale TIFF. The wavelength window has been controlled on a per-line basis using a mercury vapor reference lamp. The PID controller has been parameterized with a constant term of 0.25, an integration time of 0.01 minutes, and no derivative term. The total spring constant on the SFA sample holder was measured to be 8860 N/m. The spring constant of the AFM cantilever was measured to be 243 pN/nm.

List of Publications

Publications as First Author

- **Schwenzfeier, K. A.**, Erbe, A., Bilotto, P., Lengauer, M., Merola, C., Cheng, H.-W., Mears, L. L. E., & Valtiner, M. (2019). Optimizing multiple beam interferometry in the surface forces apparatus: Novel optics, reflection mode modeling, metal layer thicknesses, birefringence, and rotation of anisotropic layers. *Review of Scientific Instruments*, 90(4), 043908.
- **Schwenzfeier, K. A.**, and Valtiner, M. (2022). Design and testing of a drift free scanning probe microscope with absolute distance control. *Review of Scientific Instruments*, in submission.

Submitted Patents

- Technische Universität Wien, im Namen von **Schwenzfeier, K. A.** and Valtiner, M. (2021). *Verfahren und Vorrichtung zur Störgrößenkompensation bei der Positionierung eines Probenträgers* (AT Application No. A 50458/2021, in registration). Österreichisches Patentamt.

Publications as Co-Author

- Merola, C., Cheng, H.-W., **Schwenzfeier, K. A.**, Kristiansen, K., Chen, Y.-J., Dobbs, H. A., Israelachvili, J. N., & Valtiner, M. (2017). In situ nano- to microscopic imaging and growth mechanism of electrochemical dissolution (e.g., corrosion) of a confined metal surface. *Proceedings of the National Academy of Sciences of the United States of America*, 114(36), 9541–9546. (contribution: development of analysis software and strategy)
- Wieser, V., Bilotto, P., Ramach, U., Yuan, H., **Schwenzfeier, K. A.**, Cheng, H.-W., & Valtiner, M. (2021). Novel in situ sensing surface forces apparatus for measuring gold versus gold, hydrophobic, and biophysical interactions. *Journal of Vacuum Science and Technology A: Vacuum, Surfaces and Films*, 39(2), 023201. (contribution: simulations to determine feasibility of the project, development of analysis and simulation software)

Frontpages

Review of
Scientific Instruments

ARTICLE

scitation.org/journal/rsi

Optimizing multiple beam interferometry in the surface forces apparatus: Novel optics, reflection mode modeling, metal layer thicknesses, birefringence, and rotation of anisotropic layers

Cite as: Rev. Sci. Instrum. 90, 043908 (2019); doi: 10.1063/1.5085210
 Submitted: 10 December 2018 • Accepted: 25 March 2019 •
 Published Online: 19 April 2019



Kai A. Schwenzfeier,^{1,a)}  Andreas Erbe,^{2(b),c)}  Pierluigi Bilotto,¹  Maximilian Lengauer,¹  Claudia Merola,¹  Hsiu-Wei Cheng,¹  Laura L. E. Mears,¹  and Markus Valtiner^{1,d)} 

AFFILIATIONS

¹Institute for Applied Physics, Vienna University of Technology, Wiedner Hauptstrasse 8-10, A-1040 Vienna, Austria

²Department of Material Science and Technology, Norwegian University of Science and Technology, NO-7491 Trondheim, Norway

^{a)}Electronic mail: kaischwenzfeier@tuwien.ac.at

^{b)}Electronic mail: SFA-explorer@the-passivists.org

^{c)}Also at: Max-Planck-Institut für Eisenforschung GmbH, Max-Planck-Str. 1, 40237 Düsseldorf, Germany.

^{d)}Author to whom correspondence should be addressed: markus.valtiner@tuwien.ac.at

ABSTRACT

Multiple beam interferometry (MBI) evolved as a powerful tool for the simultaneous evaluation of thin film thicknesses and refractive indices in Surface Forces Apparatus (SFA) measurements. However, analysis has relied on simplifications for providing fast or simplified analysis of recorded interference spectra. Here, we describe the implementation of new optics and a generalized fitting approach to 4×4 transfer matrix method simulations for the SFA. Layers are described by dispersive complex refractive indices, thicknesses, and Euler angles that can be fitted, providing modeling for birefringent or colored layers. Normalization of data by incident light intensities is essential for the implementation of a fitting approach. Therefore, a modular optical system is described that can be retrofitted to any existing SFA setup. Real-time normalization of spectra by white light is realized, alignment procedures are considerably simplified, and direct switching between transmission and reflection modes is possible. A numerical approach is introduced for constructing transfer matrices for birefringent materials. Full fitting of data to the simulation is implemented for arbitrary multilayered stacks used in SFA. This enables self-consistent fitting of mirror thicknesses, birefringence, and relative rotation of anisotropic layers (e.g., mica), evaluation of reflection and transmission mode spectra, and simultaneous fitting of thicknesses and refractive indices of media confined between two surfaces. In addition, a fast full spectral fitting method is implemented for providing a possible real-time analysis with up to 30 fps. We measure and analyze refractive indices of confined cyclohexane, the thickness of lipid bilayers, the thickness of metal layers, the relative rotation of birefringent materials, contact widths, as well as simultaneous fitting of both reflection and transmission mode spectra of typical interferometers. Our analyses suggest a number of best practices for conducting SFA and open MBI in an SFA for increasingly complex systems, including metamaterials, multilayered anisotropic layers, and chiral layers.

© 2019 Author(s). All article content, except where otherwise noted, is licensed under a Creative Commons Attribution (CC BY) license (<http://creativecommons.org/licenses/by/4.0/>). <https://doi.org/10.1063/1.5085210>

I. INTRODUCTION

Thin film studies using multiple-beam interferometry (MBI) evolved as a powerful tool for measuring absolute thicknesses and

complex refractive indices, \tilde{n} , of nanometer confined thin films between apposing surfaces.

Since the first analysis of MBI patterns by Tolansky,¹ the technique has further evolved to study surface and interfacial forces in

In situ nano- to microscopic imaging and growth mechanism of electrochemical dissolution (e.g., corrosion) of a confined metal surface

C. Merola^a, H.-W. Cheng^a, K. Schwenzfeier^a, K. Kristiansen^b, Y.-J. Chen^a, H. A. Dobbs^a, J. N. Israelachvili^{b,1}, and M. Valtiner^a

^aDepartment for Interface Chemistry and Surface Engineering, Max-Planck-Institut für Eisenforschung GmbH, D-40237 Düsseldorf, Germany, and ^bDepartment of Chemical Engineering, University of California, Santa Barbara, CA 93106

Contributed by J. N. Israelachvili, July 28, 2017 (sent for review May 19, 2017; reviewed by Joelle Frechette and Philippe Marcus)

Reactivity in confinement is central to a wide range of applications and systems, yet it is notoriously difficult to probe reactions in confined spaces in real time. Using a modified electrochemical surface forces apparatus (EC-SFA) on confined metallic surfaces, we observe in situ nano- to microscale dissolution and pit formation (qualitatively similar to previous observation on nonmetallic surfaces, e.g., silica) in well-defined geometries in environments relevant to corrosion processes. We follow “crevice corrosion” processes in real time in different pH-neutral NaCl solutions and applied surface potentials of nickel (vs. Ag|AgCl electrode in solution) for the mica-nickel confined interface of total area $\sim 0.03 \text{ mm}^2$. The initial corrosion proceeds as self-catalyzed pitting, visualized by the sudden appearance of circular pits with uniform diameters of 6–7 μm and depth $\sim 2\text{--}3 \text{ nm}$. At concentrations above 10 mM NaCl, pitting is initiated at the outer rim of the confined zone, while below 10 mM NaCl, pitting is initiated inside the confined zone. We compare statistical analysis of growth kinetics and shape evolution of individual nanoscale deep pits with estimates from macroscopic experiments to study initial pit growth and propagation. Our data and experimental techniques reveal a mechanism that suggests initial corrosion results in formation of an aggressive interfacial electrolyte that rapidly accelerates pitting, similar to crack initiation and propagation within the confined area. These results support a general mechanism for nanoscale material degradation and dissolution (e.g., crevice corrosion) of polycrystalline nonnoble metals, alloys, and inorganic materials within confined interfaces.

crevice corrosion | surface forces apparatus | pitting dynamics | surface electrochemistry

Reactivity in confinement is central to a wide range of applications and systems, such as geological and technological processes, for example, pressure solution (1, 2), chemical mechanical polishing (CMP) (3), electropolishing (4), and corrosion (5, 6), including biocorrosion, for example, implants and dental fillings (7, 8). In some cases, increased dissolution rates are desired, such as CMP; however, in other systems, particularly involving pitting and crevice corrosion, increased reactivity leads to material degradation and damage. In each of these systems, the confinement (close apposition) of two asymmetric surfaces in an aqueous environment is a common factor where increased reactivity is observed. However, unlike systems exposed to bulk solutions, the difficulties introduced by reactivity and transport (e.g., diffusion) in confinement lead to complications in developing an understanding of reaction processes under these conditions. Furthermore, few techniques are able to directly measure and study reactivity in confinement in situ at relevant length scales, leaving even more uncertainty surrounding the initiation and early growth of dissolution or corrosion processes in confinement. As a result, the understanding of early-stage reactivity in confinement remains challenging and more detailed nanoscale characterization methods are required to develop a deeper understanding.

From an electrochemical viewpoint, crevice corrosion—the focus of this article—and pitting corrosion are related phenomena

(9–11), although there are significant geometrical differences between them. Pitting corrosion is driven by an aggressive ionic environment and oxygen depletion in the stagnant electrolyte of growing pits on a surface exposed to bulk solution (12–14). Crevice corrosion is a related form of localized/confined corrosion that may occur within cracks and crevices where depletion and reduced transport of species such as oxygen may lead to the development of aggressive media and local corrosion potentials (15). Within crevice corrosion, the initiation and growth of pits are observed and, throughout this paper, we will commonly refer to pits within the crevice (which is a separate phenomenon from pitting corrosion).

Crevice corrosion is of particular concern for stainless steels and nickel alloys in contact with chloride-containing solutions, commonly found in marine environments (5, 6). Chloride anions can be found in a wide range of environments such as seawater, industrial raw water, and sludge. In particular, the potential gradient that develops in crevice corrosion drives cations out of the crevices and anions, such as chloride, into the crevices (14). The diffusion of ions into or out of crevices depends on their mobility. Chloride has a very high mobility and it is often present in high concentration in crevices. As such, chloride anions tend to accumulate inside the crevice while the more hydrated and larger cations (e.g., sodium), which typically are less mobile, remain mainly outside the crevice. In addition, the hydrolysis of the dissolving metal ions leads to a stark local variation of the pH (11, 12, 16). The dissolution products of the material (metallic cations) are also driven out of the crevice, which leads to a local change of the pH.

Significance

A surface forces apparatus was used with an electrochemical attachment to directly visualize electrochemical reactions, dissolution, and pitting on surfaces when confined in nanoscale gaps (or “crevices”) in real time. The results provide unique insights into how two closely apposed surfaces degrade under confinement, which is different from degradation of surfaces exposed to bulk solution. Degradation proceeds via local nucleation of “pits” at the periphery or center of the “contact area” that rapidly grow outward (in radius) and, more slowly, in depth, until the pits converge and the whole area has become one large pit. The results on a metal–inorganic interface are similar to previous observations on inorganic interfaces, and support a general mechanism of “pitting corrosion” at confined interfaces.

Author contributions: K.K., H.A.D., J.N.I., and M.V. designed research; C.M., H.-W.C., K.S., and Y.-J.C. performed research; C.M., H.-W.C., and M.V. analyzed data; and C.M., K.K., H.A.D., and M.V. wrote the paper.

Reviewers: J.F., Johns Hopkins University, and P.M., Chimie ParisTech-CNRS.

The authors declare no conflict of interest.

¹To whom correspondence should be addressed. Email: jacob@engineering.ucsb.edu.

This article contains supporting information online at www.pnas.org/lookup/suppl/doi:10.1073/pnas.1708205114/-DCSupplemental.



Novel *in situ* sensing surface forces apparatus for measuring gold versus gold, hydrophobic, and biophysical interactions

Cite as: J. Vac. Sci. Technol. A 39, 023201 (2021); doi: 10.1116/6.0000611

Submitted: 7 September 2020 · Accepted: 22 December 2020 ·

Published Online: 13 January 2021



Valentina Wieser,^{1,2} Pierluigi Bilotto,¹ Ulrich Ramach,^{1,3} Hui Yuan,⁴ Kai Schwenzfeier,¹ Hsiu-Wei Cheng,^{1,4} and Markus Valtiner^{1,4}

AFFILIATIONS

¹Institute of Applied Physics, Applied Interface Physics, Vienna University of Technology, Vienna 1040, Austria

²AIT Austrian Institute of Technology, Tulln 3425, Austria

³Centre for Electrochemical Surface Technology, Wiener Neustadt 2700, Austria

⁴State Key Laboratory of Chemical Engineering, School of Chemical Engineering and Technology, Tianjin University, Tianjin 310027, China

Note: This paper is part of the 2020 Special Topic Collection Celebrating 40 Years of the AVS Peter Mark Award.

Electronic mail: hsiu-wei@iap.tuwien.ac.at

Electronic mail: valtiner@iap.tuwien.ac.at

ABSTRACT

The surface forces apparatus (SFA) was developed in the late 1960s as a powerful tool for investigating molecular interactions across opposing surfaces including the first measurement of van der Waals forces and interactions in biologic and liquid media. However, the SFA has two major disadvantages. First, it traditionally uses white light interference between back-silvered muscovite mica surfaces to measure distances and to infer forces from distance shifts during interaction of two surfaces. Hence, distance shifts and force measurement are not decoupled. Second, productive SFA interferometers are so far limited to measuring across mica versus mica or mica versus metal. Direct gold-gold configurations were suggested in the late 1990s but not experimentally achieved as proof-of-principle until recently using a templating technique. In this work, we show how we solve these two disadvantages. First, we present a new SFA design that decouples force and distance measurements with similar resolution. The presented SFA design is inexpensive and can be home-built with mostly commercially available parts. Second, we present an alternative physical vapor deposition approach to construct a stable gold-gold interferometer and demonstrate its performance showing hydrophobic interactions, bubble formation, hemifusion of bilayers, and friction experiments. The presented system is easy to use. The obtained results show excellent reproducibility, indicating that the designed SFA and the three-mirror gold-gold interferometer functions as well as or even better than the traditional interferometer configurations used in SFA. This opens SFA to a wide range of options for various possible applications. Specifically, the gold-gold configuration allows a broad range of surface modifications for studying biophysical interactions as demonstrated in this work.

© 2021 Author(s). All article content, except where otherwise noted, is licensed under a Creative Commons Attribution (CC BY) license (<http://creativecommons.org/licenses/by/4.0/>). <https://doi.org/10.1116/6.0000611>

I. INTRODUCTION

All active systems that undergo change, motion, or flow of matter (*i.e.*, all biological systems and all mechanical systems) are subject to fundamental forces that drive and steer the way in which atoms, molecules, and ultimately macroscopic structures develop, evolve, adapt, and age. Consequently, the study of interactive forces

is a shared and fundamental interest in seemingly unrelated fields such as biophysics and adhesion, or surface science and stem cell research.

Techniques such as atomic force microscopy¹ or using optical tweezers² can measure forces at molecular-scale and nanoscale, while they do not actively track distances. In contrast, the surface

Excerpt from Patent

[Marken](#)
[Muster](#)
[Nationale Patente](#)
[Europäische Patente](#)
[Schutzertifikate](#)
[Download](#)



 österreichisches patentamt
 Version: 2.17.3.0 | Angemeldet als GUEST | [Login](#)

[Zurück zur Suchergebnisliste](#)

[Nationales Patent Details](#)
[Publikationen](#)

Titel	Verfahren und Vorrichtung zur Störgrößenkompensation bei der Positionierung eines Probenträgers
Aktenzeichen	A 50458/2021
Patentnummer	
Anmeldedatum	07.06.2021
Erteilt	
IPC	G01 Q
Status	In Anmeldung
Zugehörige Schutzertifikate	
InhaberIn	Technische Universität Wien, Karlsplatz 13, 1040, Wien (AT)
VertreterIn	SONN & PARTNER Patentanwälte, Riemergasse 14, 1010, Wien (AT)
ErfinderIn	
PrüferIn	KÖGL
Abteilung	3
Längste Dauer	
Prioritäten	
Nächstes Fälligkeitsdatum	
Nächster fälliger Betrag	
Art der Gebühr	
Stundungstext	
Angaben ohne Gewähr	

[Zurück zur Suchergebnisliste](#)

Excerpt from Patent

Die Erfindung betrifft ein Verfahren und eine Vorrichtung zur Störgrößenkompensation bei der Positionierung eines Probenträgers.

Die genaue Positionierung eines Probenträgers ist z.B. bei sondenmikroskopischen Messungen, in der Halbleitertechnologie bei der Einrichtung von Maske und Wafer und der Einkristalltomographie erforderlich.

Sondenmikroskopische Messungen verwenden spezielle Sonden (z.B. Rasterkraftmikroskopie: feine Nadel; Rastertunnelmikroskopie: feine, elektrisch leitende Drahtspitze; optische Pinzette: Partikel im Brennpunkt eines fokussierten Lasers), um deren Wechselwirkung mit einer Probe mit hoher örtlicher Auflösung von bis zu 0,01 nm zu vermessen und/oder bildgebend darzustellen.

Die Wechselwirkung der Sonde zur Probe hängt von der relativen Position der Sonde zur Probe ab. Alle Geräte dieser Klasse zeigen charakteristische Drifterscheinungen, welche die relative Position der Sonde zur Probe nicht-linear verändern. Drift wird durch thermische Expansion/Kontraktion der strukturellen Bauteile der Apparate, oder durch mechanische Relaxation gefügter Bauteilelemente verursacht. Die mit dem Drift einhergehende Ungenauigkeit der Sondenposition tritt in allen drei Raumrichtungen auf, stellt eine Störgröße bei der Positionierung des Sondenträgers bzw. der Sonde dar und liegt je nach Bauweise um 4-5 Größenordnung pro Minute über der theoretisch erreichbaren Auflösung von 0,01 nm. Damit ist ein hochexaktes zeitinvariantes Positionieren, sowie ein reproduzierbares Messen an einer in Echtzeit nanometergenau definierten Position über Zeiträume von Minuten bis Stunden nicht möglich.

Aus dem Stand der Technik sind zur Kompensation dieser Drifteffekte verschiedene Methoden bekannt: Bauliche Maßnahmen umfassen beispielsweise die Verwendung von Konstruktionsmaterialien mit geringer thermischer Ausdehnung, Minimierung von Verbindungen auf Basis von Haftreibung oder symmetrischen Aufbau. Andere Maßnahmen umfassen weiterhin Isolation von Schall, Stabilisierung gegenüber Temperaturänderungen oder Vermeidung von Schwingungen

durch bauliche Maßnahmen des Raums, der das Gerät beherbergt. Zu weniger aufwändigen Methoden gehören Softwarelösungen wie Adaptionen im Messprotokoll, die Redundanzen und bekannte Marker enthalten, sowie softwaregestützte Korrekturen nach der Messung. Methoden der Echtzeitkorrektur werden technisch über zusätzliche Probenmarker realisiert, die mittels zusätzlicher Sensorsysteme geortet werden können.

Nachteilig an vorgenannten Methoden ist, dass sie sehr kostspielig (bauliche und nicht-bauliche Maßnahmen) sind, die Messzeit so erhöhen können, dass zeitkritische Messprobleme ausgeschlossen werden (zusätzliche Redundanzen), oder bewirken, dass die Messung nicht mehr der Messaufgabe entspricht, weil die gewollte relative Position nicht gehalten werden kann (nachträgliche Korrektur). Ein weiterer Nachteil der etablierten Korrekturmethode in Echtzeit mittels Probenmarkern besteht darin, dass die Lösung speziell in die Messmethode eingefügt und die Probe hierauf angepasst und adaptiert werden muss. Dieser Schritt ist nicht allgemein gültig, d.h. nicht alle Probensysteme erlauben das Aufbringen von Markern und potentieller Drift des Detektionssystems an sich wird hierbei ignoriert.

Diese Probleme treten allgemein bei der genauen Positionierung von Probenträgern auf.

Die US 2013/0098274 A1 zeigt eine Probenvorrichtung, bei der mit Laserinterferometern die Entfernung zu einem Probentisch in x-Richtung und in y-Richtung ermittelt wird. Nachteiligerweise kann damit jedoch eine thermische Expansion des Probentisches nicht kompensiert werden, da diese nicht ermittelt werden kann.

Die Aufgabe der Erfindung liegt darin, zumindest einen der Nachteile des Stands der Technik zu lindern oder zu beseitigen. Insbesondere liegt der Erfindung die Aufgabe zugrunde, ein Verfahren und eine Vorrichtung bereitzustellen, bei dem/der methodenunabhängig Störgrößen (insbesondere thermischer Drift und thermische Expansion) in Bezug auf die Positionierung eines Probenträgers relativ zu einem Sensorträger (insbesondere in Echtzeit) kompensiert werden, vorzugsweise ohne dabei eine besondere Beschaffenheit der Probe zu benötigen.

Copyright Clearances

Firefox

https://marketplace.copyright.com/rs-ui-web/mp/license/cc62e297-45b...



This is a License Agreement between Kai Schwenzfeier ("User") and Copyright Clearance Center, Inc. ("CCC") on behalf of the Rightsholder identified in the order details below. The license consists of the order details, the CCC Terms and Conditions below, and any Rightsholder Terms and Conditions which are included below.
All payments must be made in full to CCC in accordance with the CCC Terms and Conditions below.

Order Date	01-Mar-2022	Type of Use	Republish in a thesis/dissertation
Order License ID	1194705-1	Publisher	American Institute of Physics
ISSN	1089-7623	Portion	Chapter/article

LICENSED CONTENT

Publication Title	Review of scientific instruments online	Rightsholder	American Institute of Physics
Article Title	Optimizing multiple beam interferometry in the surface forces apparatus: Novel optics, reflection mode modeling, metal layer thicknesses, birefringence, and rotation of anisotropic layers.	Publication Type	e-Journal
		Start Page	043908
		Issue	4
		Volume	90
		URL	http://aip.scitation.org/journal/rsi
Author/Editor	American Institute of Physics		
Date	01/01/1930		
Language	English		
Country	United States of America		

REQUEST DETAILS

Portion Type	Chapter/article	Distribution	Other territories and/or countries
Page range(s)	1-15	Enter territories/countries	Austria
Total number of pages	15	Translation	Original language of publication
Format (select all that apply)	Print, Electronic	Copies for the disabled?	No
Who will republish the content?	Academic institution	Minor editing privileges?	Yes
Duration of Use	Life of current edition	Incidental promotional use?	No
Lifetime Unit Quantity	Up to 499	Currency	EUR
Rights Requested	Main product and any product related to main product		

NEW WORK DETAILS

Title	Development of an interferometry-based drift-compensated scanning probe microscopy technique to measure surface forces	Institution name	Institute of Applied Physics, TU Wien, Austria
		Expected presentation date	2022-04-27
Instructor name	Prof. Dr. Markus Valtiner		

ADDITIONAL DETAILS

1 of 4

02.03.22, 10:24

Bibliography

- [1] C. Jarzynski. Nonequilibrium Equality for Free Energy Differences. *Phys. Rev. Lett.*, 78(14):2690–2693, Apr 1997. ISSN 1079-7114. doi: 10.1103/PhysRevLett.78.2690.
- [2] C. Jarzynski. Equilibrium free-energy differences from nonequilibrium measurements: A master-equation approach. *Phys. Rev. E*, 56(5):5018–5035, Nov 1997. ISSN 2470-0053. doi: 10.1103/PhysRevE.56.5018.
- [3] F. Marinello, P. Bariani, L. De Chiffre, and E. Savio. Fast technique for AFM vertical drift compensation. *Meas. Sci. Technol.*, 18(3):689–696, Jan 2007. ISSN 0957-0233. doi: 10.1088/0957-0233/18/3/019.
- [4] Travis R. Meyer, Dominik Ziegler, Christoph Brune, Alex Chen, Rodrigo Farnham, Nen Huynh, Jen-Mei Chang, Andrea L. Bertozzi, and Paul D. Ashby. Height drift correction in non-raster atomic force microscopy. *Ultramicroscopy*, 137:48–54, Feb 2014. ISSN 0304-3991. doi: 10.1016/j.ultramic.2013.10.014.
- [5] Ryosuke Kizu, Ichiko Misumi, Akiko Hirai, and Satoshi Gonda. A reference-scan-based method for correcting the nonlinear drift of atomic force microscopy at sub-nanometer precision. *Meas. Sci. Technol.*, 31(5):054009, Mar 2020. ISSN 0957-0233. doi: 10.1088/1361-6501/ab6b50.
- [6] Philipp Rahe, Jens Schütte, Werner Schniederberend, Michael Reichling, Masayuki Abe, Yoshiaki Sugimoto, and Angelika Kühnle. Flexible drift-compensation system for precise 3D force mapping in severe drift environments. *Rev. Sci. Instrum.*, 82(6):063704, Jun 2011. ISSN 0034-6748. doi: 10.1063/1.3600453.
- [7] Johannes Degenhardt, Rainer Tutsch, and Gaoliang Dai. Flexible correction of 3D non-linear drift in SPM measurements by data fusion. *Meas. Sci. Technol.*, 32(3):035005, Dec 2020. ISSN 0957-0233. doi: 10.1088/1361-6501/abc9f8.
- [8] Yuliang Wang, Huimin Wang, and Shusheng Bi. Real time drift measurement for colloidal probe atomic force microscope: a visual sensing approach. *AIP Adv.*, 4(5):057130, May 2014. ISSN 2158-3226. doi: 10.1063/1.4880242.
- [9] Charles A. Clifford and Martin P. Seah. Simplified drift characterization in scanning probe microscopes using a simple two-point method. *Meas. Sci. Technol.*, 20(9):095103, Jul 2009. ISSN 0957-0233. doi: 10.1088/0957-0233/20/9/095103.

Bibliography

- [10] Kai A. Schwenzfeier, Andreas Erbe, Pierluigi Bilotto, Maximilian Lengauer, Claudia Merola, Hsiu-Wei Cheng, Laura L. E. Mears, and Markus Valtiner. Optimizing multiple beam interferometry in the surface forces apparatus: Novel optics, reflection mode modeling, metal layer thicknesses, birefringence, and rotation of anisotropic layers. *Rev. Sci. Instrum.*, 90(4):043908, Apr 2019. ISSN 0034-6748. doi: 10.1063/1.5085210.
- [11] J. Israelachvili. Interferometric Method for determining Refractive Index and Thickness of Thin Films. *Nature Physical Science*, 229:85–86, Jan 1971. ISSN 2058-1106. doi: 10.1038/physci229085b0.
- [12] J. N. Israelachvili, Y. Min, M. Akbulut, A. Alig, G. Carver, W. Greene, K. Kristiansen, E. Meyer, N. Pesika, K. Rosenberg, and H. Zeng. Recent advances in the surface forces apparatus (SFA) technique. *Reports on Progress in Physics*, 73(3), March 2010.
- [13] R. M. A. Azzam and N. M. Bashara. *Ellipsometry and Polarized Light (North-Holland Personal Library)*. xn-3ug : xn-2ug Elsevier Science Ltd, May 1987. URL <https://www.amazon.de/Ellipsometry-Polarized-North-Holland-Personal-Library/dp/0444870164>.
- [14] O. S. Heavens. *Optical Properties of Thin Solid Films*. Courier Corporation, Jan 1991. ISBN 978-0-48666924-3. URL https://books.google.at/books/about/Optical_Properties_of_Thin_Solid_Films.html?id=gRsZytsSnkQC&redir_esc=y.
- [15] O. S. Heavens. *Thin Film Physics*, chapter 6. Methuen, London, England, UK, 1970. ISBN 978-0-41607650-9. URL https://books.google.at/books/about/Thin_film_physics.html?id=heINAQAIAAJ&redir_esc=y.
- [16] A. Vašíček. *Optics of Thin Films*. North-Holland, 1960.
- [17] F. Abelès. Methods for determining optical parameters in thin films. In E. Wolf, editor, *Progress in Optics*, volume II. North-Holland, 1963.
- [18] O. S. Heavens. Measurement of optical constants of thin films. In G. Hass and R. E. Thun, editors, *Physics of Thin Films*, volume 2. Academic Press, 1964.
- [19] H. E. Bennett and J. M. Bennett. Precision measurements in thin film optics. In G. Hass and R. E. Thun, editors, *Physics of Thin Films*, volume 4. Academic Press, 1967.
- [20] F. Abelès. Optical properties of metallic films. In G. Hass and R. E. Thun, editors, *Physics of Thin Films*, volume 6. Academic Press, 1971.

- [21] M. Schubert. Polarization-dependent optical parameters of arbitrarily anisotropic homogeneous layered systems. *Physical Review B*, 53(8):4265–4274, February 1996. doi: 10.1103/PhysRevB.53.4265. URL <https://link.aps.org/doi/10.1103/PhysRevB.53.4265>.
- [22] P. Yeh. Optics of anisotropic layered media: A new 4×4 matrix algebra. *Surface Science*, 96:41–53, June 1980. doi: 10.1016/0039-6028(80)90293-9.
- [23] S. Tolansky. Interferometric evaluation of thicknesses of thin films. *Journal de Physique et le Radium*, 11(7):373–374, July 1950. ISSN 0368-3842. doi: 10.1051/jphysrad:01950001107037300. URL <http://dx.doi.org/10.1051/jphysrad:01950001107037300>.
- [24] D. Tabor and R. H. Winterton. Surface forces - direct measurement of normal and retarded van der waals forces. *Nature*, 219(5159):1120+, 1968.
- [25] D. Tabor and R. H. Winterton. Direct measurement of normal and retarded van der waals forces. *Proceedings of the Royal Society of London A*, 312(1511):435+, 1969.
- [26] J. N. Israelachvili. Thin film studies using multiple-beam interferometry. *Journal of Colloid and Interface Science*, 44(2):259–272, August 1973. ISSN 0021-9797. doi: 10.1016/0021-9797(73)90218-X. URL <http://www.sciencedirect.com/science/article/pii/002197977390218X>.
- [27] J. N. Israelachvili and D. Tabor. Measurement of van der waals dispersion forces in range 1.4 to 130 nm. *Nature - Physical Science*, 236(68):106+, 1972.
- [28] J. N. Israelachvili and R. M. Pashley. The hydrophobic interaction is long-range, decaying exponentially with distance. *Nature*, 300(5890):341–342, 1982.
- [29] J. N. Israelachvili and R. M. Pashley. Molecular layering of water at surfaces and origin of repulsive hydration forces. *Nature*, 306(5940):249–250, 1983.
- [30] J. N. Israelachvili, R. K. Tandon, and L. R. White. Measurement of forces between 2 mica surfaces in aqueous poly(ethylene oxide) solutions. *Nature*, 277(5692):120–121, 1979.
- [31] L. R. Fisher and J. N. Israelachvili. Direct experimental-verification fo the kelvin equation for capillary condensation. *Nature*, 277(5697):548–549, 1979.
- [32] J. N. Israelachvili and G. E. Adams. Measurement of forces between 2 mica surfaces in aqueous electrolyte solutions in range 0-100 nm. *Journal of the Chemical Society - Faraday Transactions I*, 74(4):975+, 1978.
- [33] Stephen H. Donaldson, Jr., M. Valtiner, Matthew A. Gebbie, J. Haradad, and J. N. Israelachvili. Interactions and visualization of bio-mimetic membrane

- detachment at smooth and nano-rough gold electrode surfaces. *Soft matter*, 9 (21):5231–5238, 2013.
- [34] C. Pick, C. Argento, G. Drazer, and J. Frechette. Micropatterned charge heterogeneities via vapor deposition of aminosilanes. *Langmuir*, 31(39):10725–10733, October 2015.
- [35] M. Valtiner, Stephen H. Donaldson, Jr., Matthew A. Gebbie, and J. N. Israelachvili. Hydrophobic forces, electrostatic steering, and acid-base bridging between atomically smooth self-assembled monolayers and end-functionalized pegolated lipid bilayers. *Journal of the American Chemical Society*, 134(3):1746–1753, January 2012.
- [36] M. Valtiner, X. Banquy, K. Kristiansen, George W. Greene, and J. N. Israelachvili. The Electrochemical Surface Forces Apparatus: The Effect of Surface Roughness, Electrostatic Surface Potentials, and Anodic Oxide Growth on Interaction Forces, and Friction between Dissimilar Surfaces in Aqueous Solutions. *Langmuir*, 28(36):13080–13093, September 2012.
- [37] B. R. Shrestha, T. Baimpos, S. Raman, and M. Valtiner. Angstrom-Resolved Real-Time Dissection of Electrochemically Active Noble Metal Interfaces. *ACS Nano*, 8(6):5979–5987, June 2014. ISSN 1936-0851. doi: 10.1021/nn501127n. URL <https://doi.org/10.1021/nn501127n>.
- [38] J. N. Connor and R. G. Horn. Extending the surface force apparatus capabilities by using white light interferometry in reflection. *Review of Scientific Instruments*, 74(11):4601–4606, November 2003.
- [39] C. Merola, H.-W. Cheng, K. Schwenzfeier, K. Kristiansen, Y.-J. Chen, H. A. Dobbs, J. N. Israelachvili, and M. Valtiner. In situ nano- to microscopic imaging and growth mechanism of electrochemical dissolution (e.g., corrosion) of a confined metal surface. *Proceedings of the National Academy of Sciences of the United States of America*, 114(36):9541–9546, September 2017.
- [40] B. R. Shrestha, Q. Hu, T. Baimpos, K. Kristiansen, J. N. Israelachvili, and M. Valtiner. Real-Time Monitoring of Aluminum Crevice Corrosion and Its Inhibition by Vanadates with Multiple Beam Interferometry in a Surface Forces Apparatus. *Journal of the Electrochemical Society*, 162(7):C327–C332, 2015.
- [41] J. M. Levins and T. K. Vanderlick. Extended spectral-analysis of multiple-beam interferometry. *Langmuir*, 10(7):2389–2394, July 1994.
- [42] M. T. Clarkson. Multiple-beam interferometry with thin metal films and unsymmetrical systems. *Journal of Physics D - Applied Physics*, 22(4):475–482, April 1989.

- [43] M. Born and E. Wolf. *Principles of Optics*, chapter 1.6.2. Pergamon Press, fourth edition, 1970.
- [44] M. Heuberger. The extended surface forces apparatus. Part I. Fast spectral correlation interferometry. *Review of Scientific Instruments*, 72(3):1700–1707, March 2001.
- [45] M. Zach, J. Vanicek, and M. Heuberger. The extended surface forces apparatus. Part III. High-speed interferometric distance measurement. *Review of Scientific Instruments*, 74(1, 1):260–266, January 2003.
- [46] B. Zappone, W. Zheng, and S. Perkin. Multiple-beam optical interferometry of anisotropic soft materials nanoconfined with the surface force apparatus. *Review of scientific Instruments*, 89(8), August 2018.
- [47] D. F. Kienle and T. L. Kuhl. Analyzing refractive index profiles of confined fluids by interferometry. *Analytical Chemistry*, 86(23):11860–11867, December 2014.
- [48] D. F. Kienle and T. L. Kuhl. Analyzing refractive index profiles of confined fluids by interferometry part II: Multilayer and asymmetric systems. *Analytica Chimica Acta*, 936:236–244, September 2016.
- [49] Martina Reithmeier and Andreas Erbe. Dielectric interlayers for increasing the transparency of metal films for mid-infrared attenuated total reflection spectroscopy. *Phys. Chem. Chem. Phys.*, 12(44):14798–14803, Nov 2010. ISSN 1463-9076. doi: 10.1039/C0CP01125H.
- [50] D. W. Berreman. Optics in Stratified and Anisotropic Media: 4×4-Matrix Formulation. *Journal of the Optical Society of America*, 62(4):502–510, April 1972. doi: 10.1364/JOSA.62.000502. URL <https://www.osapublishing.org/josa/abstract.cfm?uri=josa-62-4-502>.
- [51] H. Wöhler, G. Haas, M. Fritsch, and D. A. Mlynski. Faster 4 × 4 matrix method for uniaxial inhomogeneous media. *Journal of the Optical Society of America A*, 5(9):1554–1557, September 1988. ISSN 1520-8532. doi: 10.1364/JOSAA.5.001554. URL <https://www.osapublishing.org/josaa/abstract.cfm?uri=josaa-5-9-1554>.
- [52] T. E. Oliphant. *Guide to NumPy*. Provo, UT, March 2006. URL <http://www.tramy.us/>.
- [53] William M. Moore and Peter J. Codella. Oxidation of silver films by atomic oxygen. *The Journal of Physical Chemistry*, 92(15):4421–4426, 1988. doi: 10.1021/j100326a035. URL <https://doi.org/10.1021/j100326a035>.

Bibliography

- [54] Lai-Kwan Chau and Marc D. Porter. Composition and structure of spontaneously adsorbed monolayers of n-perfluorocarboxylic acids on silver. *Chemical Physics Letters*, 167(3):198 – 204, 1990. doi: [https://doi.org/10.1016/0009-2614\(90\)85005-W](https://doi.org/10.1016/0009-2614(90)85005-W). URL <http://www.sciencedirect.com/science/article/pii/000926149085005W>.
- [55] Norland Products. Product data sheet for noa81, 2019. URL <https://www.norlandprod.com/adhesives/NOA%2081.html>.
- [56] C. D. van Engers, M. Balabajew, A. Southam, and S. Perkin. A 3-mirror surface force balance for the investigation of fluids confined to nanoscale films between two ultra-smooth polarizable electrodes. *Review of Scientific Instruments*, 89(12):123901, 2018. doi: 10.1063/1.5045485. URL <https://doi.org/10.1063/1.5045485>.
- [57] D. W. Lee, K. Kristiansen, Stephen H. Donaldson, Jr., N. Cadirov, X. Banquy, and J. N. Israelachvili. Real-time intermembrane force measurements and imaging of lipid domain morphology during hemifusion. *Nature Communications*, 6, May 2015.
- [58] S. de Beer, D. 't Mannetje, S. Zantema, and F. Mugele. Instability of confined water films between elastic surfaces. *Langmuir*, 26(5):3280–3285, March 2010.
- [59] F. Mugele and M. Salmeron. Dynamics of layering transitions in confined liquids. *Physical Review Letters*, 84(25):5796–5799, June 2000.
- [60] F. Mugele, S. Baldelli, G. A. Somorjai, and M. Salmeron. Structure of confined films of chain alcohols. *Journal of Physical Chemistry B*, 104(14):3140–3144, April 2000.
- [61] A. I. Bailey and S. M. Kay. Measurement of refractive index and dispersion of mica, employing multiple beam interference techniques. *British Journal of Applied Physics*, 16:39–44, 1965.
- [62] K.B. Rodenhausen, B.A. Duensing, T. Kasputis, A.K. Pannier, T. Hofmann, M. Schubert, T.E. Tiwald, M. Solinsky, and M. Wagner. In-situ monitoring of alkanethiol self-assembled monolayer chemisorption with combined spectroscopic ellipsometry and quartz crystal microbalance techniques. *Thin Solid Films*, 519(9):2817 – 2820, 2011. ISSN 0040-6090. doi: <https://doi.org/10.1016/j.tsf.2010.11.081>. URL <http://www.sciencedirect.com/science/article/pii/S0040609010016275>. 5th International Conference on Spectroscopic Ellipsometry (ICSE-V).
- [63] D. Peev, T. Hofmann, N. Kananizadeh, S. Beeram, E. Rodriguez, S. Wimer, K. B. Rodenhausen, C. M. Herzinger, T. Kasputis, E. Pfaumiller, A. Nguyen, R. Korlacki, A. Pannier, Y. Li, E. Schubert, D. Hage, and M. Schubert.

- Anisotropic contrast optical microscope. *Review of Scientific Instruments*, 87(11):113701, 2016. doi: 10.1063/1.4965878. URL <https://doi.org/10.1063/1.4965878>.
- [64] K. B. Rodenhausen, T. Kasputis, A. K. Pannier, J. Y. Gerasimov, R. Y. Lai, M. Solinsky, T. E. Tiwald, H. Wang, A. Sarkar, T. Hofmann, N. Ianno, and M. Schubert. Combined optical and acoustical method for determination of thickness and porosity of transparent organic layers below the ultra-thin film limit. *Review of Scientific Instruments*, 82(10):103111, 2011. doi: 10.1063/1.3653880. URL <https://doi.org/10.1063/1.3653880>.
- [65] K.B. Rodenhausen and M. Schubert. Virtual separation approach to study porous ultra-thin films by combined spectroscopic ellipsometry and quartz crystal microbalance methods. *Thin Solid Films*, 519(9):2772 – 2776, 2011. ISSN 0040-6090. doi: <https://doi.org/10.1016/j.tsf.2010.11.079>. URL <http://www.sciencedirect.com/science/article/pii/S0040609010016251>. 5th International Conference on Spectroscopic Ellipsometry (ICSE-V).
- [66] D. F. Kienle, J. V. de Souza, E. B. Watkins, and T. L. Kuhl. Thickness and refractive index of dppc and dppe monolayers by multiple-beam interferometry. *Analytical and Bioanalytical Chemistry*, 406(19):4725–4733, July 2014.
- [67] Zdzislaw Salamon and Gordon Tollin. Optical anisotropy in lipid bilayer membranes: Coupled plasmon-waveguide resonance measurements of molecular orientation, polarizability, and shape. *Biophysical Journal*, 80(3):1557 – 1567, 2001. ISSN 0006-3495. doi: [https://doi.org/10.1016/S0006-3495\(01\)76128-0](https://doi.org/10.1016/S0006-3495(01)76128-0). URL <http://www.sciencedirect.com/science/article/pii/S0006349501761280>.
- [68] M. Heuberger, M. Zach, and N. D. Spencer. Density fluctuations under confinement: When is a fluid not a fluid? *Science*, 292(5518):905–908, May 2001.
- [69] Henning Weiss, Hsiu-Wei Cheng, Julian Mars, Hailong Li, Claudia Merola, Frank Uwe Renner, Veijo Honkimäki, Markus Valtiner, and Markus Mezger. Structure and Dynamics of Confined Liquids: Challenges and Perspectives for the X-ray Surface Forces Apparatus. *Langmuir*, 35(51):16679–16692, Dec 2019. ISSN 0743-7463. doi: 10.1021/acs.langmuir.9b01215.
- [70] Claudia Merola, Hsiu-Wei Cheng, Dominik Dworschak, Ching-Shun Ku, Ching-Yu Chiang, Frank Uwe Renner, and Markus Valtiner. Nanometer Resolved Real Time Visualization of Acidification and Material Breakdown in Confinement. *Adv. Mater. Interfaces*, 6(10):1802069, May 2019. ISSN 2196-7350. doi: 10.1002/admi.201802069.
- [71] Pierluigi Bilotto, Maximilian Lengauer, Jakob Andersson, Ulrich Ramach, Laura L. E. Mears, and Markus Valtiner. Interaction Profiles and Stability

- of Rigid and Polymer-Tethered Lipid Bilayer Models at Highly Charged and Highly Adhesive Contacts. *Langmuir*, 35(48):15552–15563, Dec 2019. ISSN 0743-7463. doi: 10.1021/acs.langmuir.9b01942.
- [72] Valentina Wieser, Pierluigi Bilotto, Ulrich Ramach, Hui Yuan, Kai Schwenzfeier, Hsiu-Wei Cheng, and Markus Valtiner. Novel in situ sensing surface forces apparatus for measuring gold versus gold, hydrophobic, and biophysical interactions. *J. Vac. Sci. Technol., A*, 39(2):023201, Jan 2021. ISSN 0734-2101. doi: 10.1116/6.0000611.
- [73] Hans-Jürgen Butt, Brunero Cappella, and Michael Kappl. Force measurements with the atomic force microscope: Technique, interpretation and applications. *Surf. Sci. Rep.*, 59(1):1–152, Oct 2005. ISSN 0167-5729. doi: 10.1016/j.surfrep.2005.08.003.
- [74] Gavin M. King, Ashley R. Carter, Allison B. Churnside, Louisa S. Eberle, and Thomas T. Perkins. Ultrastable Atomic Force Microscopy: Atomic-Scale Stability and Registration in Ambient Conditions. *Nano Lett.*, 9(4):1451–1456, Apr 2009. ISSN 1530-6984. doi: 10.1021/nl803298q.
- [75] Clayton T. McKee, Wade K. J. Mosse, and William A. Ducker. Measurement of the absolute separation for atomic force microscopy measurements in the presence of adsorbed polymer. *Rev. Sci. Instrum.*, 77(5):053706, May 2006. ISSN 0034-6748. doi: 10.1063/1.2202929.
- [76] Seetharamaiah Attili and Ralf P. Richter. Combining Colloidal Probe Atomic Force and Reflection Interference Contrast Microscopy to Study the Compressive Mechanics of Hyaluronan Brushes. *Langmuir*, 28(6):3206–3216, Feb 2012. ISSN 0743-7463. doi: 10.1021/la204602n.
- [77] J. N. Israelachvili and D. Gourdon. Putting Liquids Under Molecular-Scale Confinement. *Science*, 292(5518):867–868, May 2001. ISSN 0036-8075, 1095-9203. doi: 10.1126/science.1061206. URL <http://science.sciencemag.org/content/292/5518/867>.
- [78] B. R. Shrestha, T. Baimpos, S. Raman, and M. Valtiner. Angstrom-Resolved Real-Time Dissection of Electrochemically Active Noble Metal Interfaces. *ACS Nano*, 8(6):5979–5987, June 2014.
- [79] R. Gupta and J. Frechette. Interferometry of surfaces with well-defined topography in the surface force apparatus. *Journal of Colloid and Interface*, 412: 82–88, December 2013.
- [80] Sho Fujii, Motohiro Kasuya, and Kazue Kurihara. Characterization of Platinum Electrode Surfaces by Electrochemical Surface Forces Measurement. *J. Phys. Chem. C*, 121(47):26406–26413, Nov 2017. ISSN 1932-7447. doi: 10.1021/acs.jpcc.7b09301.

- [81] Jacob N. Israelachvili. *Intermolecular and Surface Forces*. Elsevier, Academic Press, 2011. ISBN 978-0-12-375182-9. doi: 10.1016/C2009-0-21560-1.
- [82] P. E. Hillner, M. Radmacher, and P. K. Hansma. Combined atomic force and scanning reflection interference contrast microscopy. *Scanning*, 17(3):144–147, 1995.
- [83] J. K. Stuart and V. Hlady. Reflection interference contrast microscopy combined with scanning force microscopy verifies the nature of protein-ligand interaction force measurements. *Biophys. J.*, 76(1 Pt 1):500, Jan 1999. doi: 10.1016/S0006-3495(99)77218-8.
- [84] Hui Yuan, Hsiu-Wei Cheng, Laura L. E. Mears, Renliang Huang, Rongxin Su, Wei Qi, Zhimin He, and Markus Valtiner. Lipid Anchoring Improves Lubrication and Wear Resistance of the Collagen I Matrix. *Langmuir*, 37(47):13810–13815, Nov 2021. ISSN 0743-7463. doi: 10.1021/acs.langmuir.1c01581.
- [85] Julia Appenroth, Laila Moreno Ostertag, Alexander M. Imre, Markus Valtiner, and Laura L. E. Mears. Mechanistic understanding of catechols and integration into an electrochemically cross-linked mussel foot inspired adhesive hydrogel. *Biointerphases*, 16(6):061002, Dec 2021. ISSN 1934-8630. doi: 10.1116/6.0001609.
- [86] Hsiu-Wei Cheng and Markus Valtiner. Forces, structures, and ion mobility in nanometer-to-subnanometer extreme spatial confinements: Electrochemistry and ionic liquids. *Curr. Opin. Colloid Interface Sci.*, 47:126–136, Jun 2020. ISSN 1359-0294. doi: 10.1016/j.cocis.2020.02.003.
- [87] Valentina Wieser, Laura L. E. Mears, Robert D. Barker, Hsiu-Wei Cheng, and Markus Valtiner. Hydration Forces Dominate Surface Charge Dependent Lipid Bilayer Interactions under Physiological Conditions. *J. Phys. Chem. Lett.*, 12(38):9248–9252, Sep 2021. doi: 10.1021/acs.jpcclett.1c02572.
- [88] M. Newville, T. Stensitzki, D. B. Allen, and A. Ingargiola. LMFIT: Non-Linear Least-Square Minimization and Curve-Fitting for Python, September 2014. URL <https://doi.org/10.5281/zenodo.11813>.
- [89] The Winpython development team. WinPython, 2017. URL <https://github.com/winpython/winpython>.
- [90] A. Lizardo, B. Araujo, H. Parente Lima, L. Moura, L. M. Wolf, M. Lira, P. Alcantara, R. A. O. Filho, and W. Moreira. PySide, 2016. URL <https://wiki.qt.io/PySide>.
- [91] E. Jones, T. Oliphant, P. Peterson, et al. SciPy: Open source scientific tools for Python, 2001+. URL <http://www.scipy.org/>.

Bibliography

- [92] wiredfool, A. Clark, Hugo, A. Murray, A. Karpinsky, C. Gohlke, B. Crowell, D. Schmidt, A. Houghton, S. Johnson, S. Mani, J. Ware, D. Caro, S. Kossouho, E. W. Brown, A. Lee, M. Korobov, M. Górný, E. Santana Santana, N. Pieuchot, O. Tonnhofer, M. Brown, B. Pierre, J. Cuenca Abela, L. J. Solberg, F. Reyes, A. Buzanov, Y. Yu, eliempje, and F. Tolf. Pillow: 4.0.0, January 2017. URL <https://doi.org/10.5281/zenodo.44297>.
- [93] L. Campagnola. PyQtGraph, 20117. URL <http://www.pyqtgraph.org>.
- [94] A. D. Rakić, A. B. Djurišić, J. M. Elazar, and M. L. Majewski. Optical properties of metallic films for vertical-cavity optoelectronic devices. *Journal of Applied Optics*, pages 5271–5283, 1998.
- [95] I. Z. Kozma, P. Krok, and E. Riedle. Direct measurement of the group-velocity mismatch and derivation of the refractive-index dispersion for a variety of solvents in the ultraviolet. *Journal of the Optical Society of America B*, pages 1479–1485, 2005. measured at 22 °C.
- [96] G. M. Hale and M. R. Querry. Optical constants of water in the 200-nm to 200- μ m wavelength region. *Journal of Applied Optics*, pages 555–563, 1973. measured at 25 °C.
- [97] P. E. Ciddor. Refractive index of air: new equations for the visible and near infrared. *Journal of Applied Optics*, pages 1566–1573, 1996.
- [98] M. Polyanskiy. refractiveindex.info, 2018. URL <http://refractiveindex.info>.
- [99] Jacob N. Israelachvili, Norma A. Alcantar, Nobuo Maeda, Thomas E. Mates, and Marina Ruths. Preparing Contamination-free Mica Substrates for Surface Characterization, Force Measurements, and Imaging. *Langmuir*, 20(9):3616–3622, Apr 2004. ISSN 0743-7463. doi: 10.1021/la0352974.